

“Understanding and controlling mammalian photoreceptor functions in health and disease”

Inauguraldissertation

zur

Erlangung der Würde eines Doktors der Philosophie

vorgelegt der

Philosophisch-Naturwissenschaftlichen Fakultät

der Universität Basel

von

Volker Busskamp

aus Bocholt, Deutschland

Basel, 2010

Originaldokument gespeichert auf dem Dokumentenserver der Universität Basel

edoc.unibas.ch



Dieses Werk ist unter dem Vertrag „Creative Commons Namensnennung-Keine kommerzielle Nutzung-Keine Bearbeitung 2.5 Schweiz“ lizenziert. Die vollständige Lizenz kann unter creativecommons.org/licences/by-nc-nd/2.5/ch eingesehen werden.



Namensnennung-Keine kommerzielle Nutzung-Keine Bearbeitung 2.5 Schweiz

Sie dürfen:



das Werk vervielfältigen, verbreiten und öffentlich zugänglich machen

Zu den folgenden Bedingungen:



Namensnennung. Sie müssen den Namen des Autors/Rechteinhabers in der von ihm festgelegten Weise nennen (wodurch aber nicht der Eindruck entstehen darf, Sie oder die Nutzung des Werkes durch Sie würden entlohnt).



Keine kommerzielle Nutzung. Dieses Werk darf nicht für kommerzielle Zwecke verwendet werden.



Keine Bearbeitung. Dieses Werk darf nicht bearbeitet oder in anderer Weise verändert werden.

- Im Falle einer Verbreitung müssen Sie anderen die Lizenzbedingungen, unter welche dieses Werk fällt, mitteilen. Am Einfachsten ist es, einen Link auf diese Seite einzubinden.
- Jede der vorgenannten Bedingungen kann aufgehoben werden, sofern Sie die Einwilligung des Rechteinhabers dazu erhalten.
- Diese Lizenz lässt die Urheberpersönlichkeitsrechte unberührt.

Die gesetzlichen Schranken des Urheberrechts bleiben hiervon unberührt.

Die Commons Deed ist eine Zusammenfassung des Lizenzvertrags in allgemeinverständlicher Sprache: <http://creativecommons.org/licenses/by-nc-nd/2.5/ch/legalcode.de>

Haftungsausschluss:

Die Commons Deed ist kein Lizenzvertrag. Sie ist lediglich ein Referenztext, der den zugrundeliegenden Lizenzvertrag übersichtlich und in allgemeinverständlicher Sprache wiedergibt. Die Deed selbst entfaltet keine juristische Wirkung und erscheint im eigentlichen Lizenzvertrag nicht. Creative Commons ist keine Rechtsanwalts-gesellschaft und leistet keine Rechtsberatung. Die Weitergabe und Verlinkung des Commons Deeds führt zu keinem Mandatsverhältnis.

Genehmigt von der Philosophisch-Naturwissenschaftlichen Fakultät
auf Antrag von

Prof. Susan Gasser (Fakultätsverantwortliche)

Dr. Botond Roska (Dissertationsleiter)

Prof. Ernst Bamberg (Korreferent)

Basel, den 25.05.2010

Prof. Dr. Eberhard Parlow (Dekan)

Introduction	3
<i>The mammalian retina</i>	3
<i>Phototransduction cascade</i>	4
<i>Light adaptation and microRNAs as molecular regulators</i>	5
<i>Retinitis Pigmentosa</i>	5
<i>“Optogenetic” tools</i>	6
<i>Retinal gene transfer</i>	7
Chapter 1 - Genetic reactivation of cone photoreceptors restores visual responses in Retinitis pigmentosa	10
<i>Abstract</i>	11
<i>Results and discussion</i>	11
<i>Supplementary discussion</i>	22
<i>Supplementary figures</i>	25
<i>Supplementary tables</i>	35
<i>My contribution</i>	37
Chapter 2 - Characterization of microRNAs induced by light adaptation in mouse retina reveals rapid turnover as a common property of neuronal microRNAs	38
<i>Summary</i>	39
<i>Introduction</i>	39
<i>Results</i>	41
<i>Discussion</i>	60
<i>Supplemental figures</i>	65
<i>Supplemental tables</i>	76
<i>Supplemental table legends</i>	78
<i>My contribution</i>	79

Chapter 3: Side projects	80
3.1 - <i>Genetically timed, activity-sensor and rainbow transsynaptic viral tools</i>	80
<i>Abstract</i>	80
<i>My contribution</i>	80
3.2 - <i>KAP1-mediated epigenetic repression in the forebrain modulates behavioral vulnerability to stress</i>	81
<i>Abstract</i>	81
<i>My contribution</i>	81
3.3 – <i>Light-activated channels targeted to ON bipolar cells restore visual function in retinal degeneration.</i>	82
<i>Abstract</i>	82
<i>My contribution</i>	82
Summarizing Discussion	83
Material and Methods	85
<i>Chapter 1: Material and Methods</i>	85
<i>Chapter 2: Experimental procedures</i>	99
<i>Chapter 2: Supplemental experimental procedures</i>	101
<i>Chapter 3.1 - Methods</i>	114
<i>Chapter 3.2 – Methods</i>	114
<i>Chapter 3.3 –Methods</i>	115
References	116
Curriculum Vitae of Volker Busskamp	120

Introduction

The mammalian retina

The retina is a light sensory organ lying in the back of the eyeball. This neural tissue consists of five major neuronal cell classes which are organized in three

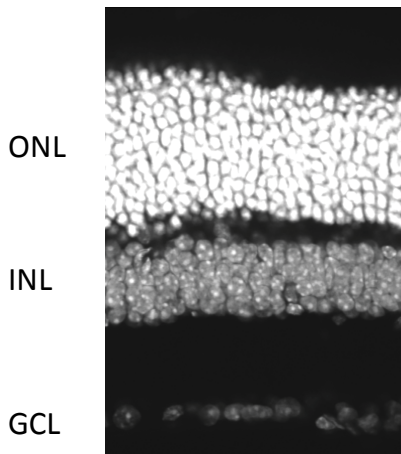


Figure 1 Retinal cross section, nuclear layers are shown in white (DAPI staining)

nuclear layers. There are two types of photoreceptors in the outer nuclear layer (ONL); rods for low light levels and cones for bright light, acuity and color vision. Photoreceptors lie at the back of the retina and their light-sensitive cell compartments, the outer segments (OS), are embedded in the retinal pigment epithelium (RPE). Light has to pass through the entire

transparent tissue to stimulate the receptor cells. The second layer is named inner nuclear layer (INL) and consists of excitatory bipolar cells,

inhibitory horizontal cells and amacrine cells. The ganglion cell layer (GCL) forms the third cell layer and is occupied by ganglion and amacrine cells. Ganglion cells have axons that reach to higher visual brain centers. The photoreceptors are connected to bipolar and horizontal cells in the outer plexiform layer (OPL). In the inner plexiform layer (IPL), bipolar cells are linked to amacrine and ganglion cells. Synaptic connections are made in these plexiform layers. The OPL and IPL are largely devoid of cell bodies (1).

The retina has to be considered as a delocalized brain area specialized to sense light signals and process this information before relaying it to further downstream brain centers. The vertical excitatory signal flow is shown in Figure 2.

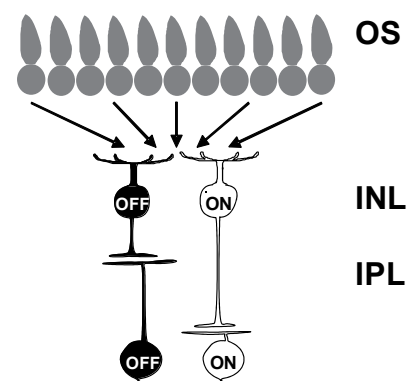


Figure 2 Scheme of excitatory retinal signal flow

Many photoreceptors convert light signals into chemical signals that a few downstream bipolar cells read and transmit to a ganglion cell. At the bipolar cell

level, light information also diverges into two major pathways, one being activated by increments of light (ON) and the other one by decrements of light (OFF). Morphologically, OFF bipolar cells meet OFF ganglion cells in the more upper part of the IPL whereas corresponding ON cells are connected in the lower IPL. At least ten types of bipolar cells lead to a formation of different parallel channels in the retina, each representing a different aspect of the visual input (2, 3) Higher grades of signal processing are mediated by inhibitory horizontal cells (in the OPL) and amacrine cells (in the IPL). In ganglion cells, these processed signals are coded into action potentials that are transmitted via axons to the higher visual centers.

Phototransduction cascade

The initial step of visual perception is the detection of photons by photoreceptive pigments, called opsins, in the outer segments of photoreceptor cells.

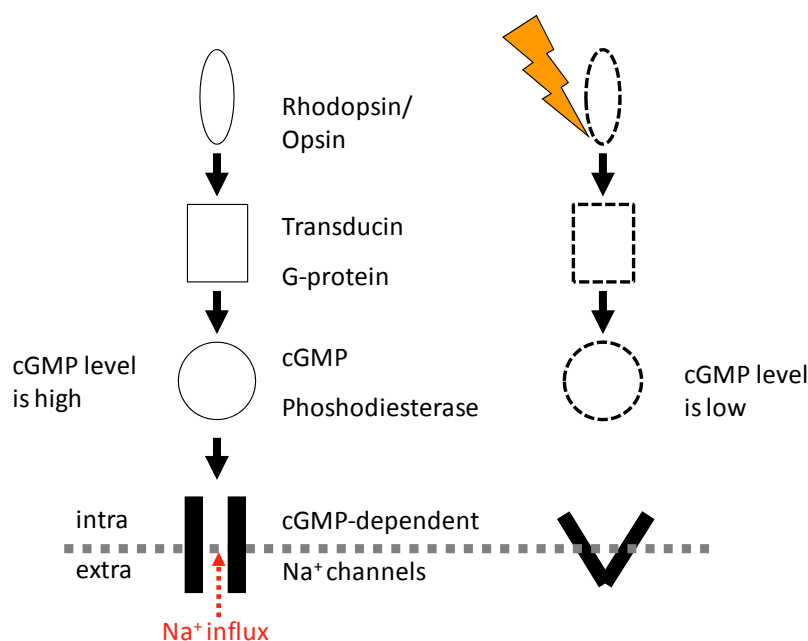


Figure 3 Scheme of the phototransduction cascade

The impact of a photon on an opsin changes its conformation and a G-protein signal cascade starts. Activated G-protein subunits activate a phosphodiesterase that reduces the cellular concentration of the second messenger cyclic

GMP (cGMP). Low cellular cGMP levels induce the closure of cGMP-dependent Na⁺ channels. If positive ions stop diffusing through the channels into the photoreceptor cell, the membrane voltage becomes more and more negative relative to the outside. This hyperpolarization blocks the release of the neurotransmitter glutamate to the synaptic cleft at the photoreceptor terminal.

Differences in glutamate concentrations in the synaptic cleft are detected by downstream bipolar and horizontal cells and at this point, light signals are translated into neurochemical signals. Photoreceptors are depolarized in the dark and continuously release glutamate. The involvement of a signal cascade slows down the signal flow but more importantly, it amplifies the signal giving the detecting system a high sensitivity. A set of other proteins is involved in stopping, recharging and maintaining the phototransduction cascade (4). The phototransduction cascade is very similar between rod and cone photoreceptors but differs in the protein variants leading to spectral and sensitivity differences.

Light adaptation and microRNAs as molecular regulators

One important feature of the retina is its ability to adapt and maintain light sensitivity over an enormous range of light intensities. This adjustment increases sensitivity of the visual system at low light levels by improving the signal-to-noise ratio and prevents saturation at high light levels. Adaptation takes place at different levels in the retina, both in photoreceptors (5, 6) and in inner retinal neurons (7). The temporal features also range from millisecond timescales to hours. At longer timescales, light adaptation at the cellular level involves changes of gene expression that set the cell to the adapted state. Little is known about the cellular events that control the changes in gene expression. Recent research draws the attention to small non-coding RNA molecules, microRNA (8). These 21 nucleotide single-stranded RNA molecules interact with messenger RNA (mRNA) molecules and influence their translation to proteins by degrading mRNA or its removal from the translational machinery. According to target binding algorithms, microRNA molecules have the potential to bind and thereby affect various cellular mRNA targets. (8) The field of microRNA research is relatively young especially in the retina and many cellular functions of microRNAs have yet to be explored, exciting my exploratory interest.

Retinitis Pigmentosa

Retinitis pigmentosa (RP) refers to dysfunctions of retinal function leading to the loss of vision (9). Historically, RP was thought to be an inflammation of the retina but intensive research over the last 150 years tracked back the cause of

the disease to genetic lesion (10). These mutations primarily affect rod photoreceptors and affect genes involved in the phototransduction cascade, cellular structure (such as the outer segments), transcription factors, photoreceptor catabolism, mitochondrial metabolism and also many genes of unknown function. Today, more than 100 mutations in 44 genes have been mapped that affect rod photoreceptors, all leading to a similar pathology. Normally, the onset of the disease in humans is in their adulthood, leading to night blindness. Dysfunctional rod photoreceptors start to die from the retinal periphery. This retinal degeneration (RD) progresses to the central part of the retina also affecting cone photoreceptors leading to a loss of daytime vision and visual acuity. The lingering degeneration can cause overall blindness. Treating RP patients is a very difficult task not only due to RP's genetic complexity but also the fact that the patients realize their condition too late after the onset of rod photoreceptor death. Most therapies aim to slow down retinal degeneration to preserve resting vision. It was postulated that cone photoreceptor cells follow rods in degeneration leading to a photoreceptor free retina. Recent research (11) indicated that cones change their morphology and lose their light-sensing outer segments but persist in a non-functional dormant state. However, the loss of OS makes cones light-insensitive and it is unknown if remaining cone photoreceptors are accessible for therapeutic intervention.

“Optogenetic” tools

In our visual system photoreceptors with their phototransduction machinery convert photons to chemical signals. In prokaryotic organisms, single proteins mediate light sensation. Intensive screening and characterization has provided us with a genetic toolbox of light-sensing proteins, called optogenetic modulators (12-14). If these genes are exogenously expressed in neurons, one can activate (depolarize) or silence (hyperpolarize) the cells simply by shining light. Because a single gene mediates light sensitivity and substitutes for an entire phototransduction cascade, optogenetic tools are ideal candidates to confer light sensitivity to disease-caused light-insensitive retinas. This approach was shown to restore light perception in animal models of RP by creating artificial photoreceptors out of inner retinal neurons (15-17).

Retinal gene transfer

The big challenge is to deliver genes to retinal cells in a cell-type-specific manner. The three main parameters are timing (regarding retinal development or disease onset, for example), efficiency and specificity of gene expression in targeted cells. One way is to simply inject naked DNA molecules close to retinal cells and induce the uptake by electric pulses. This technique is called *in vivo* electroporation (18). One advantage is the possibility of delivering genes without size limitations but on the other hand, there is only a short window during retinal development for intervention leading to stable gene expression. The use of cell-type-specific promoters can make this gene transfer specific but the overall efficiency would be very low (19). Viral delivery tools bear several advantages for efficiency and specificity and can be used to bring genes into the developing as well as into the adult retina. The most commonly used gene delivery tool resorts to non-pathogenic Adeno-Associated-Viruses (AAV) (20). These relatively small viral capsids (20 nm in diameter) contain 4.7kb single-stranded DNA genomes. Recombinant AAVs are exploited for their viral genes and promoters except the genome flanking inverted tandem repeats (ITRs). The rest of the AAV genome can be replaced by engineered DNA fragments of choice. Cell type expression patterns can be obtained by using cell type specific promoters and by modifying the viral capsids. AAV capsid proteins interact with host cell surface receptors and pseudotyping (using capsid proteins from other AAV types) influences host cell tropism. AAVs are easy to produce (genome generation and assembling to infectious particles), they do not replicate in host cells and their genomes persist in the host cell genomes as stable episomal DNA aggregates. In combination with chosen promoters, the expression of genes from AAV genomes can be very efficient and stable for longer periods. AAVs are used for human gene transfer approaches (21). The retina is predestined for using AAVs because it lies at the back of the eyeball which as a closed compartment reduces diffusion of injected AAV particles. One can also control the injection site. A subretinal injection targets mostly RPE and the ONL whereas intra vitreal injections promote AAV uptake in ganglion and INL cells.

Chapter 1: Genetic reactivation of cone photoreceptors restores visual responses in Retinitis pigmentosa

My main project dealt with the functional repair of light-insensitive morphologically-altered cone photoreceptors in RP mouse models. The idea was to introduce a hyperpolarizing optogenetic tool into persisting cone photoreceptors after complete rod degeneration to retinas of mice suffering from slow and fast forms of retinal degeneration (s-RD and f-RD mice).

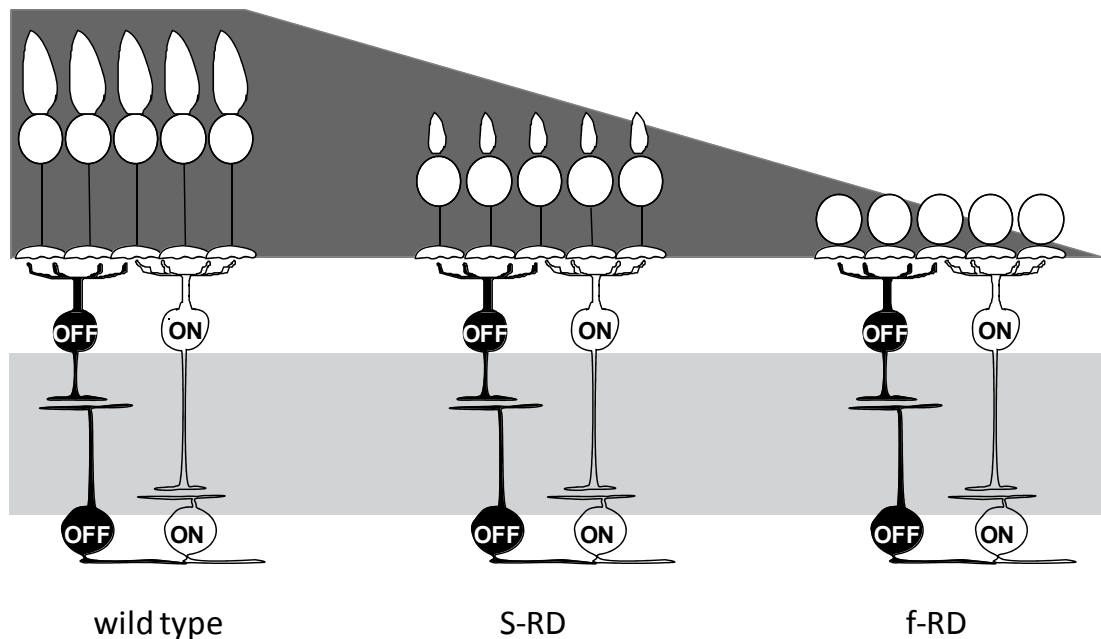


Figure 4 Scheme of RD forms (ONL in dark gray, IPL in light gray).

The functional reactivation of photoreceptors at the entry level of light perception was advantageous for preserving downstream retinal processing to restore vision and not only light perception. I will show reactivated sophisticated and complex vision in former blind mice, as well as the first steps for translating this biomedical approach from mice to humans.

Chapter 2: Characterization of microRNAs induced by light adaptation in mouse retina reveals rapid turnover as a common property of neuronal microRNAs

The field of microRNA research in the retina but also in general is relatively young and little is known about microRNA functions. My second more basic research project was to study the functional roles of microRNA in the retina.

Everything started with a screen of expressed microRNA in the mouse retina at two states of light adaptation conditions: dark or light adapted. Differences in microRNA level in dependence of the light adaption state revealed a rapid turnover of these small molecules in the retina and more generally in neurons. I contributed to the understanding of how light adaptation occurs at the molecular level in photoreceptors and that microRNA levels can be highly dynamic in neurons.

Chapter 3: Side projects

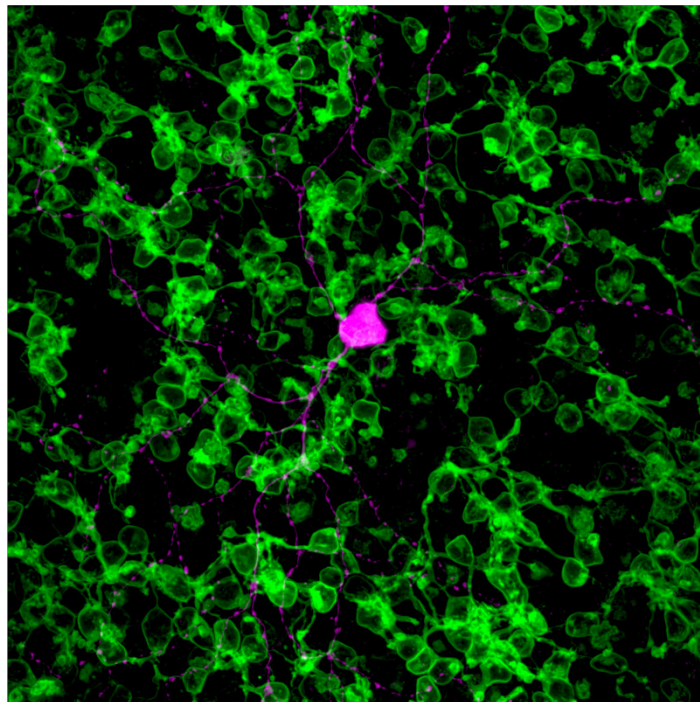
During my PhD thesis, I made molecular tools, such as the generation of a transgenic mouse line that expresses a calcium sensor in a subset of retinal cells (22) In another project, I used *in silico* approaches to identify target molecules whose expression might be altered in the hippocampus due to the manipulation of epigenetic repression. I verified *in silico* results by combining robotics with high throughput quantitative real time PCR (23). Furthermore, I learned techniques for retinal gene transfer and contributed to the generation of artificial photoreceptors out of inner retinal cells to restore vision in a RP mouse model (16).

Chapter 1 - Genetic reactivation of cone photoreceptors restores visual responses in Retinitis pigmentosa

Volker Busskamp, Jens Duebel, David Balya, Mathias Fradot, Tim James Viney, Sandra Siegert, Anna C. Groner, Erik Cabuy, Valérie Forster, Mathias Seeliger, Martin Biel, Peter Humphries, Michel Paques, Saddek Mohand-Said, Didier Trono, Karl Deisseroth, José A. Sahel, Serge Picaud & Botond Roska

This work is published as a research article in Science

(Volker Busskamp, *et al.* *Science* **329**, 413 (2010))



(This image shows reactivated cones (green) that project on one retinal ganglion cell (magenta). This image served as the cover of the July 23rd 2010 Science issue)

Abstract

Retinitis pigmentosa refers to a diverse group of hereditary diseases that lead to incurable blindness, affecting two million people worldwide. As a common pathology, rod photoreceptors die early, whereas light-insensitive, morphologically altered cone photoreceptors persist longer. It is unknown if these cones are accessible for therapeutic intervention. Here, we show that expression of archaeobacterial halorhodopsin in light-insensitive cones can substitute for the native phototransduction cascade and restore light sensitivity in mouse models of retinitis pigmentosa. Resensitized photoreceptors activate all retinal cone pathways, drive sophisticated retinal circuit functions (including directional selectivity), activate cortical circuits, and mediate visually guided behaviors. Using human ex vivo retinas, we show that halorhodopsin can reactivate light-insensitive human photoreceptors. Finally, we identified blind patients with persisting, light-insensitive cones for potential halorhodopsin-based therapy.

Results and discussion

Retinitis pigmentosa (10, 24) is the result of diverse mutations in more than 44 genes expressed in rod photoreceptors (25); which then degenerate, causing loss of night vision. Subsequently, cone photoreceptors, which are responsible for color and high-acuity daytime vision, progressively lose their photoreceptive outer segments, leading to overall blindness. Despite this loss of sensitivity, cone cell bodies remain present longer than rods in both humans and animals (11, 26, 27) but it is not known whether these light-insensitive cells can be reactivated or if information from them can still flow to downstream visual circuits (Fig. 1A) for a substantial time window after the loss of photosensitivity (28).

To restore light-evoked activity in light-insensitive cone photoreceptors we genetically targeted a light-activated chloride pump (12, 29, 30), enhanced *Natronomonas pharaonis* halorhodopsin (eNpHR) (14, 31), to photoreceptors by means of adeno-associated viruses (AAVs) (32, 33). Light-activated chloride pumps are rational candidates for reactivating vertebrate photoreceptors as both eNpHR-expressing cells (14) and healthy photoreceptors hyperpolarize in

response to increases in light intensity. We selected two animal models of *Retinitis pigmentosa* for gene therapy, both of which lead to retinal degeneration (RD). *Cnga3^{-/-}; Rho^{-/-}* double-knockout mice served as a model of slow forms of RD (s-RD mice) (34), and *Pde6b^{rd1}* (also known as rd1) mice as a model of fast forms of RD (f-RD mice) (35). Targeted expression of eNpHR was accomplished with the use of three cell-specific promoters (Fig. 1B): (i) human rhodopsin (hRHO) (36); (ii) human red opsin (hRO) (37); and (iii) mouse cone arrestin-3 (mCAR)(38).

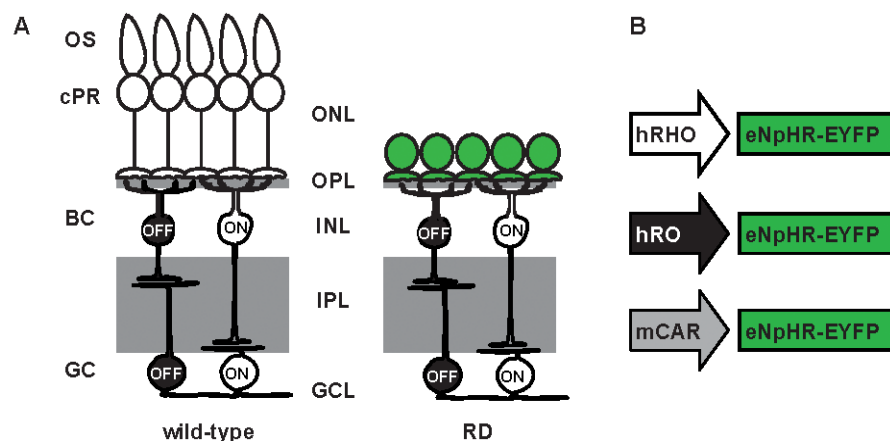


Figure 1. Scheme of the excitatory pathways of cone retinal circuitry in WT and RD retinas. **(A)** Cone photoreceptors (cPR) in WT retinas (left) detect light with photopigments in their outer segments (OS). Cone cell bodies are located in the outer nuclear layer (ONL). Cones provide input to ON and OFF bipolar cells (BC) that have cell bodies in the inner nuclear layer (INL). Bipolar cells are connected to corresponding ON and OFF ganglion cells (GC). Ganglion cell bodies are in the ganglion cell layer (GCL), and their axons relay visual information to higher visual centers. The locations of inhibitory interactions mediated by horizontal cells in the outer plexiform layer (OPL) and by amacrine cells in the IPL are indicated by gray boxes. Light-insensitive RD cones (right) lack outer segments, but their cell bodies (green) persist longer than rods. **(B)** AAV-expression constructs. hRHO, hRO, or mCAR promoters drive eNpHR-EYFP.

To assess the effectiveness and specificity of the promoters, we used eNpHR fused to enhanced yellow fluorescent protein (31) (EYFP) (Fig. 2, A to I). It is important to restrict the expression of eNpHR to photoreceptors only, because eNpHR in downstream retinal circuit elements, such as ON-bipolar and ON-ganglion cells, may inhibit the flow of information across the retina. Enhanced green fluorescent protein (EGFP)-expressing AAVs were used as controls throughout this study (fig. S1). We selected the hRO and mCAR promoters for s-RD mice (Fig. 2, B and C) and the mCAR promoter for f-RD mice (Fig. 2F), on

the basis of their ability to selectively drive expression of eNpHR-EYFP in a high percentage of cone photoreceptors (figs. S2 and S3).

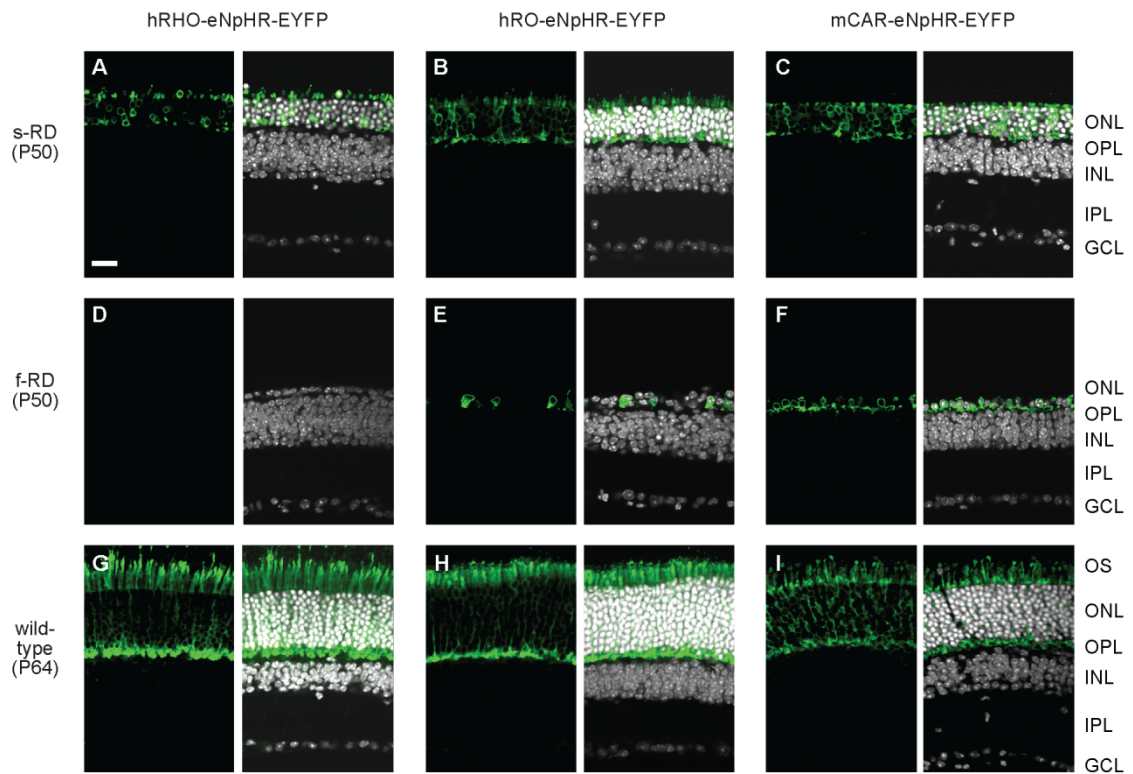


Figure 2. Targeted expression of a light-sensitive chloride pump in persisting photoreceptors in RD retinas. (A to I) Cross sections of GFP-immunostained (35) retinas transduced by hRHO- (A, D, G), hRO- (B, E, H), and mCAR- (C, F, I) eNpHR-EYFP AAVs in s-RD (A to C), f-RD (D to F), and WT (G to I) mice. Left panel of each pair, eNpHREYFP; right panel of each pair, co-stained with 4',6'-diamidino-2-phenylindole (DAPI). Scale bar, 20 mm.

The life span of cones in RDmice defines the window of opportunity for reactivation. Therefore, we tested EYFP or EGFP expression driven by the mCAR promoter at different time points during retinal degeneration. Surprisingly, EYFP and EGFP expression lasted more than eight months (Fig. 3A, fig. S4, last tested f-RD at postnatal day 264 (P264) and s-RD at P255), longer than opsin protein expression [~P95 (11) or between P21-P110 (39)] We isolated these long-lasting AAV- transduced cells from f-RD retinas at different time points and verified their identity by analyzing their transcriptome (P110 to P220, fig. S5). Cone-specific genes were expressed in the isolated cells, whereas markers of other retinal cell types were absent, suggesting that AAV-labeled cells are altered cones, even at later stages of degeneration. The fact

that opsin mRNA remained, whereas the opsin protein did not, suggests translational down-regulation of opsins, as also shown before (39). We estimate that ~27% of cones remain between P184 and P255 in s-RD and ~25% remain between P182 and P264 in f-RD mice (Fig. 3A).

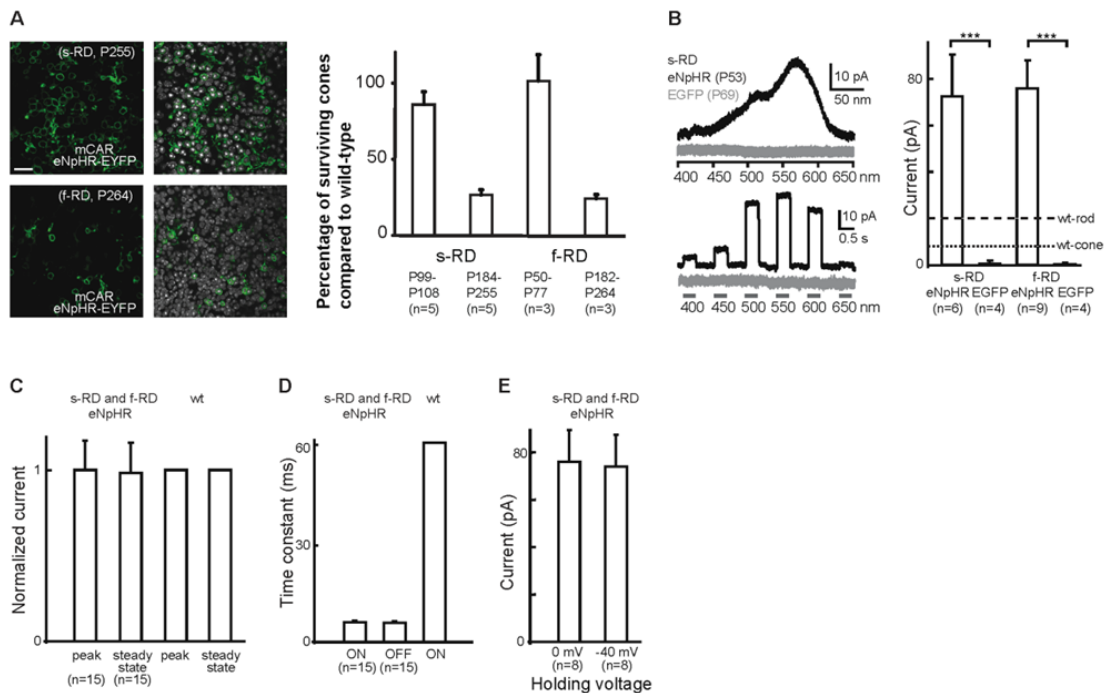


Figure 3. Light responses in surviving eNpHR-expressing RD cones. **(A)** (Left) Confocal top views of GFP-immunostained RD photoreceptors transduced by mCAR-eNpHR-EYFP in P255 s-RD (top) and P264 f-RD (bottom) retinas. Left panel of each pair, eNpHR-EYFP; right panel of each pair, co-stained with DAPI. Scale bar 20 mm. (Right) Estimated fraction of surviving cones (see Material and Methods) in s-RD and f-RD mice at different time points compared with WT cone numbers. n, number of retinas analyzed. **(B)** (Left) Photocurrent action spectrum of an eNpHR- (black) or EGFP- (gray) expressing s-RD cone. Top, color-ramp; bottom, light flashes. Gray bars indicate the timing of the full-field light stimuli. (Right) Magnitude of photocurrents in photoreceptors expressing eNpHR or EGFP. Dashed lines show the peak magnitude of photocurrents in WT cones (short dashes) and WT rods (long dashes). Stars indicate statistical significance (see Material and Methods). **(C)** Peak and steady-state photocurrents (0.5-s flash) in RD and WT animals. **(D)** Rise and decay time constants of eNpHR-mediated photocurrents compared with the rise time constant in WT photoreceptors. **(E)** eNpHR-mediated photocurrents in RD retinas at different holding voltages. Because the response properties in s-RD and f-RD mice were similar, the data from both mouse lines were grouped in panels **(C to E)**. All WT cone response data shown in Fig. 3 were taken from (40). Error bars indicate SEM.

We tested whether eNpHR drives cone light responses in RD retinas at an age (P53 to P264, table S1) when many (s-RD) (34) or all (f-RD) (39) rods have already died. eNpHR-EYFP-expressing photoreceptors in s-RD and f-RD

retinas displayed larger (Fig. 3B and fig. S6), more sustained (Fig. 3C), and significantly faster (Fig. 3D) photocurrents than those of wild-type (WT) cones. The photocurrents peaked at 580 nm. Photoreceptors expressing only EGFP did not react to light. The magnitude of photocurrents in eNpHR-transduced s-RD and f-RD mice were similar (Fig. 3B). The current size was independent of the holding voltage (Fig. 3E), a finding that is consistent with the view that the photocurrents are mediated by ion pumps (30). Photocurrents and voltages were modulated across three logarithmic units of intensities (fig. S6). In the absence of functional outer segments, which normally generate currents that depolarize photoreceptors in the dark, RD photoreceptors were expected to stay hyperpolarized. A hyperpolarized state would limit the ability of eNpHR currents to modulate synaptic transmission. However, the recorded eNpHR-expressing RD photoreceptors were depolarized in the dark [-26 ± 3 mV, $n = 12$ cones; see supporting online material (SOM)].

The ability of eNpHR-reactivated RD photoreceptors to convey information to downstream retinal circuits depends on the presence of functional photoreceptor-to-bipolar cell synapses. As retinal degeneration progresses, these synapses morphologically reorganize (25). However, they still possess elements of both pre- and postsynaptic machinery (11). To test for potential signal flow from photoreceptors to ganglion cells, we recorded excitatory currents from ganglion cells, the output neurons of the retina. Ganglion cells in eNpHR-transduced s-RD and f-RD retinas displayed robust, light-evoked excitatory currents (Fig. 4A), indicating functional outer and inner retinal synaptic connections. The magnitudes of these excitatory currents were comparable to those in WT retinas (Fig. 4A). There were no measurable light-evoked currents in the ganglion cells of retinas transfected with EGFP (Fig. 4A).

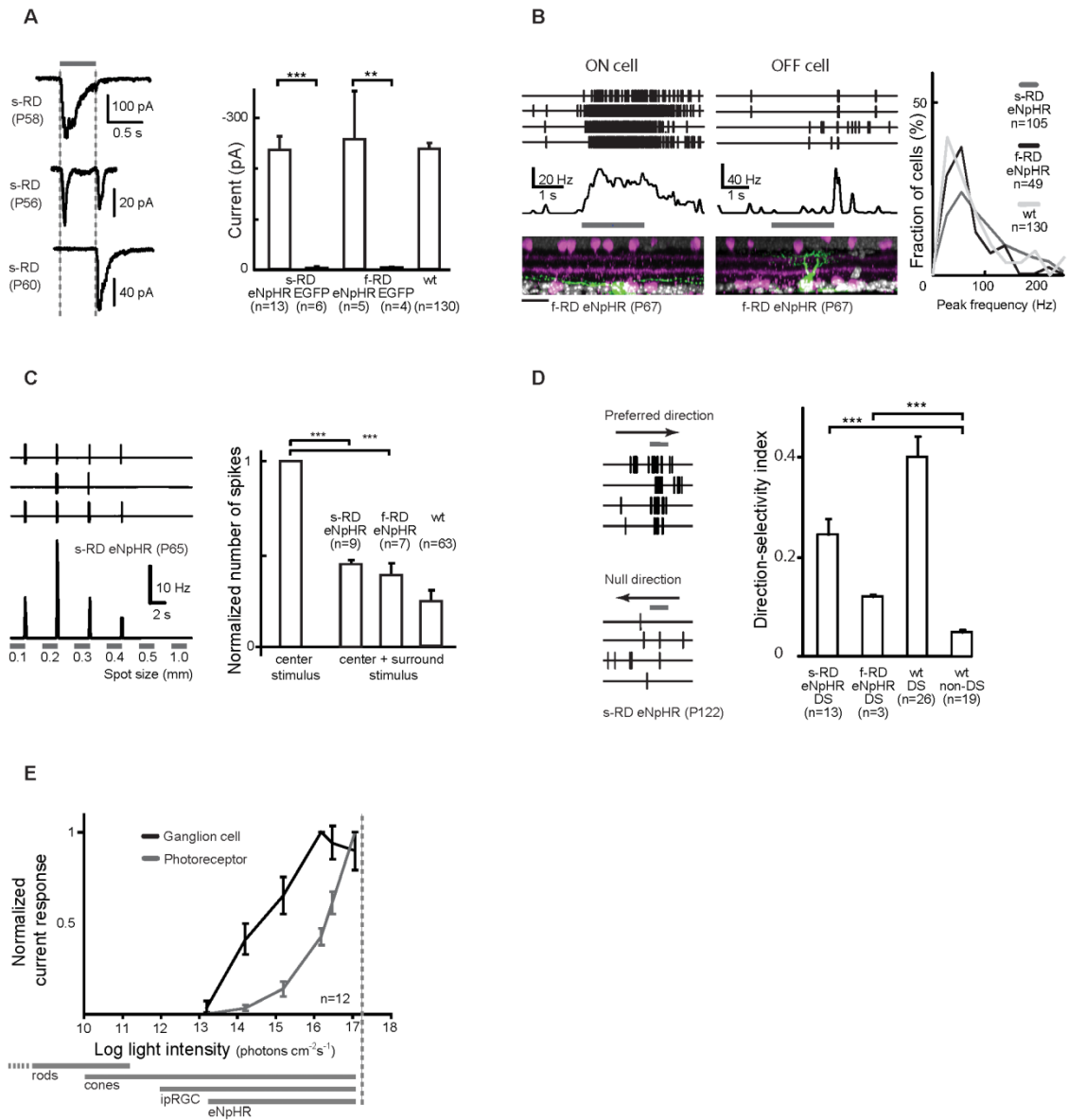


Figure 4. Light responses in eNpHR-expressing RD retinas. For each functional test, individual examples are shown on the left, followed by statistics on the right. **(A)** Ganglion cell excitatory currents. (Left) Light-evoked excitatory currents in ON (top), ON-OFF (middle), and OFF (bottom) ganglion cells in eNpHR-expressing s-RD retinas. Gray bars show the timing of the full-field light stimulus. (Right) Magnitude of light-evoked peak excitatory currents in s-RD, f-RD, and WT mice; ON, OFF, and ON-OFF cells are pooled together. Full-field stimulus was used. **(B)** Ganglion cell spiking output. (Left) Top, spike recordings (four repetitions) from ON (left) and OFF (right) ganglion cells from an eNpHR-expressing f-RD retina; middle, spike frequency responses (gray bar shows the timing of a full-field light stimulus); bottom, corresponding cells filled with neurobiotin (green), choline acetyltransferase (magenta) as an IPL stratification marker, and DAPI staining (white) to visualize nuclear layers. (Right) Peak spike frequency distribution in response to full-field flash stimuli in s-RD, f-RD, and WT retinas. **(C)** Lateral inhibition. (Left) Top, spike trains from an OFF ganglion cell in response to light stimulation with a white spot of increasing size (three repetitions); bottom, corresponding spike frequency. (Right) Number of spikes evoked by 1-mm

diameter spot stimuli (center + surround stimulus) relative to the number of spikes evoked by a 0.1- to 0.2-mm spot (center stimulus). **(D)** Directional selective responses. (Left) Spike recordings during stimulation with a fast-moving bar (width, 200 μm ; speed, 1.5 mm s^{-1} ; four repetitions) in the preferred direction (top) and in the opposite direction (“null” direction, bottom). Stimulus timing is shown by gray bars. (Right) Direction-selectivity index (see Materials and Methods (41)). **(E)** Light sensitivity. eNpHR-induced excitatory current responses in ganglion cells and photocurrents in photoreceptors as a function of light intensity. The gray lines at the bottom display the ranges of sensitivities for rods (only partially shown), cones, and intrinsically photosensitive ganglion cells (ipRGCs). The maximum light intensity at 580 nm allowed in the human eye, according to the 2006 European directives on artificial optical radiation (42), is shown by the vertical dashed line. In all panels, n, number of different cells from which we took our measurements; error bars, SEM; stars, statistical significance (see Materials and Methods). Light intensity was 10^{16} photons $\text{cm}^{-2} \text{s}^{-1}$ for each experiment.

The retina incorporates two major information channels that diverge at the level of bipolar cells and are physically separated by depth within the inner plexiform layer (IPL). ON cells are activated by light increments, whereas OFF cells are activated by light decrements (43). The activity of ganglion cells is coded by action potentials (“spikes”) that form the output signal of the retina (44) and the input signal to higher brain centers. Notably, light stimulation evoked excitatory currents and spiking activity in ganglion cells of eNpHR-transduced RD retinas, either at light increments, light decrements, or both (P53 to P264; Fig. 4, A and B). The dendritic processes of morphologically reconstructed ganglion cells were properly aligned in the corresponding ON or OFF strata (45) of the IPL (Fig. 4B). Ganglion cell spike frequencies spanned similar ranges in s-RD, f-RD, and WT retinas (Fig. 4B). Some ganglion cell types respond preferentially to changes in illumination and therefore spike transiently after a light step, whereas others represent the level of illumination and thus spike in a more sustained manner. The dynamics of spiking activity in eNpHR-transduced retinas varied from transient to sustained, as in WT retinas (fig. S7). Light-stimulation of eNpHRreactivated photoreceptors in RD retinas even evoked ganglion cell spiking activity at later stages of degeneration (s-RD: <P255, f-RD: <P264; fig. S7).

We next asked if basic forms of spatial processing were functional in the eNpHR-transduced RD retinas. Lateral inhibition is a conserved feature of vertebrate retinas that is important for spatial contrast (“edge”) enhancement.

When spots of increasing sizes were presented to eNpHR-expressing RD retinas, the response magnitude of ganglion cells reached a maximum and then gradually decreased, a sign of lateral inhibition (Fig. 4C and fig. S7) (43, 46). Lateral inhibition also results in ON-center, OFF-surround responses (43) that we were able to observe in eNpHR-expressing RD retinas (fig. S7). Another example of spatial processing is the directionally selective responses of types of ganglion cells to motion stimuli (47). The activity of directional selective ganglion cells is important for the optokinetic reflex (48). When eNpHR-transduced RD retinas were stimulated with bars moving in different directions, some ganglion cells responded preferentially to motion in a particular direction but produced little activity when the bar moved in the opposite direction (Fig. 4D) (49). This response asymmetry suggests that the retinal circuit for directional selectivity is, at least partially, maintained in RD retinas.

The sensitivity of eNpHR to light is less than that of normal cones (Fig. 4E), and although normal cones can adapt to different light intensities, eNpHR-driven cones have a fixed sensitivity range (see SOM). However, the sensitivity of ganglion cells to light was 1.7 log units higher than that of the eNpHR-expressing photoreceptors (Fig. 4E), and the light levels required for eNpHR stimulation at 580 nm are below the limit allowed for safe radiation of the human eye, according to the 2006 European directives on artificial optical radiation (Fig. 4E) (42).

The slow and fast RD mouse models not only differ in the time course of photoreceptor degeneration, but also in the amount of light-driven activity present during development. s-RD mice have no light-sensitive rod-cone system during development (34), whereas f-RD mice lose the rod-cone function gradually and are blind by 4 weeks of age (35). In the retina, the responses in eNpHR-activated s-RD and f-RD mice were similar, suggesting that the development of the tested retinal functions, like direction selectivity, may not require light-driven input from rods and cones. Light stimulation of the eyes resulted in visually evoked potentials in eNpHR-expressing f-RD mice but not in EGFP-transduced controls (P42 to P118, fig. S8). In contrast to the retina, we could not measure light-driven cortical activity in eNpHR-transduced s-RD mice.

We next evaluated whether light could induce behavioral changes in eNpHR-transduced mice. In dark-light box tests (50), eNpHR-expressing f-RD and s-RD mice performed significantly better than the corresponding EGFP-expressing control groups (P44 to P143, Fig. 5A), and the increased performance depended on the illumination level (Fig. 5B). In the optomotor reflex test (51), only eNpHR-expressing f-RD mice performed better than EGFP-expressing control mice at a variety of drum speeds (P69 to P153, Fig. 5C). WT (fig. S8) and f-RD responses both peaked at the same speed. The optimum spatial frequency was higher for WT animals [0.26 cycles per degree (cpd)] compared to f-RD (0.13 cpd). These experiments demonstrated that resensitized photoreceptors are able to drive visually guided behavior in f-RD mice and, to some extent, in s-RD mice.

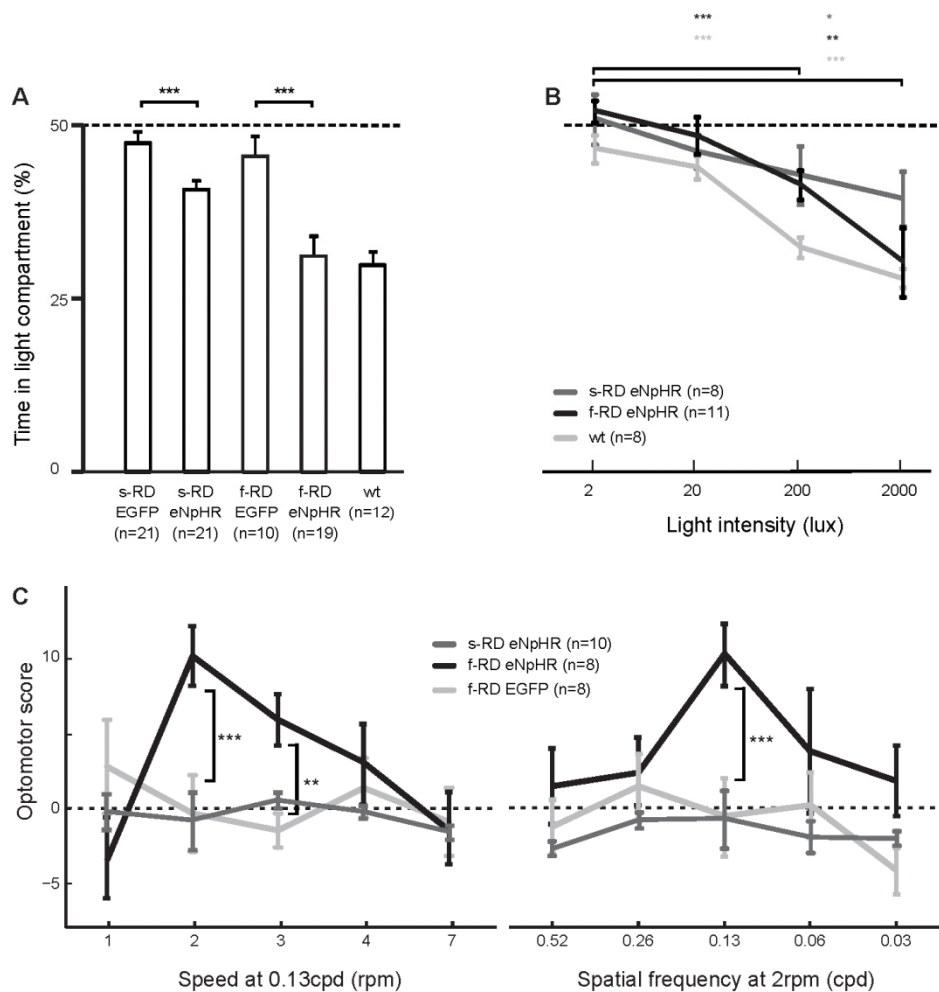


Figure 5. Visually guided behavior in eNpHR-expressing RD mice. **(A)** Dark-light box experiment. Percentage of time the AAV-injected RD animals and WT mice spent in the light compartment. **(B)** Darklight box test. Percentage of time mice spent in the light compartment as a function of light intensity. **(C)** Optomotor response score of eNpHR- or EGFP-expressing RD animals at different rotational speeds and spatial frequencies. rpm, revolutions per minute. In all panels, n, number of different animals; error bars, SEM; stars, statistical significance (see Materials and Methods).

To test for potential toxicity of eNpHR or the unmodified NpHR, we first compared the retinas of eNpHR-transduced WT mice (6 weeks after AAV administration) with those of normal WT mice. The number of photoreceptors was similar in both conditions (fig. S9), and, in addition to the light-induced spiking activity, ganglion cells in eNpHR-transduced WT retinas had a wider action spectrum (a gain of function at longer wavelengths) than ganglion cells in uninjected WT retinas (fig. S9). This suggests that both intrinsic opsins and eNpHR are at work. Next, we compared the retinas of transgenic mice expressing NpHR in photoreceptors under the control of a bovine rhodopsin promoter with WT retinas and found similar numbers of photoreceptors (at P140, fig. S9). These results suggest that, in the studied time window, neither the unmodified NpHR nor eNpHR induced additional photoreceptor degeneration.

The translation of gene therapy achieved in mice to human participants requires the use of promoters and AAV serotypes that drive photoreceptor-specific eNpHR expression in human retinas. Therefore, we tested our AAVs on human *ex vivo* retinal explants (Fig. 6A), which we could keep in culture for 2 to 3 weeks. Because of this short time window and the relatively long period of time required to efficiently express eNpHR from AAVs, we had to use immunohistochemistry to visualize eNpHR-EYFP protein expression in the cultured human retinas. Of the three promoters, mCAR directed expression of eNpHR specifically in human photoreceptors (fig. S10). To reduce the time required to obtain robust eNpHR-EYFP expression, which is necessary for two-photon laser-targeted electrophysiology, we inserted the mCAR-eNpHR construct into a lentiviral vector (fig. S10) (52). Using this new vector, we found high levels of eNpHR expression, specifically in human photoreceptors after only 1 to 2 days of incubation (Fig. 6B and fig. S10). Brightly labeled

photoreceptors in the parafoveal region displayed photocurrents and photovoltages with spectral tuning reflecting eNpHR activation (Fig. 6C and fig. S10). We could not measure any photocurrents from control human retinas, even at the time when the retina was isolated.

To find potential patients with retinitis pigmentosa eligible for eNpHR-mediated restoration of visual functions, we screened a database (see SOM) that contained records of retinal images acquired by optical coherence tomography (OCT), Goldman visual field tests, multifocal electroretinograms (ERGs), full-field ERGs, and visual acuity tests. We identified legally blind patients (data from one of whom are shown in Fig. 6 and fig. S11) with no visible outer segments on OCT pictures, but cone cell bodies in the central region. These criteria may be used in the future for selecting patients who could benefit from this therapy.

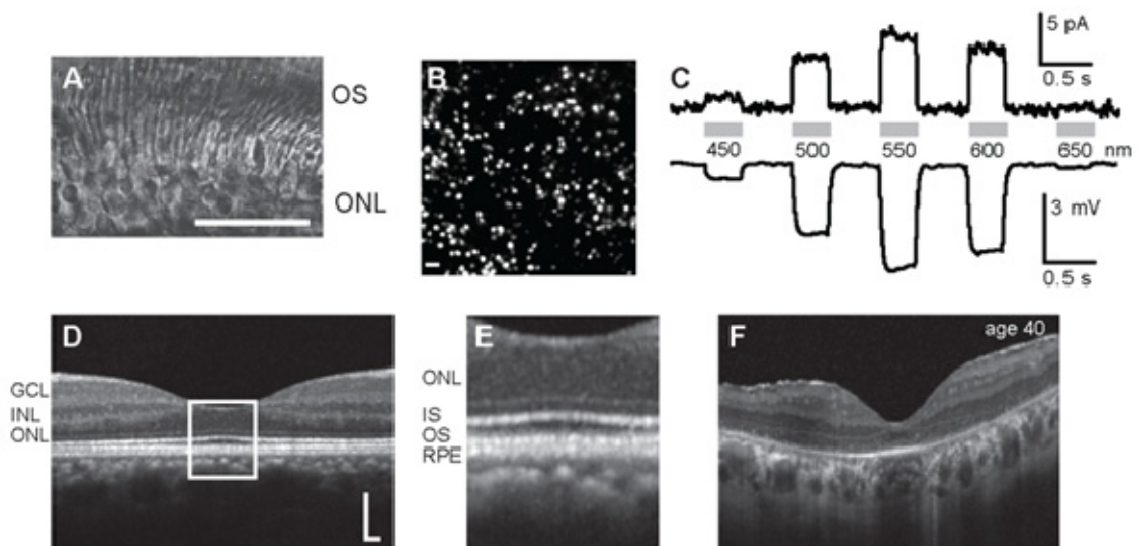


Figure 6. Translational aspects of eNpHR-EYFP-mediated reactivation of photoreceptors. **(A)** Retinal slice from a human retinal explant (24 hours postmortem). Scale bar, 30 mm. **(B)** Fluorescent live image of a lentivirus-transfected area from a human retina after 7 days in culture and 2 days after lentiviral administration. Scale bar, 20 mm. **(C)** Action spectrum of an eNpHR-expressing human photoreceptor stimulated with full-field light flashes ranging from 450 to 650 nm (top, current response; bottom, voltage response). Gray bars indicate the timing of the stimulus. **(D)** Representative OCT scan covering the foveal region of a healthy individual. **(E)** Magnified image. IS, inner segments; RPE, retinal pigment epithelium. Scale bar, 200 mm. **(F)** OCT from the left eye of a 40-year-old male patient with sporadic retinitis pigmentosa (loss of vision since the age of 15). Outer segments are undetectable.

We have shown that a microbial gene introduced to surviving cone cell bodies reactivated retinal ON and OFF pathways and the retinal circuitry for lateral inhibition and directional selective responses. Moreover, the reactivated cones enabled RD mice to perform visually guided behaviors. The tested time window of intervention was up to ~260 days in f-RD and s-RD mice, suggesting that persisting cone cell bodies (~25%) are enough to induce ganglion cell activity, even during later stages of degeneration. Our finding that AAVs with the mCAR promoter specifically transduced human photoreceptors and the identification of patients with little measurable visual function and no outer segments but surviving cone cell bodies suggest a potential for translating eNpHR-based rescue of visual function to humans (see SOM). In the future, eNpHR-based restoration may be combined with other approaches that increase the survival of altered photoreceptors (39, 53-55).

Supplementary discussion

Selecting patients for possible eNpHR-based gene therapy.

Possible criteria to stratify patients for eNpHR-based therapy include the following: No central visual field in Goldmann perimetry; legal blindness; and no visible outer segments on OCT pictures; but a layer of cone cells in the foveal region at least. There may, however, be several other factors for consideration when selecting patients. First, after losing central vision it is most often difficult to obtain good quality OCT due to the lack of fixation. Improved OCT imaging techniques (56) or, alternatively, a reversible blockade of muscle activity could overcome this difficulty. Second, the disappearance of the photoreceptor nuclear layer on OCT images may not necessarily be indicative of a complete photoreceptor loss: We found in the f-RD mouse model that, at later stages, the AAV-labeled cone cells did not form a distinct layer above the outer plexiform layer, but merged into the upper row of the inner nuclear layer. In *Retinitis pigmentosa* patients, even at late stages, the macula has a monolayer of cone cell bodies (27), which may not be detectable with current OCTs. New, high

resolution and fast scanning techniques (56) may facilitate the detection of even a single layer of cone cell bodies for eNpHR treatment. Third, we note that a major advantage of targeting remaining cone cell bodies with eNpHR, as compared with targeting bipolar or ganglion cells with channelrhodopsin (15, 16), is that, unlike cones, bipolar and ganglion cells are not arranged in a mosaic in the fovea (since these cells are moved away from the path of light in the fovea) and, therefore, light stimulation with patterns will cause spatially irregular activation of bipolar and ganglion cells. Fourth, we noted in both the transgenic mice expressing NpHR on a wild-type background, and also in eNpHR-EYFP-AAV-injected wild-type mice, that normal visual function was preserved in these mice, and eNpHR-induced additional light sensitivity at longer wavelengths. This finding implies that it may even be beneficial to consider targeting cones with eNpHR in patients that who have not completely lost central vision (57). Since eNpHR is less sensitive than normal cones, stimulation will require image intensifier goggles (see below) and we predict that in the absence of these goggles the remaining natural vision would not be affected. This later approach should only be considered if clinical results with patients without any central vision are established and safety is proved.

Light intensity requirements for eNpHR-based treatment.

Since eNpHR is not able to adapt to different intensities, stimulator goggles with an adaptive front sensor array and an LED array (42, 58) (or other patterned light source) facing the eye will be needed, independent of the exact sensitivity range of these halobacterial sensors. Without the goggles, if the mean light intensity is too low, halorhodopsins will not respond, or, if the mean light intensity is too high, halorhodopsins will be saturated. The key point is that the sensitivity of halorhodopsins is tuned to intensities that are safe to use in the human eye. In this respect, the red-shifted spectra (peak at 580nm) of halorhodopsins compared to that of channelrhodopsin (peak at 470 nm, blue light) is of importance since blue light has a higher potential for inducing photochemical damage than yellow light (42). We envision that adaptation to the different background intensities of the visual world will be achieved by artificial image sensors in the goggles, similar to those used in commercial video cameras. Nevertheless, new mutants and other types of light-activated

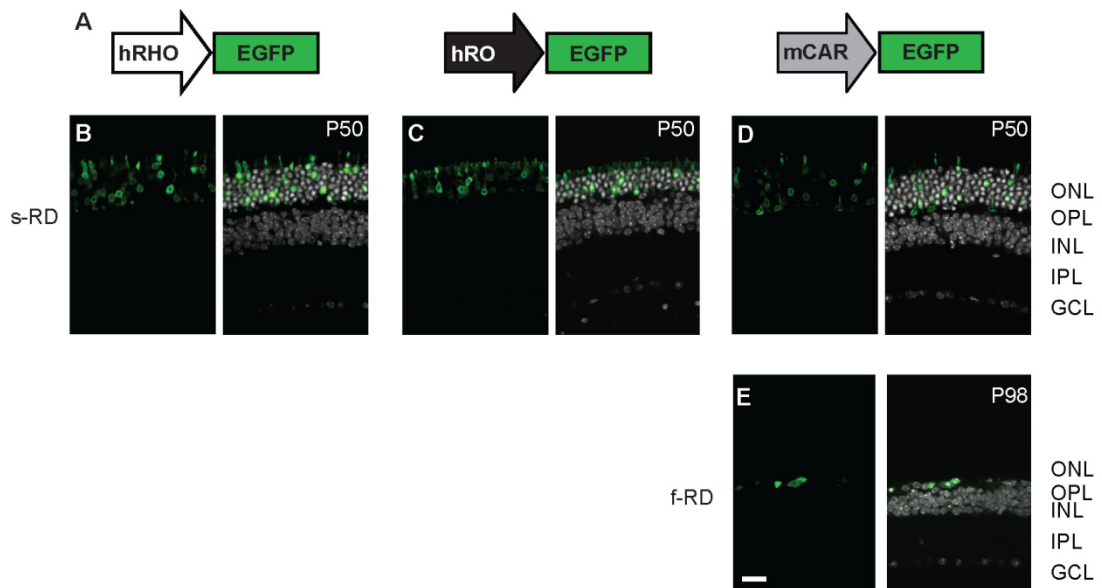
ion pumps (59) that produce more current per captured photon can make it even more sure that the light intensity required to stimulate the eye is safe (42). There are two factors that it may be worth balancing for potential clinical trials. On the one hand, increasing the sensitivity of eNpHR-transduced cones, by enhanced expression of eNpHR or by increased current per photon, is beneficial. On the other hand, if the regained visual sensation may, for some unforeseen reason, cause headache or tiredness after long light exposure, eNpHR stimulation could be simply turned off by removing the stimulation goggles. Finally, light-sensitive pumps activated at different wavelengths (59) may open the way for restoring color vision.

The state of cone photoreceptors in RD mice.

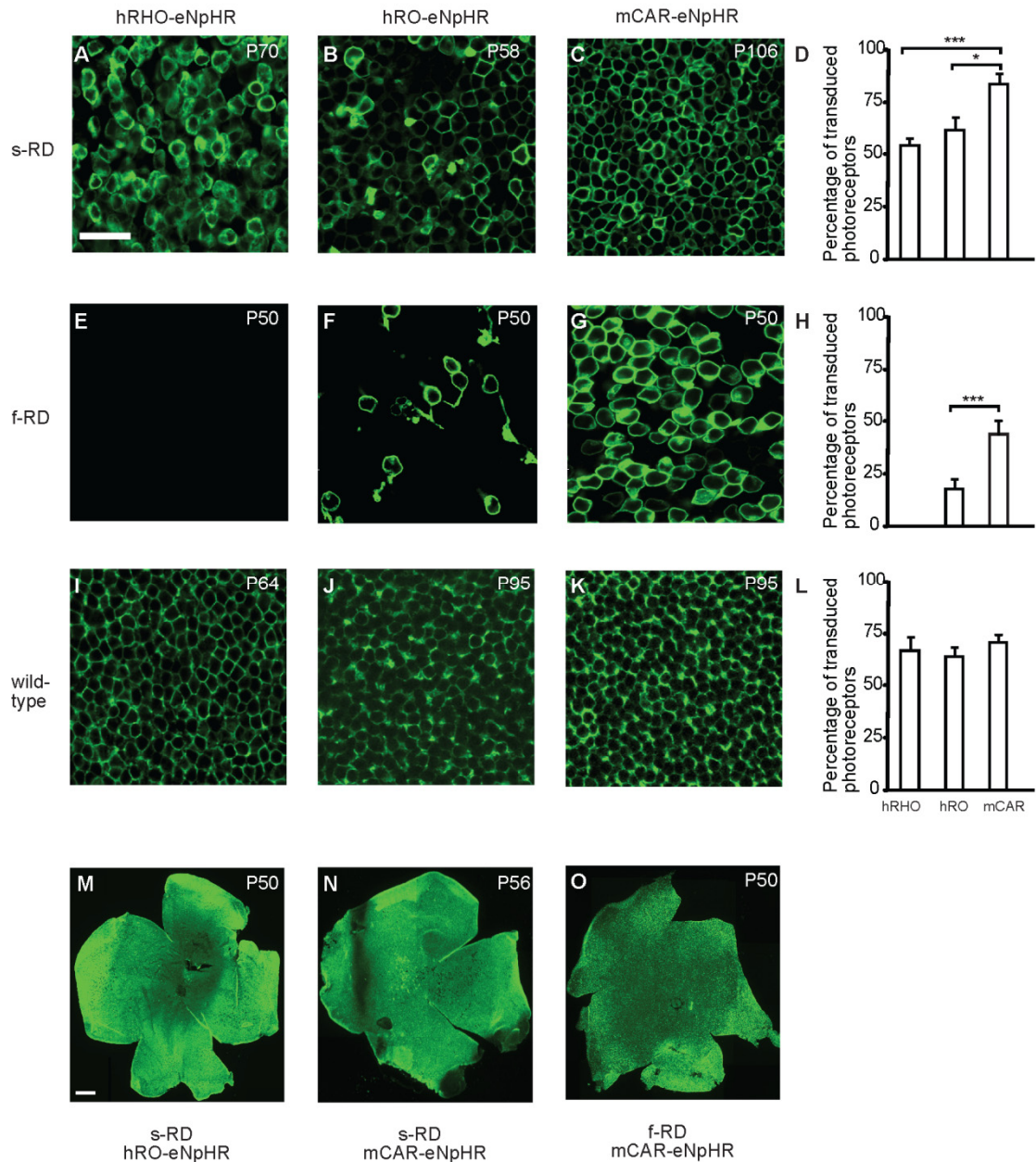
Cones of healthy retinas respond to light with hyperpolarization caused by the closure of cyclic-nucleotide gated (CNG) channels (60) located in the cone outer segment. CNG channels are open in the dark, and their closure is controlled through a molecular cascade induced by the capture of photons by opsins. In later stages of RD, the outer segment of cones degenerate and, therefore, one would expect no dark current and, consequently, a hyperpolarized cone. In contrast, we found that RD cone cell bodies were depolarized at -26 mV. Although the reason for the depolarized state is currently not understood, we speculate here about a mechanism. One possibility is that CNG channels in RD retinas are present in the remaining cone cell body but these channels are no longer modulated by opsins. However, this explanation is inadequate because the CNG channels are not functional (Cnga3^{-/-}) in s-RD mice, and CNG channel expression is low in f-RD mice (see Fig. S5). There are at least three other potential mechanisms. First, a compensatory mechanism may exist at the level of gene regulation that induces the expression of genes that keep the cell body in a depolarized state, for example by up-regulation of constitutively open Na⁺, Ca²⁺, or nonselective ion channels, either alone or in combination with the downregulation of K⁺ or Cl⁻ channels. Second, depolarization can be achieved by a ligand, present in RD but not wild type retinas, that opens Na⁺, Ca²⁺, or nonselective ion channels or closes K⁺ or Cl⁻ channels. Third, it is possible that the ion concentrations in the cone change in RD in such a way that a channel, for example a Cl⁻ channel,

may have a new driving force. This last possibility alone is unlikely, since we controlled the ion concentrations in the recorded cone in our experiments. Finally, it is possible that the combination of these above events led to the depolarized state.

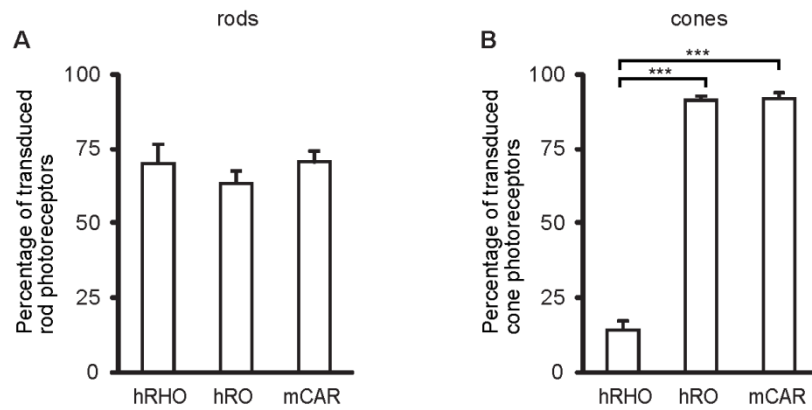
Supplementary figures



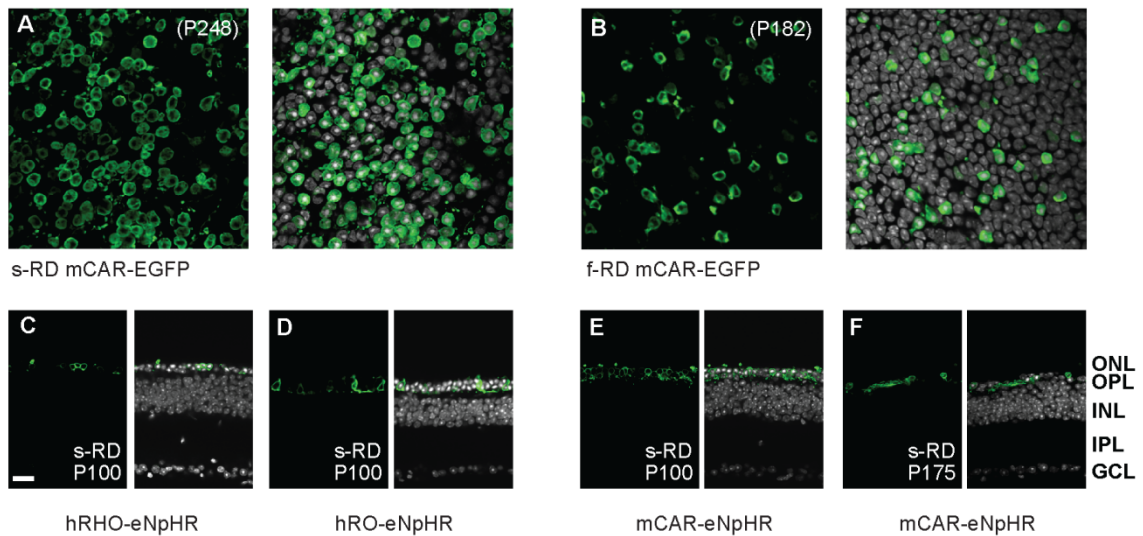
Supplementary Figure 1. (A) EGFP-expressing control AAV vectors. (B-E) Cross-sections of hRHO-EGFP- (B), hRO-EGFP- (C), mCAR-EGFP- (D) transduced s-RD and mCAR-EGFP- (E) transduced f-RD retinas. Scale bar 20 μ m.



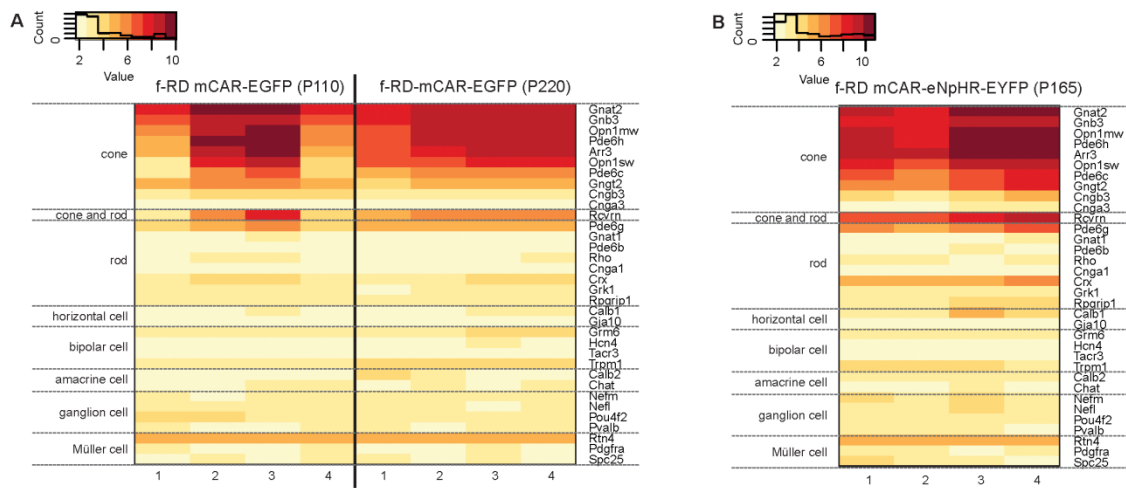
Supplementary Figure 2. Efficiency of eNpHR expression from different promoters. Confocal top views of eNpHR-EYFP expressing, GFP-immunostained photoreceptors in s-RD (A-C), f-RD (E-G) and wild-type (I-K) retinas, promoters are indicated above. Scale bar 20 μm . (D, H, L) Percentage of transduced photoreceptors with different promoter constructs. (M-O) Confocal tile scans of GFP-immunostained s-RD (M, N) and f-RD (O) retinas. Scale bar 250 μm .



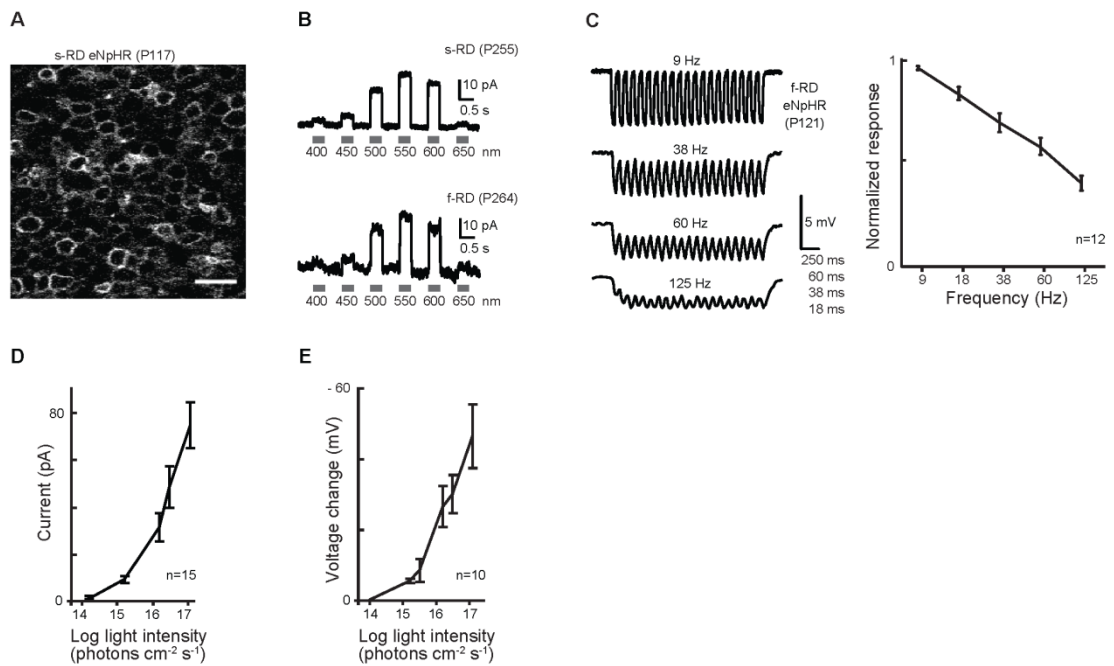
Supplementary Figure 3. The efficiency of cone photoreceptor targeting. **(A, B)** Percentage of transduced rods **(A)** and cones **(B)** by different promoter constructs quantified in wild-type retinas.



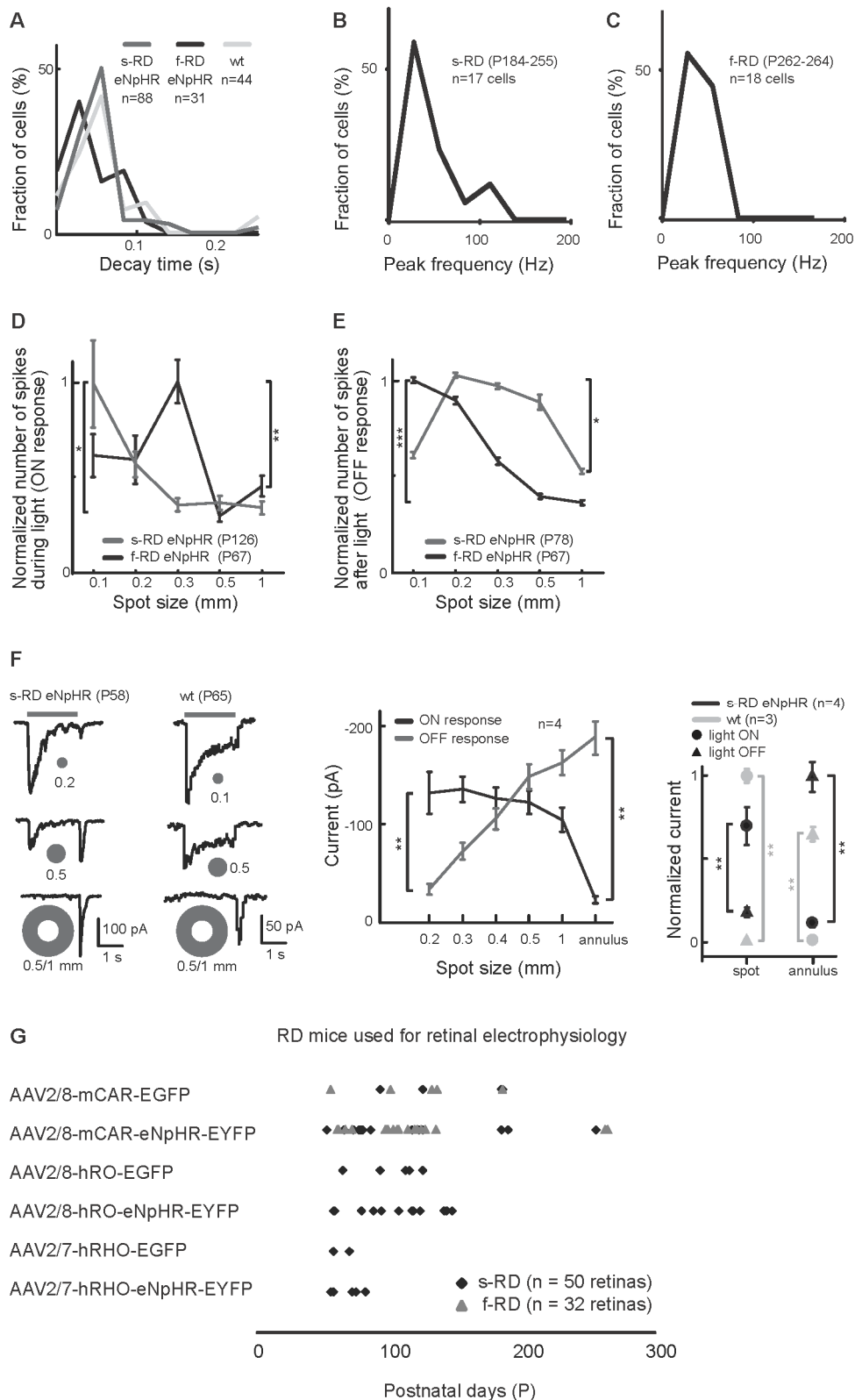
Supplementary Figure 4. Persisting eNpHR-EYFP or EGFP expression in RD retinas (P100-P248). **(A, B)** Left, confocal top view of GFP-immunostained s-RD **(A)** and f-RD **(B)** photoreceptors transduced by mCAR-EGFP. Right, co-stained with DAPI. **(C-F)** Cross-sections of GFP-immunostained s-RD retinas transduced by hRHO- **(C)**, hRO- **(D)**, and mCAR- **(E, F)** eNpHR-EYFP AAVs at P100 **(C-E)** and P175 **(F, only mCAR-eNpHR is shown)**. Scale bar 20 μ m.



Supplementary Figure 5. Analysis of the transcriptome of eNpHR-EYFP and EGFP expression cells in f-RD retinas. **(A)** Microarray analysis of EGFP-expressing and FACS-sorted f-RD photoreceptors (from P110 and P220 mice, in quadruples), heat map shows known cone markers (61) and additional retinal cell-type markers. **(B)** Microarray analysis of eNpHR-EYFP-expressing FACS-sorted f-RD photoreceptors (from P165 mice, in quadruples).

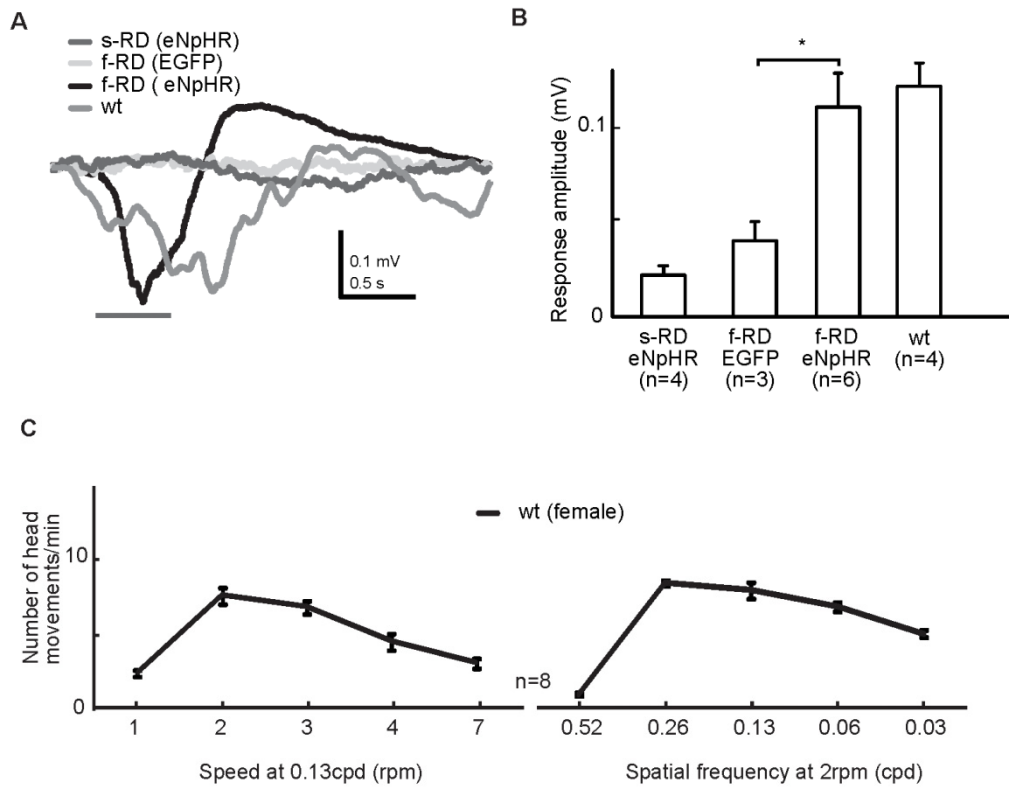


Supplementary Figure 6. Functional properties of the light responses of the eNpHR-expressing RD photoreceptors. **(A)** Two-photon laser scanning live image of photoreceptor cells expressing eNpHR-EYFP driven by the hRO promoter in an AAV-injected s-RD retina. Scale bar 10 μm . **(B)** Action spectrum of eNpHR-expressing P255 s-RD (top) and P264 f-RD (bottom) photoreceptors stimulated by full-field light flashes; gray bars indicate the timing of the stimulus. **(C)** Left, eNpHR-mediated modulation of photoreceptor membrane voltage from 9 to 125 Hz; right, normalized voltage response as a function of stimulus frequency (580 nm light). **(D, E)** Light-evoked changes of current **(D)** and membrane voltage **(E)** as a function of light intensity. “n” refers to the number of different cells we measured from.

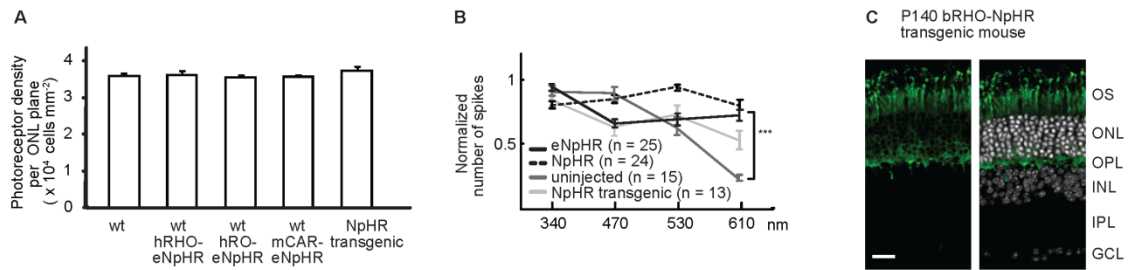


Supplementary Figure 7. The properties of light responses of ganglion cells in eNpHR-expressing RD retinas. **(A)** Both transient and more sustained ganglion cell responses can be recorded in eNpHR-transduced RD retinas. Distribution of the estimated decay time of the spike frequency response to full-field flashes in s-RD, f-RD, and wild-type (wt) retinas (difference between groups is not significant, $p=0.17$).

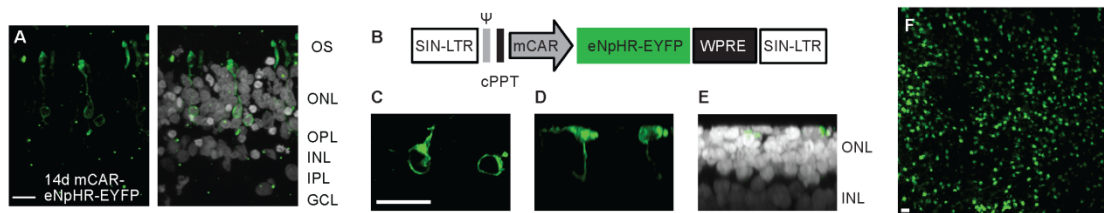
(B, C) Spiking frequency distribution in ganglion cells of eNpHR-transduced P184-255 s-RD **(B)** and P262-264 f-RD **(C)** retinas. Full-field light stimuli. **(D, E)** The effect of lateral inhibition. Examples from four ganglion cells. Number of spikes (normalized to the mean of the peak response) as a function of stimulus diameter in ON-type **(D)** and OFF-type **(E)** ganglion cells. **(F)** Left, an 'ON centre OFF surround' response in ganglion cells of an s-RD and a wild-type retina. Excitatory currents evoked by stimulation with increasing spots and an annulus. Gray bars indicate the timing of the light stimulus. Note that the receptive field center stimulation with a spot evokes an ON response and the receptive field surround stimulation evokes an OFF response. Middle, magnitude of excitatory currents for the ON-centre and OFF surround responses as a function of stimulus size in s-RD ganglion cells. Right, comparison to wild-type responses. "n" refers to the number of different cells we measured from. **(G)** Age of AAV-injected RD mice used for testing light responses. Each row represents recordings with a particular AAV type, indicated on the left. The timeline at the bottom labels the age of RD mice. Each rectangle (s-RD) or triangle (f-RD) refers to recordings on a particular postnatal day.



Supplementary Figure 8. Visually evoked potentials (VEPs) in eNpHR-expressing RD and wild-type mice (wt). **(A)** Examples of VEPs recorded in the visual cortex. **(B)** VEP response amplitudes. The intensity of light was 10^{16} photons $\text{cm}^{-2} \text{s}^{-1}$ at the eye surface **(C)** Optomotor response score of female wild-type mice (51) at different rotational speeds and spatial frequencies. “n” refers to the number of different animals we measured from.

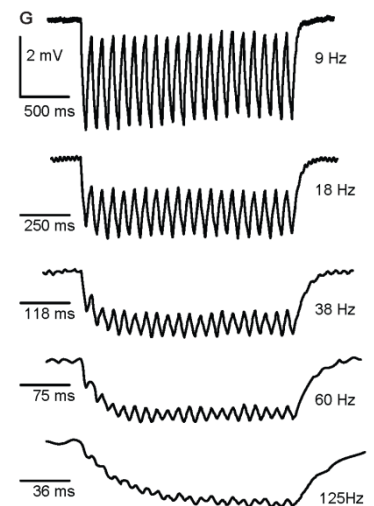


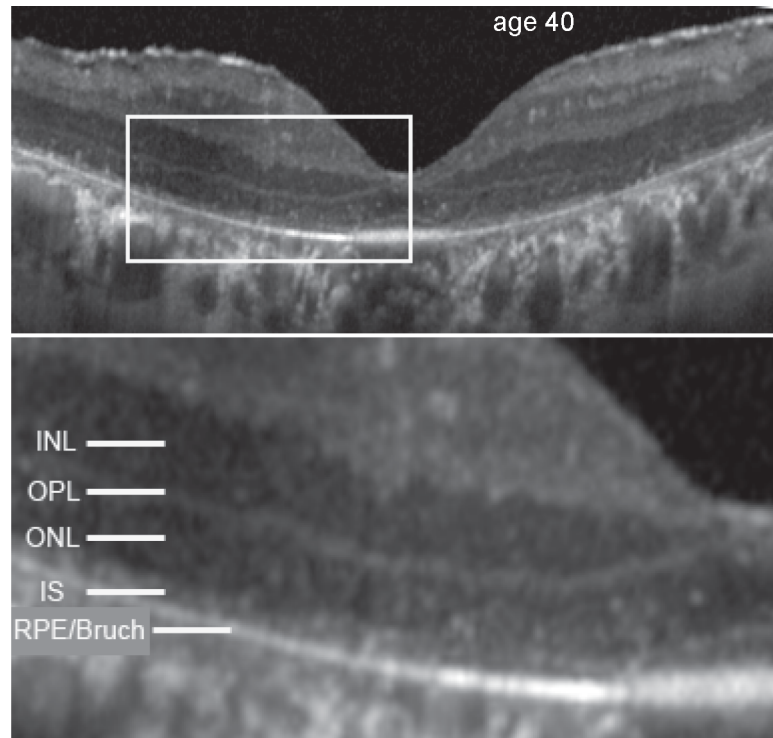
Supplementary Figure 9. eNpHR and NpHR expression is not cytotoxic to wild-type photoreceptors. **(A)** Photoreceptor density measured in confocal horizontal planes (see Materials and methods) of uninjected wild-type (wt), wild-type injected with three different eNpHR-EYFP-expressing AAVs, and bRHO-NpHR-EYFP transgenic mice. **(B)** Action spectra of AAV-transduced wild-type retinas with eNpHR (black, merged hRO and mCAR), NpHR (dashed black, hRHO), uninjected wild-type retinas (dark gray), and bRHO-NpHR-EYFP transgenic retinas (light gray) by multi-electrode array recordings. “n” refers to the number of different cells we measured from. **(C)** Cross-section of a bRHO-NpHR-EYFP transgenic mouse retina (P140). Left, EYFP signal; right, merged



with DAPI. Scale bar 20 μm .

Supplementary Figure 10. Viral targeting of photoreceptors in *ex vivo post-mortem* human retinal cultures. **(A)** Left, confocal cross-section of GFP-immunostained AAV-transduced eNpHR-EYFP-expressing human photoreceptors. Right, merged with DAPI staining (white). **(B)** Lentiviral eNpHR-EYFP expression construct: SIN-LTR, self-inactivating long tandem repeat; ψ , extended packaging signal; cPPT, central polypurine tract; WPRE, woodchuck hepatitis virus post-transcriptional regulatory element. **(C-E)** Confocal image of GFP-immunostained (green) photoreceptors. Top view (**C**), side view (**D**), and side view together with DAPI staining (white, **E**). **(F)** Confocal image (top view) of a lentivirus-transduced area of a human retina after 7 days in culture and 2 days after lentiviral administration. Scale bars 20 μm . **(G)** eNpHR-mediated modulation of human photoreceptor membrane voltage with light pulses from 9 to 125 Hz.





Supplementary Figure 11. Enlarged view of the OCT image of the patient shown in Fig. 6F. Left eye of a 40 year-old man with sporadic RP. Loss of vision since the age of 15. Visual acuity, hand motion. Flat ERG. No detectable visual field. While the ONL and inner segments (IS) are clearly delineated, there are no detectable outer segments. The retinal pigment epithelium (RPE) and the Bruch membrane are indicated.

Supplementary tables

Supplementary Table S1: Range of mice used for experiments

Experiment	s-RD	f-RD	wild-type
Imaging	P50-P255	P50-264	P64-93
Retinal electrophysiology	P53-P255	P56-264	P30-180
Cortical recordings	P70-99	P67-118	P42-60
Dark/light box test	P44-143	P50-120	P52-64
Optomotor test	P113-153	P69-120	P52-64

Supplementary Table S2: Sources of plasmids

Construct name	Source
pAAV2.1-Rho-eGFP	Alberto Auricchio
Lenti-CaMKIIa-eNpHR-EYFP-WPRE	Karl Deisseroth
pcDNA3.1/NpHR-EYFP	Karl Deisseroth
pRed2.1lacZ	Jeremy Nathans
pRho-dsRed	Constance Cepko
pRRLsincPPT-hPGK	Didier Trono

Supplementary Table S3: AAV constructs

AAV sample	Serotype	Promoter	Transgene	Titer [GC/mL]
AAV2-hRHO-EGFP	7	hRHO	EGFP	3.81×10^{12}
AAV2-hRHO-eNpHR-EYFP	7	hRHO	eNpHR-EYFP	3.28×10^{12}
AAV2-hRO-EGFP	8	hRO	EGFP	4.51×10^{13}
AAV2-hRO-eNpHR-EYFP	8	hRO	eNpHR-EYFP	3.08×10^{12}
AAV2-mCAR-EGFP	8	mCAR	EGFP	5.36×10^{13}
AAV2-mCAR-eNpHR-EYFP	8	mCAR	eNpHR-EYFP	5.33×10^{12}

Supplementary Table S4: Antibodies

Primary antibody:	Species:	Dilution:	Company:	Stock #:
anti choline acetyltransferase (ChAT)	goat	1:200	Chemicon	AB144P-200UL
anti cone arrestin	rabbit	1:200	MA Dyer, C Craft	
anti green fluorescent protein (GFP)	rabbit	1:200	Invitrogen	A 11122
anti green fluorescent protein (GFP)	sheep	1:200	Biogenesis	4745-1051
Secondary antibody:				
anti goat IgG (H+L)-Alexa Fluor 633	donkey	1:200	Invitrogen	A21082
anti rabbit IgG (H+L)-Alexa Fluor 488	donkey	1:200	Invitrogen	A21206
anti sheep IgG (H+L)-Alexa Fluor 488	donkey	1:200	Invitrogen	A11015
anti rabbit IgG (H+L)-Cy3	donkey	1:300	Jackson Labs	711-165-152

My contribution

My contribution to the following research article “Genetic reactivation of cone photoreceptors restores visual responses in Retinitis pigmentosa” published as a research article in Science was the following: I developed the underlying idea to express a hyperpolarizing light-sensitive chloride pump specifically in RD photoreceptors. I designed and tested all plasmids and AAV vectors (shown in Fig. 1 and S1). I performed all *in vivo* AAV injections in mice that were used for this study, I also transfected human retinas *in vitro* with lentiviral vectors (see Fig. 6 and S10). All immunohistochemistry, confocal microscopy, image processing and transfection quantifications (shown in Fig. 2-4, S1- S4, S9 and S10) were performed by me (except S10A). One of my images was selected as the cover image for the Juli 23rd 2010 Science issue. I recorded spikes from reactivated RD retinas using a multi-electrode array setup and analyzed these data (shown in Fig. 3 and S9). I planned and designed the plasmids to generate a transgenic mouse that was used as a control for cell toxicity of the light sensor (see Fig. S9). I performed the dark-light box behavioral assays and the optomotor response test (see Fig. 5 and S8). I dissociated GFP-labeled RD photoreceptors that were used for fluorescent-activated cell sorting following gene chip experiments (Fig. S5). I designed most experiments except two-photon targeted patch clamp recordings, cortical recordings, isolation of human post-mortem retinas, gene chip analysis and optical coherence tomography (OCT) of human eyes. I actively wrote the paper and contributed in the reviewing process.

Chapter 2 - Characterization of microRNAs induced by light adaptation in mouse retina reveals rapid turnover as a common property of neuronal microRNAs

Jacek Krol, Volker Buskamp, Ilona Markiewicz, Michael B. Stadler, Sebastian Ribi, Jens Richter, Jens Duebel, Silvia Bicker, Hans Jörg Fehling, Dirk Schübeler, Thomas G. Oertner, Gerhard Schratt, Miriam Bibel, Botond Roska and Witold Filipowicz

Published in Cell (May 14th 2010).

Summary

Adaptation to different levels of illumination is central to the function of the retina. Here we demonstrate that levels of the miR-183/96/182 cluster, miR-204, and miR-211 are regulated by different light levels in the mouse retina. Concentrations of these microRNAs were down-regulated during dark adaptation and up-regulated in light-adapted retinas, with rapid decay and increased transcription being responsible for the respective changes. We identified the voltage-dependent glutamate transporter *Slc1a1* as one of the miR-183/96/182 targets in photoreceptor cells. We found that microRNAs in retinal neurons decay much faster than microRNAs in non-neuronal cells. The high turnover is also characteristic of microRNAs in hippocampal and cortical neurons, and neurons differentiated from ES cells *in vitro*. Blocking activity reduced turnover of microRNAs in neuronal cells while stimulation with glutamate accelerated it. Our results demonstrate that microRNA metabolism in neurons is higher than in most other cells types and linked to neuronal activity.

Introduction

The first steps of vertebrate visual processing occur in the retina (62, 63). Light is converted to neural signals by photoreceptors, the more sensitive rods and the less sensitive cones, which can adapt to several log unit changes in intensity, enabling the rest of the visual system to remain responsive over an intensity span of ~8 log units. Information flows from photoreceptors to bipolar cells and then to ganglion cells, which then communicate with higher brain centers. The transfer of information from photoreceptors to bipolar cells is modified by the inhibitory horizontal cells in the outer plexiform layer (OPL), and from bipolar to ganglion cells by the inhibitory amacrine cells in the inner plexiform layer (IPL). The cell bodies of these neurons are located in distinct retinal layers: photoreceptors in the outer nuclear layer (ONL); bipolar-horizontal-amacrine cells in the inner nuclear layer (INL); and amacrine and ganglion cells in the ganglion cell layer (GCL).

Adaptation to different light levels in the retina occurs on a timescale ranging from milliseconds to hours depending on the mechanism involved. The most-studied cellular site of light-dark adaptation are the photoreceptors, where both the light-sensing (63) and adaptation machinery have been described in detail (64). In addition, different light-dark adaptation phenomena have also been noted in other cellular components of the retinal network, proximal from photoreceptors, in the INL and GCL (7). The coordination and regulation of the molecular network in different states of light-dark adaptation is not well understood. In this work, we investigated whether the process of light-dark adaptation in the mouse retina involves microRNAs (miRNAs). The layered organization of the retina and the fact that retinal cells activity can be controlled *in vivo* by light, the physiological input, make the retina a good model to study miRNAs regulation in neural circuits.

In mammals, miRNAs generally base-pair imperfectly to sequences in the 3'-untranslated region (UTR) of target mRNAs and repress protein synthesis, either by inhibiting translation of mRNAs or causing their destabilization (65) (66). miRNAs are implicated in the control of many fundamental processes and most miRNAs are expressed in a development- or tissue-specific manner (66) (67). In particular, many miRNAs are specifically expressed or enriched in neuronal cells, including those of the retina(68-71), consistent with growing evidence of importance of miRNAs for brain development and function(72, 73).

Hundreds of different miRNAs have been characterized in mammals. They are either encoded by independent genes or are excised from introns. During miRNA processing, primary transcripts (pri-miRNAs) are first cleaved in the nucleus to ~70-nt-long pre-miRNA hairpins, which are then matured in the cytoplasm to miRNAs (74). Although details of miRNA biogenesis and its regulation are quite well established, little is known about catabolism of miRNAs. They are generally assumed to have a very long half-life, corresponding to many hours or even days (75-77). However, such a slow turnover may not be a universal feature of miRNAs since they often play a role in rapid developmental transitions or act as on and off switches, conditions which call for a more active miRNA metabolism (66, 67).

We found that a subset of miRNAs is reversibly up- and down-regulated *in vivo* in the retina during light-dark adaptation, independent of the circadian rhythm. The sensory neuron-specific miR-183/96/182 cluster, and miR-204 and miR-211, are down-regulated during dark adaptation and up-regulated in light, with rapid miRNA decay and increased transcription being responsible for the changes. One of the identified targets of the light-regulated miRNAs, *Slc1a1*, might fine-tune synaptic function in different light-adaptation states. Finally, we found that fast turnover of many miRNAs is not limited to the retina but is a general property of neurons, and that activity is an important regulator of miRNA turnover in neurons.

Results

miRNAs expressed in dark- and light-adapted mouse retina

We characterized populations of small RNAs isolated from retinas of mice adapted to either light or dark (see Supplementary Experimental Procedures). To obtain a global picture of small RNAs expressed in these two conditions, cDNA libraries of gel-purified small RNAs were subjected to deep sequencing using the 454 methodology. Analysis of ~75,000 reads identified 253 retinal miRNAs expressed in either dark-adapted (DA) or light-adapted (LA) states (Figure S1A; Table S1). miRNAs, whose levels increased in LA retina included those encoded by the intergenic miR-183/96/182 cluster and intronic miRNAs miR-204 and -211 (Figure 1A, B; Table S1), identified previously as being expressed in the retina(69-71, 78). Two other platforms were also used to globally assess the effect of light on miRNA levels in the retina: Exiqon arrays and Illumina deep sequencing. A light-induced increase in the level of miR-183/96/182 cluster miRNAs was seen in two independent array experiments, while increases in miR-204/211 was only detected in one (Figure 1A; Table S1). The Illumina sequencing did not yield consistent results. In one experiment, miR-96, -204, and -211 (but not miR-182 and -183) were up-regulated 1.5- to 2.5-fold in LA retina, but in another experiment no stimulatory effect was observed (data not shown); possibly, ~2-fold effects are too small to be

reproducibly quantified by this method. To quantify miRNA levels by other, more direct techniques, the light-dependent changes in selected miRNAs were determined by quantitative real-time PCR (qRT-PCR) and RNase protection assays (RPA). These analyses demonstrated that expression levels of miRNAs encoded by the miR-183/96/182 cluster, and miR-204 and -211, increased 1.5- to 2.5-fold in LA retina (Figure 1C, D). Since a light-induced increase in the level of these miRNAs was detected by at least three independent methods, they were selected for further analysis (for comparable changes in expression of these miRNA ascertained by still another independent method, see below). It should be noted that both 454 and Exiqon I analyses identified light-dependent changes in a number of miRNAs other than miR-183/96/182, and miR-204 and -211. Since these changes were not confirmed by other analyses, these miRNAs were not further investigated. The levels of miRNAs let-7b and miR-29c (Figure 1A, C and D) did not change significantly in any analyses, and these miRNAs were therefore used as controls.

The miR-183/96/182 cluster miRNAs have related seed sequences, while the seeds of miR-204 and -211 are identical. The latter two miRNAs are excised from introns of two related protein-coding genes, *Trpm3* and *Trpm1*, which are expressed in the retina (Figure 1B; see also Figure S2B). Since the levels of miR-183/96/182 miRNAs have been reported to vary ~2-fold during the day (71), we verified that the alterations observed by us were not due to changes in gene expression associated with the circadian rhythm. For the miR-183/96/182 cluster and other miRNAs tested, increased accumulation upon light adaptation occurred independently of whether the measurements were performed at noon [Zeitgeber (ZT) 6] or at midnight (ZT18) (Figure S1B, C).

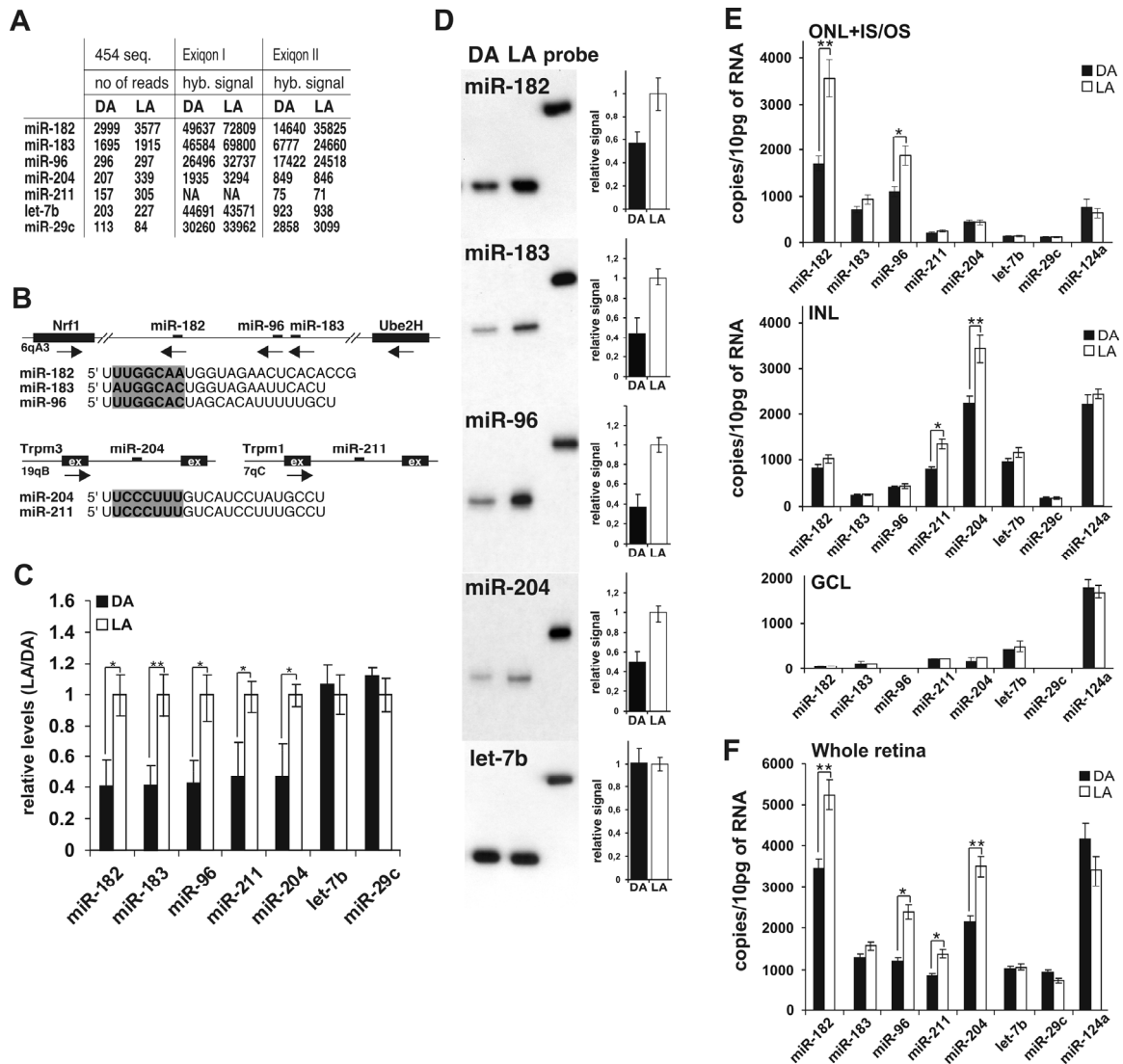


Figure 1. Differences in miRNA levels between LA and DA retinas. **(A)** Number of reads determined by 454 sequencing and Exiqon array hybridization signals (from two independent experiments) for selected miRNAs expressed in DA and LA retinas. NA, signal intensity close to background. **(B)** Schemes of genomic organization of the intergenic miR-183/96/182 cluster, and intronic miRNAs miR-204 and -211. Genes or exons flanking miRNA sequences, and chromosomal positions are indicated. Sequences of mature miRNAs are shown below, with seeds highlighted. **(C)** Comparison of miRNA levels in DA (black bars) and LA (white bars) retinas by qRT-PCR. The values, normalized for U6 RNA, are means \pm SEM [six independent experiments ($n=6$)]; * $p < 0.05$, ** $p < 0.01$. Values for LA retinas are set to one. **(D)** Quantification of selected miRNAs by RPA. The graphs show phosphorimaging quantification of miRNA levels (means \pm SEM; $n=5$). **(E and F)** miRNA levels in LCM-dissected layers of DA and LA retina **(E)** or a whole retina **(F)**. Values, normalized for U6 RNA, are means \pm SEM ($n=3$). See also Figure S1 and Table S1.

Expression of miRNAs in different retina layers

To establish expression patterns of the miRNAs investigated in different retinal cell layers we used laser capture microscopy (LCM) to dissect the LA and DA retinas. The quality of the LCM dissection was verified by demonstrating that captured samples were enriched in mRNAs known to be expressed in specific retinal cells (Figure S2C). RNA was isolated from three different layers: a layer containing photoreceptor cells (ONL+OS/IS); INL; and GCL. These were analyzed by qRT-PCR (Figure 1E), revealing that miRNAs of the miR-183/96/182 cluster were most abundant in photoreceptors, while miR-204 and -211 were enriched in the INL. The levels of miR-183/96/182 miRNAs in the ONL+OS/IS layer and miR-204 and -211 in the INL increased in response to light, consistent with the data obtained for a whole retina captured by LCM (Figure 1F). Levels of miR-183/96/182, miR-204, and -211 in the GCL were very low, although the level of a brain-specific miRNA, miR-124a, was comparable to that in other cell layers (Figure 1E).

Enrichment of the investigated miRNAs in different retinal layers was confirmed by *in situ* hybridizations (ISH) performed on sections from LA retina. In photoreceptors, strong signals were detected with probes specific for miR-182, -183, and -96, but not with the respective mutant probes (Figure S1D). Weaker signals for miR-182, -183, and -96 were also detected in the INL (71). In contrast, the INL stained strongly with probes for miR-211 and let-7b (Figure S1D). None of the used probes used detected substantial levels of miRNAs in ganglion cells, consistent with the LCM data.

Identification of potential targets of miR-183/96/182 cluster miRNAs

To gain an insight into the biological role of miRNAs undergoing light-induced changes in the retina, we compiled a list of potential targets of miRNAs from the highly expressed miR-183/96/182 cluster, using three computational target prediction algorithms: TargetScan 5.1 (www.targetscan.org); MicroCosm (www.microrna.sanger.ac.uk); and PicTar (www.pictar.mdc-berlin.de). Of the potential targets bearing miR-183/96/182 binding sites in the 3'-UTR, 337 were predicted by all three algorithms (Figure 2A). 214 of them are expressed in mouse retina (Table S2). We used RNA isolated from retina cell layers obtained

by LCM to profile mRNA expression using Affymetrix arrays. For 12 gene transcripts predicted as potential targets of miR-183/96/182 miRNAs, we observed enrichment of more than 2.0-fold ($p < 0.05$) in the ONL+OS/IS photoreceptor layer of DA retina as compared to LA retina (Figures S2A; Table S2). Among the aforementioned twelve mRNAs are those encoding a sodium/potassium-transporting ATPase subunit ATP1B3, a voltage-dependent glutamate transporter SLC1A1, and a polyA-binding protein interacting protein 2B (PAIP2B, a translational inhibitor). The expression of *Trpm1* and *Trpm3* genes, hosting miR-211 and -204 in their introns, was generally increased in a whole retina or its layers upon exposure to light, although in most instances the changes were not statistically significant (Figure S2B). This regulation is of potential interest since TRPM1 was recently implicated in the signal transduction in retinal ON bipolar cells (79, 80).

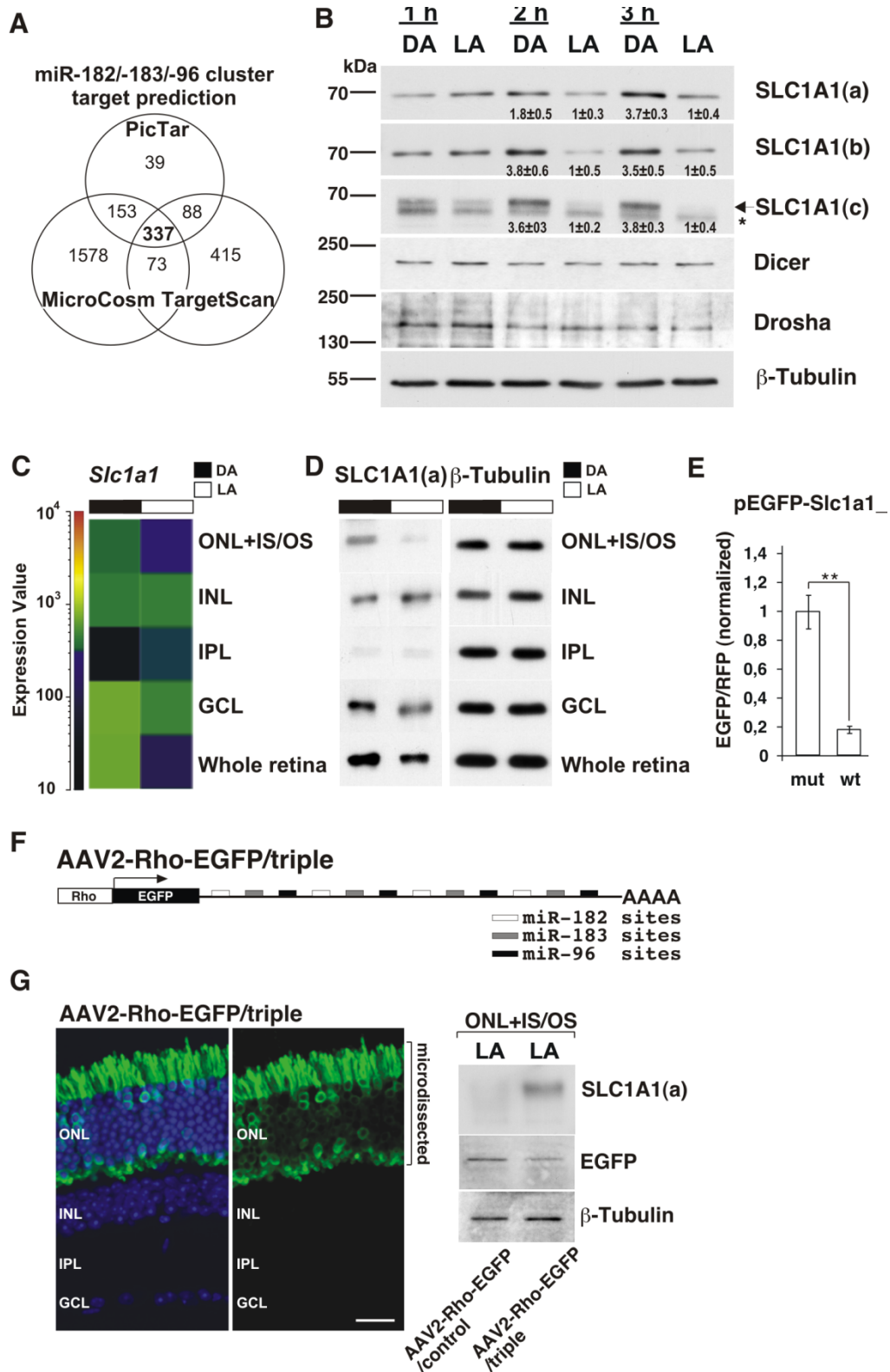


Figure 2. Glutamate transporter *Slc1a1* is targeted by miR-183/96/182 miRNAs. **(A)** Venn diagram showing targets of miR-183/96/182 cluster predicted by PicTar, Targetscan 5.1, and MicroCosm algorithms. **(B)** Western analysis of protein lysates of LA retinas and retinas from mice adapted to dark (DA) for 1, 2, or 3 h, using three different (a through c) anti-SLC1A1 Abs, and Abs against Dicer, Drosha, and β-Tubulin.

Asterisk, non-specific band recognized by SLC1A1(c) Ab. Increase in the intensity of SLC1A1 bands in DA retinas at 2 and 3 h of dark adaptation (always calculated relative to levels in LA retinas) is indicated. Values are means \pm SEM from three Westerns performed with each Ab. (C) The heat map comparing *Slc1a1* mRNA levels, as assessed using Affymetrix arrays and related to median expression values, in different LCM-dissected layers of DA and LA retinas. (D) Western blot analysis of lysates of different layers (~100,000 cells/layer) of DA and LA retinas, using anti-SLC1A1(a) and anti- β -Tubulin Abs. (E) Two-photon ratiometric imaging of EGFP expression from pEGFP-*Slc1a1*_wt and _mut constructs electroporated, together with a reference pDsRed plasmid to photoreceptors *in vivo*. The graphs show relative ratios of EGFP to RFP signals (measured for 20 individual cells for each combination of plasmids), with the ratio for pEGFP-*Slc1a1*_mut set to 1.0. Values are means \pm SEM. (F) Scheme of the AAV-Rho-EGFP-triple sponge, harboring four sites for each of the miR-183/96/182 miRNAs. (G) (left panel) Confocal cross section of an immunostained LA retina infected with AAV2-Rho-EGFP/triple. Left and right pictures visualize EGFP plus DAPI and EGFP alone, respectively. (right panel) Western analysis of lysates from five combined ONL+OS/IS layers of retinas infected with either AAV2-Rho-EGFP/triple or control sponge. See also Figures S2 and S3 and Table S2.

Validation of selected targets of miR-183/96/182 cluster miRNAs

The gene encoding the voltage-dependent glutamate transporter, SLC1A1, was first selected for a more detailed analysis. Glutamate transporters are responsible for scavenging glutamate from the synaptic cleft after release (81, 82). Western blot analysis performed with extracts of DA and LA retinas, and three different antibodies recognizing distinct sequences of SLC1A1, revealed that the level of the protein increased by up to 3.8-fold following 2- or 3-h adaptation to dark, an effect expected to accompany the decrease in miR183/96/182 levels in the dark. No light-dependent changes were observed in the levels of several control proteins, including Drosha and Dicer (Figure 2B). Importantly, analysis of different LCM-dissected layers revealed a marked increase in both *Slc1a1* mRNA and protein levels in the photoreceptors of DA retina (Figure 2C, D).

Different approaches were used to demonstrate that SLC1A1 is a direct target of miR-183/96/182 miRNAs. We constructed enhanced green fluorescent protein (EGFP) and firefly luciferase (FL) reporters containing either wild-type (wt) full-length *Slc1a1* 3'-UTR or the 3'-UTR bearing mutations in seed sequences of the two predicted sites recognized by miR-183/96/182 miRNAs

(Figure S3A). When transfected into mouse NIH3T3 cells, both types of wt, but not mutant, reporters were inhibited by miRNA mimics specific for individual miR-183/96/182 miRNAs, co-transfected either individually or as a mixture of all three (Figure S3B, G).

To find out if the EGFP reporter is similarly regulated in a more physiological context and in response to endogenous miRNAs, the wt (pEGFP-Slc1a1_wt) and mutant (pEGFP-Slc1a1_mut) EGFP reporters were *in vivo* electroporated into retinas of newborn mice to mostly target photoreceptors (18). The co-electroporated reporter expressing red fluorescent protein (RFP) was used as a normalization control. EGFP and RFP fluorescence in individual photoreceptor cells from electroporated retinas (>21 days post-electroporation) was measured by two-photon live microscopy. Activity of the EGFP reporter containing wt miRNA sites was found to be ~5-fold lower than that of the mutated form (Figure 2E). No significant difference was found in the levels of EGFP between LA and DA retinas electroporated with pEGFP-Slc1a1_wt (data not shown); possibly, electroporation of newborn mouse retinas affects proper light regulation of miRNA expression in photoreceptors.

To get further support for the role of the miR-183/96/182 cluster in regulating *Slc1a1* mRNA, we generated EGFP constructs expressing miR-183/96/182-specific “sponges” in their 3'-UTR (83). Three sponges, each containing eight sites complementary to one of the three miR-183/96/182 cluster miRNAs and a sponge containing four sites specific to each of the three miRNAs (triple sponge) were constructed (Figure S3C-F). When tested in mouse NIH3T3 cells, all sponges markedly relieved the repression of FL-Slc1a1_wt reporter induced by the co-transfection of either single miR-183/96/182 cluster miRNAs or a mixture of the three (Figure S3G).

We chose adeno-associated virus (AAV)-mediated gene transfer to deliver the triple sponge into photoreceptors *in vivo*. The sponge sequence was cloned into the 3' UTR of an EGFP cDNA, whose expression is driven by the human rhodopsin (Rho) promoter, yielding AAV2-Rho-EGFP/triple (Figure 2F). The untagged EGFP AAV construct, AAV2-Rho-EGFP/control, served as a control. AAV particles were administrated subretinally, the sponged AAV into one eye

and the control AAV into the contra-lateral eye of the same adult mice ($P > 42$). Infected retinas were isolated three weeks post-AAV injection and their EGFP-expressing ONL+OS/IS layers were dissected by LCM (Figure 2G). Western blot analysis revealed that infection with AAV-Rho-EGFP-triple resulted in a marked increase in the SLC1A1 protein level when compared to retinas infected with AAV-Rho-EGFP-control (Figure 2G), indicating that *Slc1a1* is a direct target of the miR-183/96/182 cluster. Of note, expression of the triple sponge had no effect on the level of targeted miRNAs (Figure S2G).

Western analysis of extracts from DA and LA retinas, and from “sponged” ONL+OS/IS layers with antibodies specific for PAIP2 and ATP1B3, two other predicted miR-183/96/182 targets (Figure S2A and D), revealed that levels of these proteins are ~2-fold higher in DA retinas and in photoreceptors cells expressing the AAV-Rho-EGFP-triple sponge (Figure S2E, F). Hence, similarly to *Slc1a1*, also *Paip2b* and *Atp1b3*, likely represent direct targets of the miR-183/96/182 cluster in photoreceptors.

Kinetics of light-dependent changes in miRNA and pri-miRNA levels

miRNAs are known to generally have a slow turnover(75-77). Our finding that the abundance of many retinal miRNAs markedly decreased following 3h in the dark (Figure 1) was therefore unexpected, and prompted us to measure the kinetics of changes in miRNA levels in response to dark and light adaptation. Following transfer of mice to the dark, levels of miR-183/96/182, and miR-204 and -211, reached their minimum after approximately 90 min. However, upon return to light following dark adaptation for 3h, the miRNAs reached maximal levels after only 30 min. No significant changes were seen in the levels of let-7b and miR-29c (Figures 3A and S4A).

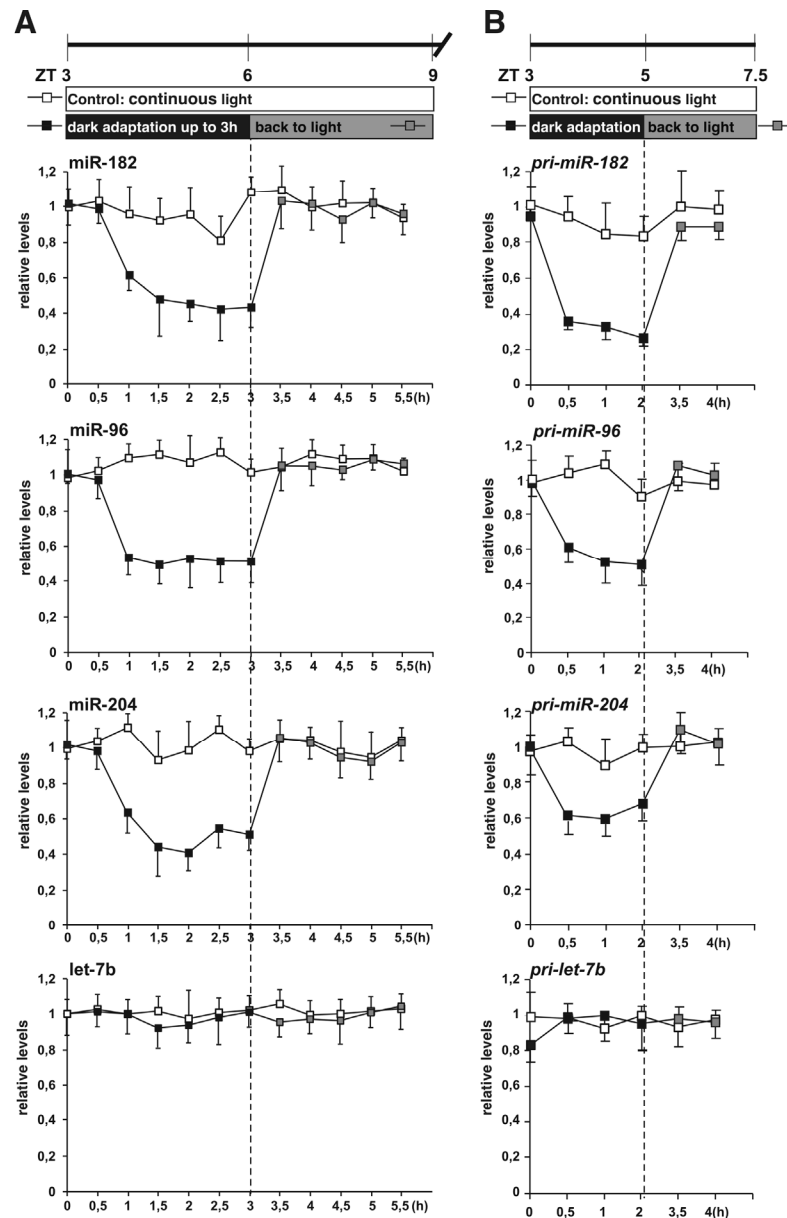


Figure 3. Kinetics of changes in mature miRNA (**A**) and pri-miRNA (**B**) levels in retina during adaptation to dark and light. Schemes at the top describe light/dark adaptation regime. Values, normalized to U6 RNA, represent means \pm SEM; $n=2$. Values for LA retinas at 0 h were set to one. See also Figure S4.

The kinetic data indicated that the more prolonged decrease in miRNA levels might be due to miRNA decay, while the rapid increase could result from augmented transcription and RNA processing. Generally (for exceptions, see (74)), processing of pri- and pre-miRNAs is quite rapid, and assessment of their levels provides an approximate measure of miRNA gene transcription. Analysis

of pri-miRNAs using qRT-PCR revealed that changes in their levels indeed occur relatively fast (≤ 30 min), irrespective of the animals being transferred from light to dark (decreased levels) or dark to light (increased levels) (Figures 3B and S4B). Similar results were obtained when combined levels of both pri- and pre-miRNAs were analyzed using RT-PCR (Figure S4C, D). Quantification of pri- and pre-miRNA suggests that changes in the level of light-induced miRNAs are a consequence of transcriptional up-regulation of their genes in response to light. These measurements, performed by procedures different from those presented in Figure 1, also provide independent evidence that the expression of the investigated miRNA genes differs between LA and DA retinas.

Inhibitor assays reveal rapid turnover of miRNAs in retina

We used specific inhibitors to directly test whether transcription is responsible for the up-regulation of precursor and mature forms of miR-183/96/182, miR-204, and miR-211. Transcription inhibitors, actinomycin D (ActD) or α -amanitin (α -Am), were injected intraocularly into the right eye, while retinas isolated from the left eye were used for control measurements (Figure 4A). The levels of pri-miRNAs and mature miRNAs were measured at time points corresponding to the established minimal (dark adaptation, 90 min) and maximal (light adaptation, 30 min) levels of miRNAs (Figure 4B). Injection of α -Am (Figures 4C-F and S5C-E, left panels) or ActD (middle panels) completely blocked the increase of pri-miRNA and miRNA levels upon exposure to light, while the expected changes occurred in the control eye. In the presence of inhibitors, the pri-miRNAs and mature miRNAs remained at the low levels characteristic of a DA retina. Notably, upon repression of transcription the levels of mature miRNAs which do not undergo light-mediated regulation (let-7b and miR-29c) and their precursors also decreased dramatically (Figure 4E, F), indicating that many, if not all, miRNAs expressed in the retina may turnover rather rapidly.

Several control experiments were performed to demonstrate that the observed effects were indeed due to the action of injected inhibitors. As expected, the inhibitors blocked expression of the pol II-transcribed *Gat1* mRNA but had no effect on expression of U6 snRNA, a stable pol III transcript (Figure S5F, G).

Moreover, injection of only a buffer to the test eye had no effect on the level of any investigated RNA (Figures 4C-F and S5C-G, right panels).

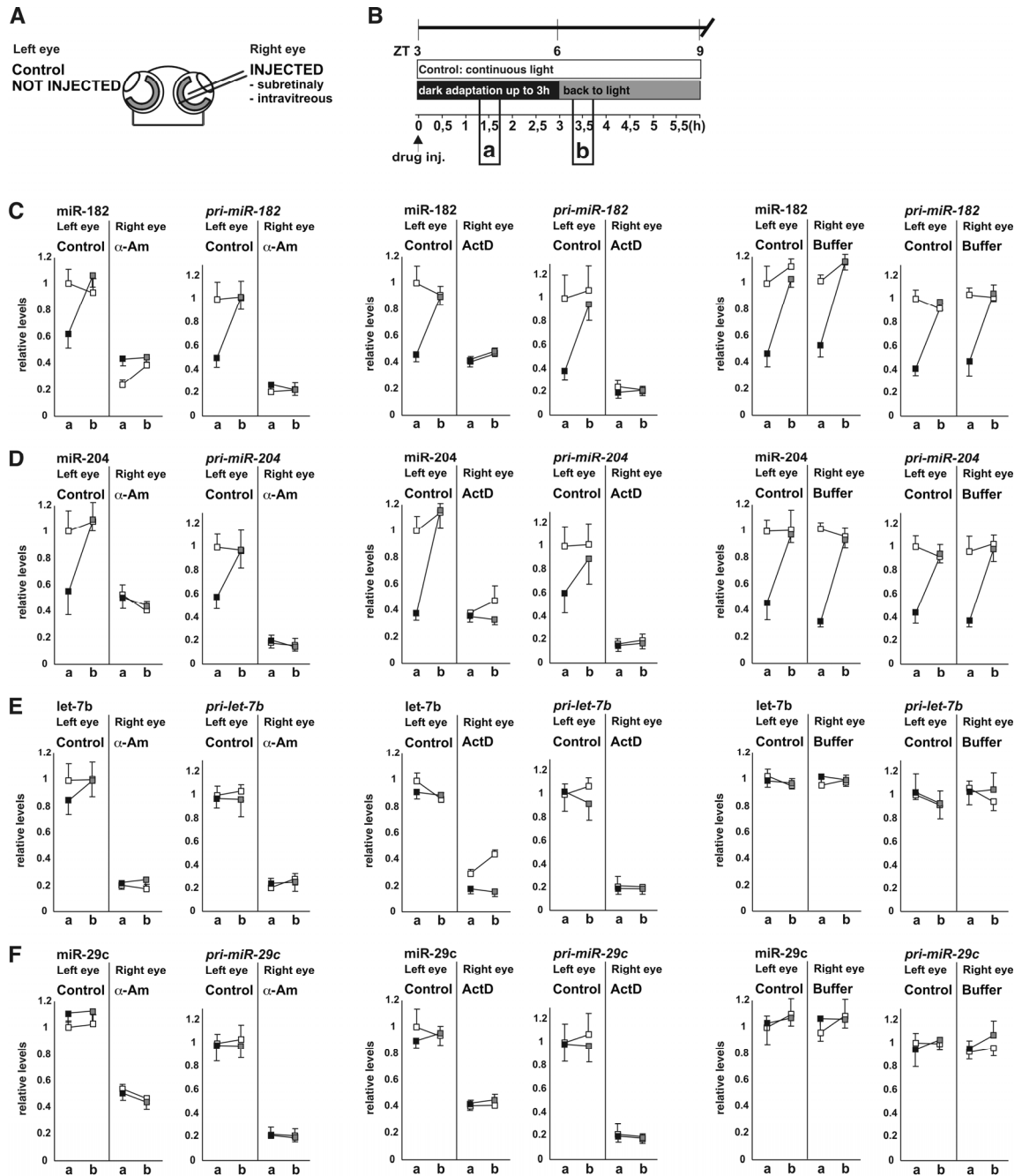


Figure 4. Effect of transcription inhibitors on miRNA and pri-miRNA levels in DA and LA retinas. **(A)** Injections were performed into right eye, and the non-injected left eye was used for isolation of control retina. **(B)** A scheme indicating time points used for collecting retinas. **(C-F)** Effect of α -Am (*left panels*) and Act D (*middle panels*) on levels of indicated miRNAs and pri-miRNAs. Control determinations, for the non-injected left eye, are in the left sub-panels. Levels of RNAs in retina from mice kept in continuous light, adapted to the dark for 90 min (a), or moved from dark to light for 30 min (b) are shown as white, black, and grey squares, respectively. Values, normalized to either U6

RNA (for α -Am and buffer injections) or 18S rRNA (for ActD injections) are means \pm SEM; n=3. Values for retinas from the control eye of mice kept in continuous light (time-point a) were set to one. See also Figure S5.

We further investigated the turnover of selected miRNAs in LCM-dissected retinal layers of wild type mouse or in specific cell types obtained by fluorescence activated cell sorting (FACS) from retinas of transgenic mice expressing EGFP or RFP under control of cell-specific promoters. As for the whole retina, inhibition of transcription resulted in a marked decrease in all tested miRNAs (including those which are not light-regulated: let-7b, miR-29c, miR-15a, and miR-16) in each dissected retina layer (Figure 5A, B). Interestingly, all miRNAs were found to turn over fast in FACS-sorted amacrine cells but not in rod bipolar cells (Figure 5C-E; see Discussion). No rapid turnover of miRNAs was observed in the FACS-sorted population of Müller glia cells (Figure 5F).

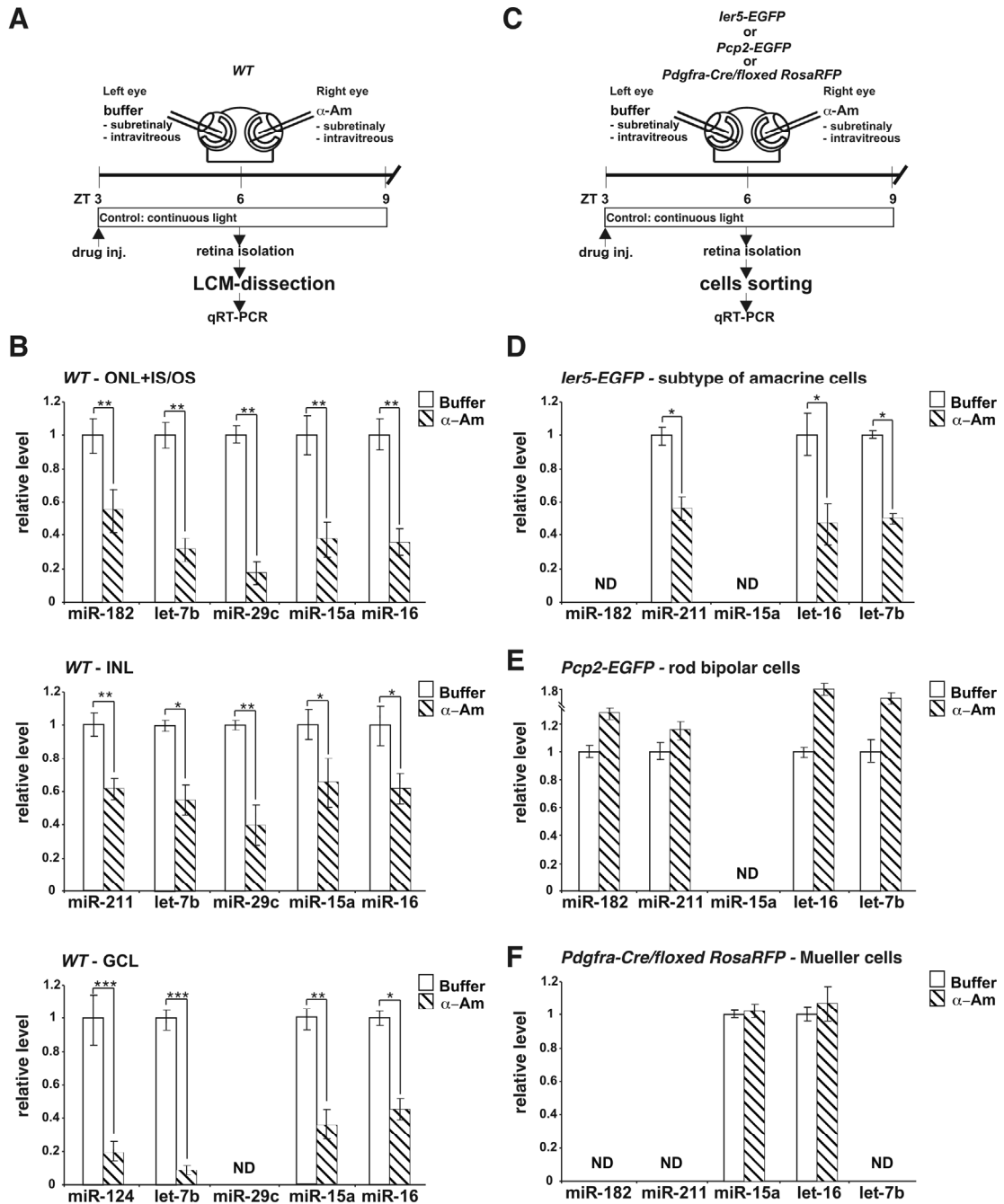


Figure 5. Determination of miRNA turnover in LCM-dissected retinal layers and FACS-sorted populations of specific retinal cells. **(A and C)** Schemes indicating experimental approaches. Mice expressing either EGFP or RFP under control of cell-specific promoters are indicated in **(C)**. Retinas were always isolated 3h after *in vivo* injection of either α -Am or a buffer. **(B)** Effect of α -Am on the level of selected miRNAs in dissected ONL+OS/IS, INL or GCL layers of LA retinas. Values represent means \pm SEM (n=2; each RNA sample assayed in triplicate). **(D-F)** miRNAs decay rapidly in amacrine cells **(D)** but not in rod bipolar **(E)** or Müller glia **(F)** cells of LA retinas. RNA was extracted from pools of FACS-sorted amacrine cells (~10,000 cells/pool; n=2), a single pool of rod bipolar cells (~10,000 cells), or pools of Müller cells (~30,000 cells/pool; n=2). Five animals were used for preparation of each pool. RNA from each

pool was tested in triplicate. Values, normalized to U6 RNA, represent means \pm SEM. Values for eyes injected with a buffer were set to one. ND, not detectable.

Taken together, these data indicate that miRNAs turnover rapidly in many types of retinal neurons, but not in rod bipolar cells or Müller glia, and that fast turnover applies to both light-responsive miRNAs and miRNAs which do not undergo light-mediated regulation.

Fast turnover of miRNAs also occurs in non-retinal neurons and is activity-dependent

The observed differences in the turnover of miRNAs between different retinal cell types and the fact that direct determination of miRNA decay was previously performed in only few studies, prompted us to measure miRNA catabolism in different cells and tissues. In all cases, the decay was determined using qRT-PCR, following treatment with either α -Am or ActD. Measurements performed with cultured NIH3T3 and RPE-1 (human retinal pigmented epithelium) cells (Figure S7A-D, left panels) and also non-differentiated mouse embryonic stem (ES) cells (see Figure 7B) revealed no appreciable turnover of investigated miRNAs for 3 or 6h following the addition of transcription inhibitors; pri-miRNAs and urokinase (uPA) mRNA decayed rapidly, as expected (Figures S7A-D, right panels; Figure S7E).

To find out whether the fast turnover of miRNAs may be a general property of neuronal cells, we first measured the decay of miRNAs in rat brain cultured hippocampal slices (84) and dissociated hippocampal neurons (85). In both systems, the addition of α -Am (Figure 6A, B; top panels) or ActD (not shown) resulted in a marked decrease in the level of neuron-specific miRNAs miR-124, -128, -134, and -138. However, levels of another neuron-enriched miRNA, miR-132, and miRNAs known to be either ubiquitously expressed or enriched in glial cells (miR-16, 23a/b, -25, -29c, -193a; (86)) were not markedly affected. Similar rapid decay of many miRNAs was also observed in mouse cultured cortical neurons (Figure 6C). We note that, in most instances, the levels of mature neuronal miRNAs decreased only ~2-fold, indicating that either only part of the cellular miRNA pool is accessible to the degradation, or that miRNAs turn over

rapidly only in a fraction of neurons (see Discussion). As expected, pri-miRNAs underwent fast degradation no matter whether they were precursors to neuronal or non-neuronal miRNAs (Figure 6A-C).

Interestingly, in all three investigated cultures the inclusion of tetrodotoxin (TTX), a toxin which blocks sodium channels and neuronal action potentials, prevented rapid turnover of miRNAs (Figure 6, panels +TTX + α -Am). Incubation with TTX in the absence of transcription inhibitors had no effect on miRNA levels (Figure 6, panels +TTX). We have verified that TTX is unlikely to affect the transcription of miRNA genes since its inclusion had no effect on pri-miRNA levels in any system (Figure S6A-C). Likewise, TTX had no apparent effect on the processing or turnover of pri-miRNAs (Figure S6A-C). These results also argue against TTX having any effect on the action of α -Am as transcription inhibitor. Analysis of hippocampal slices and dissociated neurons treated with α -Am or α -Am+TTX, by either staining with calcein AM (CalAM; staining live cells) and ethidium homodimer-1 (EthD-1; staining dead cells) or counting apoptotic nuclei, indicated that toxic effects of the inhibitors were very limited (Figure S6D, E). This argues against a possibility that the observed reductions in miRNA levels are results of selective neuronal loss upon inhibitor treatment. In summary, our data indicate that accelerated turnover of miRNAs in neurons is dependent on their activity.

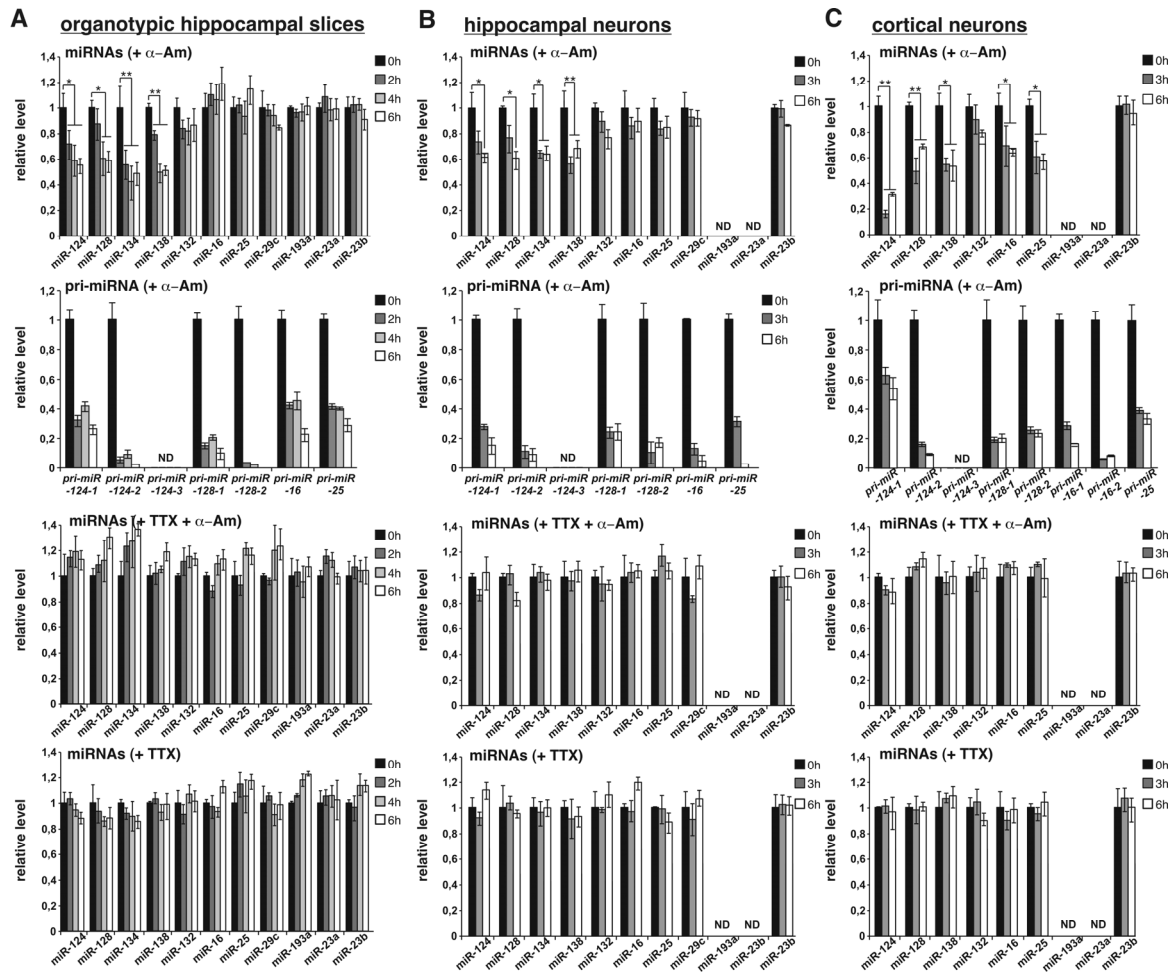


Figure 6. Activity-dependent decay of miRNAs in organotypic hippocampal slices (DIV25) (A), dissociated hippocampal neurons (DIV12) (B), and dissociated neocortical neurons (DIV25) (C). Levels of mature miRNAs (*upper and two bottom rows*) or pri-miRNAs (*second row*) were determined using RNA from cultures treated for the indicated times with α -Am or TTX alone, or a mixture of both. TTX was added to hippocampal slices and cultured neuron, 1.5 and 0.5 h prior to the addition of α -Am, respectively. Values, normalized for U6 RNA, are means \pm SEM ($n \geq 3$), with controls at 0 h set to one. Note that in cortical neuron preparations, the non-neuron specific miRNAs (miR-16 and -25) also show accelerated turnover. ND, not detectable. See also Figure S6.

Activity-dependent turnover of miRNAs in neurons derived from ES cells

To obtain additional evidence that miRNAs turn over faster in neurons than in non-neuronal cells, we used an *in vitro* system in which mouse ES cells are differentiated into a population of glutamatergic neurons. In this system, ES cells are first differentiated into neural progenitors (NPs) characterized as radial glial cells, which then give rise to differentiated pyramidal neurons (DNs; Figure

7A), know to form functional synaptic connections (87). We found that in non-differentiated ES cells (Figure 7B), NPs (not shown), and DNs maintained in culture for 15 days (Figure 7C), miRNAs did not show any appreciable turnover during the 6h following the α -Am addition (Figure 7B, C) or ActD (not shown); as expected, pri-miRNAs and uPA mRNA turned over rapidly in these cells (Figure S7E, F). In marked contrast to the 15-day culture, in neurons cultured for 25 days neuronal miRNAs miR-124, -128, -134, and -138 turned over rapidly, and their turnover was blocked by TTX; in contrast, no significant changes in the level of miR-132, and constitutive miRNAs miR-16, -23b, and -25b were seen (Figure 7D). In control experiments, we have verified that the pri-miRNA levels decreased in 25-day cultures in the presence of α -Am with similar kinetics irrespective of TTX being added to the assays (Figure S7G). Moreover, addition of α -Am and/or TTX (or glutamate and/or NBQX/ CPP; see below) did not result in a substantial cell death, particularly when cells were treated with inhibitors for 2h (Figure S7H), sufficient time to reach maximal changes in miRNA levels (Figure 7D). We also ascertained that the observed changes in miRNA levels were not due to changes in levels of Dicer or Argonaute-2 (AGO2), proteins required for miRNP assembly; treatment with α -Am or α -Am + TTX had no effect on levels or electrophoretic mobility of these proteins in 25-day ES-cell-derived or hippocampal neurons (data not shown).

The ES-cell-derived neurons express glutamate receptors and respond to glutamate stimulation (87). Thus, we tested whether glutamate has an effect on miRNA turnover in neurons cultured for 25 days. Blocking glutamate receptors with NBQX/ CPP (6-nitro-2,3-dioxo-1,4-dihydrobenzo[f]quinoxaline-7-sulfonamide, blocking AMPA and kainate receptors, plus (\pm)-3-(2-carboxypiperazin-4-yl)propyl-1-phosphonic acid, blocking NMDA receptors) prevented turnover of miR-124, -128, -134, and -138 but, surprisingly, activated decay of miR-132, which did not show any turnover in control neurons (Figure 7E). In contrast, the addition of glutamate markedly accelerated decay of miR-124, -128, -134, and -138, and also made constitutive miRNAs decay at an appreciable rate; inclusion of NBQX/ CPP blocked the effect of exogenous glutamate (Figure 7E). Notably, miR-132 again showed an opposite trend. Its degradation was accelerated on the blocking of glutamate receptors and not by

treatment with glutamate. Identical results were obtained with dissociated hippocampal neurons (Figure 7F).

We have also tested whether glutamate can induce the decay of miRNAs in ES-cell-derived neurons cultured for 15 days. The addition of glutamate, or NBQX/CPP plus glutamate, had no effect on the turnover of any miRNA (Figure 7G). To follow the electrophysiological properties of the ES-cell-derived neurons as a function of time in culture, we cultured them on microelectrode arrays (MEAs) and recorded their spontaneous spiking activity. Although some spiking was already visible after 10 to 15 days, maximal activity was reached after 25-30 days of culturing (Figure S7I).

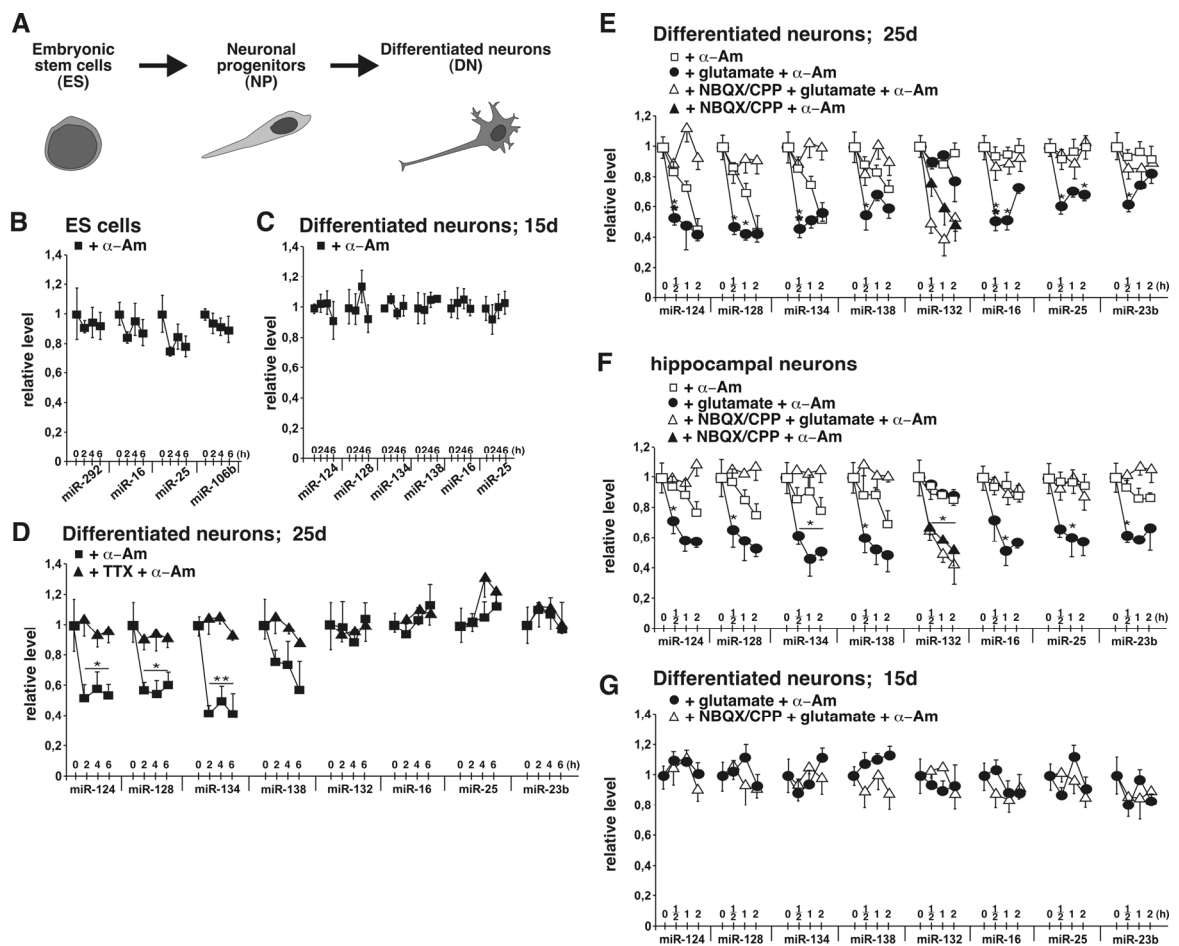


Figure 7. Analysis of turnover of miRNAs in mouse ES cells and neurons derived from them. **(A)** Scheme of the *in vitro* differentiation of mouse ES cells into neuronal progenitors (NP) and neurons (DN). **(B-D)** Effect of α -Am or TTX + α -Am on the level of indicated miRNAs in ES cells or neurons maintained in culture for 15 or 25 days. **(E-G)** Effect of α -Am, glutamate + α -Am, or NBQX/CPP + glutamate + α -Am on the level of miRNAs in ES-cell-derived neurons (**E**, **G**) and hippocampal neurons (**F**). For cultures

treated with NBQX/ CPP and α -Am (black triangles), only miR-132 level measurements are shown in panels E and F. Levels of other miRNAs were not affected by this treatment (not shown). Glutamate and/or NBQX/ CPP were added to cultures 15 min prior to the addition of α -Am. Following α -Am addition, cultures were collected at indicated times (0-6h for panels B-D; 0-2h for panels E-G). Values, normalized for U6 RNA, are means \pm SEM (n=4). See also Figure S7.

In summary, these experiments indicate that in both ES-cell-derived and hippocampal neurons neuronal activity may have both stimulatory and inhibitory effects on miRNA turnover. Experiments with differentiated ES cells also suggest that neurons have to reach a certain level of maturity or connectivity to manifest activity-dependent changes in miRNA decay.

Discussion

In this work, we identified miRNAs which respond to different light conditions in mouse retinal neurons, independent of the circadian clock. Levels of the sensory neuron-specific miR-183/96/182 cluster, and miR-204 and -211, were down-regulated during dark adaptation and up-regulated during light adaptation, with rapid miRNA decay and increased transcription being responsible for the respective changes. We identified the voltage-dependent glutamate transporter, *Slc1a1*, as one of the targets of the light-regulated miR-183/96/182 cluster; other likely targets of these miRNAs in photoreceptor cells include *Paip2b* and *Atp1b3*. We found that many miRNAs in retinal, and also non-retinal, neurons turn over much faster than miRNAs in other cell types. Blocking action potentials with TTX, or glutamate receptors with NBQX/ CPP, strongly affected miRNA turnover rates, indicating that active miRNA metabolism may be important for the function of neurons.

Different algorithms were previously used to predict targets of miRNAs expressed in the retina, and, in a few instances, the validity of the predictions was tested using 3'-UTR reporter fusions in HEK293 or NIH3T3 cells overexpressing retinal miRNA mimics (68, 71). Using three different algorithms, we compiled a list of potential miR183/96/182 targets, including 214 mRNAs expressed in the mouse retina. Levels of 12 of them were up by more than 2-

fold ($p < 0.05$) in the photoreceptor layer of the DA retina as compared to the LA retina, consistent with the decrease in miR-183/96/182 miRNAs in the dark.

For mRNA encoding SLC1A1, we obtained compelling evidence that it is a *bona fide* target of miR-183/96/182 miRNAs. In addition to the support obtained from reporter assays, performed *in vitro* and *in vivo*, we found that: (1) the AAV-mediated expression of “sponges”, which titrate miR-183/96/182 miRNAs in photoreceptors *in vivo*, resulted in a marked increase in the SLC1A1 level in the LCM-dissected photoreceptor layer; and, (2) in the western blot analyses, the level of SLC1A1 increased 2- to 3-fold during dark adaptation, an effect expected to accompany the decrease in miR183/96/182 in the dark. Experiments listed in (1) and (2), indicated that also *Paip2b* and *Atp1b3* are likely to represent miR183/96/182 targets. To our knowledge, *Slc1a1*, *Paip2b*, and *Atp1b3* represent the first examples of miRNA-regulated mRNAs documented in the physiological context of the retina.

The finding that *Slc1a1*, which encodes a neuronal glutamate transporter, is a target of the miR-183/96/182 cluster, and that its level increases in the dark, is intriguing. Glutamate is the neurotransmitter used by vertebrate photoreceptors (88). In the dark, photoreceptors are depolarized and release glutamate. Light hyperpolarizes the membrane and the release of glutamate is reduced. It has been shown that glutamate transporters help to clear glutamate from the synaptic cleft in rods and cones (89, 90). In the DA state, the load on rod glutamate transporters is higher than in the LA state, when rods are saturated by light, and therefore the up-regulation of glutamate transporters in the dark may help to scavenge glutamate from the synaptic cleft. In LA retinas, when SLC1A1 expression is low (Figure 2B, D), it has been suggested (90) that the glutamate transporter in rods is SLC1A7. However, immunohistochemical evidence shows that SLC1A1 is also present in rods (91). We propose that SLC1A1 in the dark helps SLC1A7 to remove glutamate from the first visual synapse.

Kinetic experiments and the use of transcription inhibitors have revealed that all tested miRNAs, both light-regulated and constitutively expressed, decay in retinal neurons very rapidly ($T_{1/2}$ of 1h or less). This contrasts with the situation

in purified Müller glia and rod bipolar cells, in which no decrease in the level of miRNAs was observed during 3h of α -Am treatment. Inhibitor experiments also indicated that fast up-regulation of miR-183/96/182, miR-204 and -211 levels upon exposure to light is due to increased transcription of the respective genes. It is important to emphasize that, while turnover experiments with non-retinal neurons involved the use of α -Am or ActD, the rapid decay of miRNAs in the retina *in vivo* was observed upon transfer of animals from light to dark, thus under physiological conditions, in the absence of the inhibitors.

Rapid decay of many miRNAs was also observed in cultured rodent neurons or hippocampal slices, and in neurons differentiated from mouse ES cells *in vitro*. In all these systems, the addition of α -Am or ActD resulted in a rapid decrease in the level of neuron-specific miRNAs such as miR-124, -128, -134, and -138. In contrast, we observed no appreciable decay of miRNAs over 6h in cultured NIH3T3, RPE-1 or ES cells. Experiments with neurons indicated that miRNA turnover may be subject to complex activity-dependent regulation. In all four neuronal cultures investigated, blocking action potentials with TTX prevented rapid turnover of miRNAs. Blocking glutamate receptors with NBQX/CPG likewise prevented turnover of miR-124, -128, -134, and -138 in hippocampal and ES-cell-derived neurons, while the addition of glutamate accelerated it. Notably, the behaviour of miR-132 was opposite to the other miRNAs. Its degradation was induced by the blocking of glutamate receptors and not by the addition of glutamate. miR-132 represents one of the most studied neuronal miRNAs. Its transcription is up-regulated by light and it modulates the expression of clock genes in the superchiasmatic nucleus in mice (92). Importantly, the expression of miR-132 is activated in response to neuronal stimulation in rodent brain or culture neurons (93), and miR-132 is required for activity-dependent dendritic growth and spine formation (93, 94). These findings, clearly distinguishing the activity of miR-132 from that of miRNAs such as miR-134 or -138, which generally reduce dendritic spine growth (reviewed by (73)), provide a possible rationale explaining why miR-132, in contrast to miR-134 or -138, is not a subject of the accelerated decay in active neurons.

The dependence of miRNA decay on neuronal activity may also explain why miRNAs were found to turn over fast in FACS-sorted amacrine cells but not rod

bipolar cells. Rod bipolar cells are thought to be inactive during daylight conditions, while amacrine cells are activated during both dark and light states (62). Since both types of cells were collected during daylight, it is likely that rod bipolar cells were less, or not at all, active. The observation that miRNAs decay fast in ES-cell-derived neurons cultured for 25 but not 15 days is also consistent with the idea that a defined level of neuronal maturation or connectivity is essential for increased catabolism of miRNAs. The MEA recordings showed that spontaneous spiking activity of 25-day neurons is substantially higher than that of 15-day neurons. In addition, we found that neither NBQX/CPG nor glutamate had any effect on miRNA decay in 15-day cultures.

It was reported recently (95) that levels of two miRNAs, miR-124 and -184, are down-regulated 2 to 3-fold in *Aplysia* neurons upon stimulation with serotonin, although no inhibitor studies were performed to determine the mechanism involved. In another recent report, they (96) found that brain-enriched miRNAs in human primary neural cultured cells and post-mortem brain tissues have a $T_{1/2}$ of 1-3.5h. Hence, rapid and/or activity-regulated miRNA decay may be a general feature of neurons. This contrasts with the situation in non-neuronal cells in which miRNAs generally turn over very slowly (75, 77) (this work), with estimated half-lives extending even beyond 24h (76).

What could be a role of accelerated turnover of miRNAs in neurons, and why would turnover be dependent on neuronal activity? Several hundred protein-coding genes have been identified in cortical and hippocampal neurons whose transcription is regulated by neuronal activity. Many of them encode transcription factors while others specify proteins with important functions in dendrites and synapses (reviewed by (97)). Possibly, the rapid turnover of miRNAs and, consequently, a continuous supply of *de novo*-transcribed miRNAs, are prerequisites for the assembly of new miRNPs, which would be available for regulating the newly-synthesized activity-dependent mRNA targets. Such regulation might involve not only translation or stability of the targeted mRNAs, but also their localization and expression in neuronal processes (73). Blocking neuronal activity would make the need for rapid miRNA metabolism obsolete because of the diminished supply of potential mRNA targets. In another scenario, the fast decay of miRNAs might be important for stimulating

translation of neuronal mRNAs, e.g. those located at dendritic spines, in response to synaptic activity (reviewed by (72, 73)).

In the future, it will be important to establish what factors are responsible for the rapid decay of miRNAs and its regulation in neurons. Enzymes responsible for miRNA turnover are beginning to be identified (98, 99). In addition, the first examples of regulated miRNA turnover, such as differences in the miR-29b half-life between cycling and mitotic HeLa cells (77), or the stabilizing effect of the A residue addition to the 3'end of miR-122 in liver (100), have already been reported.

Supplemental data

Supplemental Data include Supplemental Experimental Procedures, Supplemental References, seven figures, and three tables.

Supplemental figures

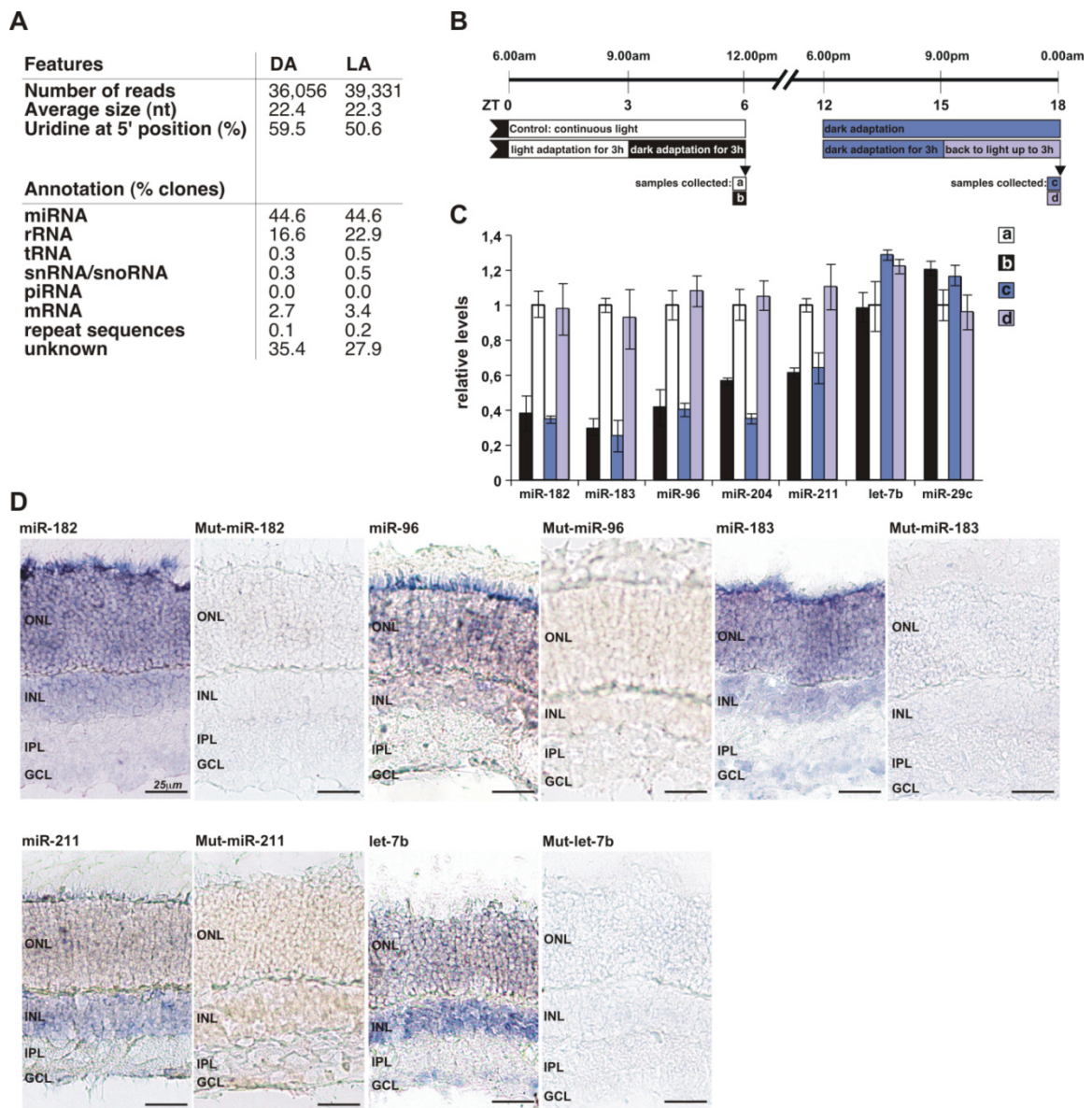


Figure S1, related to Figure 1. Analysis of light dependent changes and localization of miRNAs expression in retina. **(A)** Summary of 454 deep sequencing data of small RNAs isolated from LA and DA retinas. **(B)** Schemes describing the light/dark adaptation regime at different times of the day. **(C)** Light dependent changes in the level of retinal miRNAs are not due to circadian regulation. Comparison of miRNA levels in DA and LA retinas collected at different times of the day. Values, normalized to U6 RNA, are means \pm SEM from qRT-PCR reactions performed in triplicate with RNA isolated from pooled retinas of four animals. Values for LA retinas collected at ZT6 are set to one. **(D)** Localization of miRNAs in LA retina determined by *in situ* hybridization. Cryosections were hybridized with perfectly complementary or mutated digoxigenin-labeled LNA probes. Blue staining indicates a positive hybridization signal.

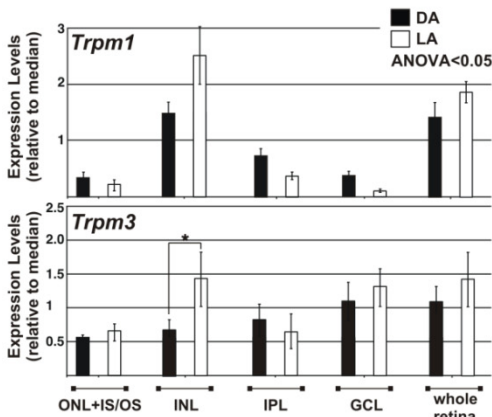
ONL, outer nuclear layer; INL, inner nuclear layer; IPL, inner plexiform layer; GCL, ganglion cell layer.

A

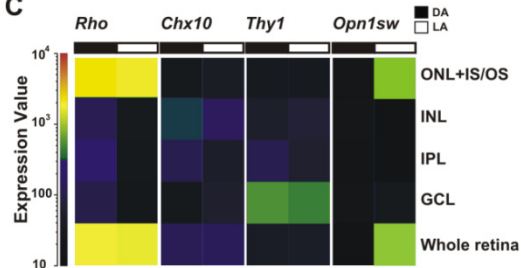
List of miR-182/183/96 target candidates expressed in ONL+IS/OS >2.0-fold up-regulated in DA relative to LA retina

Gene symbol	Description	Fold
<i>Paip2B</i>	polyadenylate-binding protein-interacting protein 2B	4.7
<i>Sfrs2</i>	splicing factor, arginine/serine-rich 2	4.1
<i>Zhx2</i>	zinc fingers and homeoboxes protein 2	4.1
<i>Atp1b3</i>	Sodium/potassium-transporting ATPase subunit beta-3 (ATPB-3)	3.7
<i>Nlgn2</i>	neuroligin 2	3.6
<i>Tpm1</i>	tropomyosin 1, alpha	3.5
<i>Anxa11</i>	annexin A11	3.2
<i>Gng5</i>	guanine nucleotide binding protein (G protein), gamma 5 subunit	3.2
<i>Slc1a1</i>	excitatory amino acid transporter 3	3.05
<i>Chst10</i>	carbohydrate sulfotransferase 10	2.82
<i>Pcdh8</i>	protocadherin 8	2.1
<i>KcnJ14</i>	potassium inwardly-rectifying channel, subfamily J, member 14	2.0

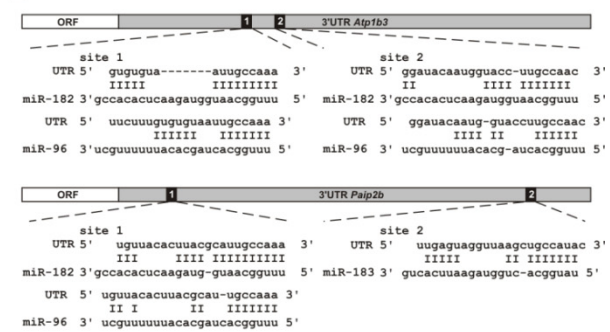
B



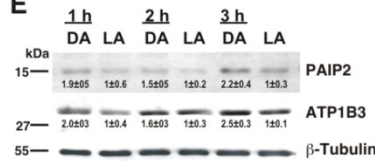
C



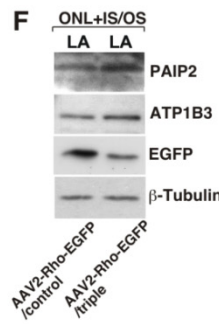
D



E



F



G

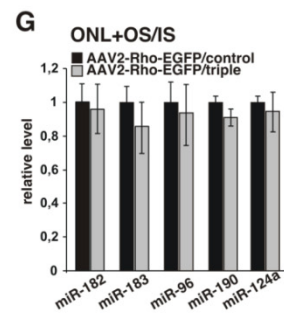


Figure S2, relative to Figure 2. Analysis of miR-183/96/182 targets in LA and DA retinas. **(A)** List of putative miR-183/96/182 targets up-regulated ≥ 2 -fold ($p < 0.05$) in retinal photoreceptors of DA relative to LA retina. **(B)** Comparison of expression of *Trmp1* and *Trpm3* genes, which host intronic miR-211 and miR-204 (both up-regulated by light), respectively. Values for different cell layers dissected from LA or DA retinas represent means \pm SEM of transcript levels, relative to the median (data collected from two independent array experiments). ONL+OS/IS, photoreceptors; INL, inner nuclear layer; IPN, inner plexiform layer; GCL, ganglion cell layer. **(C)** Quality of LCM dissection verified by demonstration that mRNAs known to be expressed in specific retinal cells are enriched in LCM-captured samples of DA or LA retinas. The heat map displays

expression of rhodopsin (*Rho*), *C. elegans* ceh-10 homeodomain-containing homolog (*Chx10*), and Thy-1 membrane glycoprotein precursor (*Thy1*) genes, which represent markers for photoreceptors, bipolar cells and ganglion cells, respectively(19, 101-104). The *Opn1sw* gene represents a light/dark adaptation marker (105). Numerical values represented by different colors are indicated by the bar scale on the left. **(D)** Sequences and base-pairing of predicted sites in 3'UTRs of *Atp1b3* and *Paip2b* mRNAs, potentially recognized by individual miR-183/96/182 cluster miRNAs. **(E)** Western blot analysis of protein lysates of LA retinas and retinas from mice adapted to dark (DA) for the indicated times, using Abs against PAIP2, ATP1B3, and β -Tubulin. Increase in the intensity of specific bands in DA retinas (always calculated relative to levels in LA retinas) is indicated. Values are means \pm SEM (n=3). **(F)** Western blot analysis of lysates from five combined LCM-dissected ONL+OS/IS layers of retinas infected with either AAV2-Rho-EGFP/triple or control sponge. **(G)** Levels of endogenous or transfected miR-183/96/182 cluster miRNAs are not affected by expression of the triple sponge construct. RT-qPCR analysis of endogenous miRNA levels in the LCM-dissected ONL+OS/IS layer of retinas infected with either AAV2-RHO-EGFP/triple or AAV2-RHO-EGFP/control. Values, normalized to U6 RNA, represent means \pm SEM. Values for samples infected with AAV2-RHO-EGFP/control were set to one.

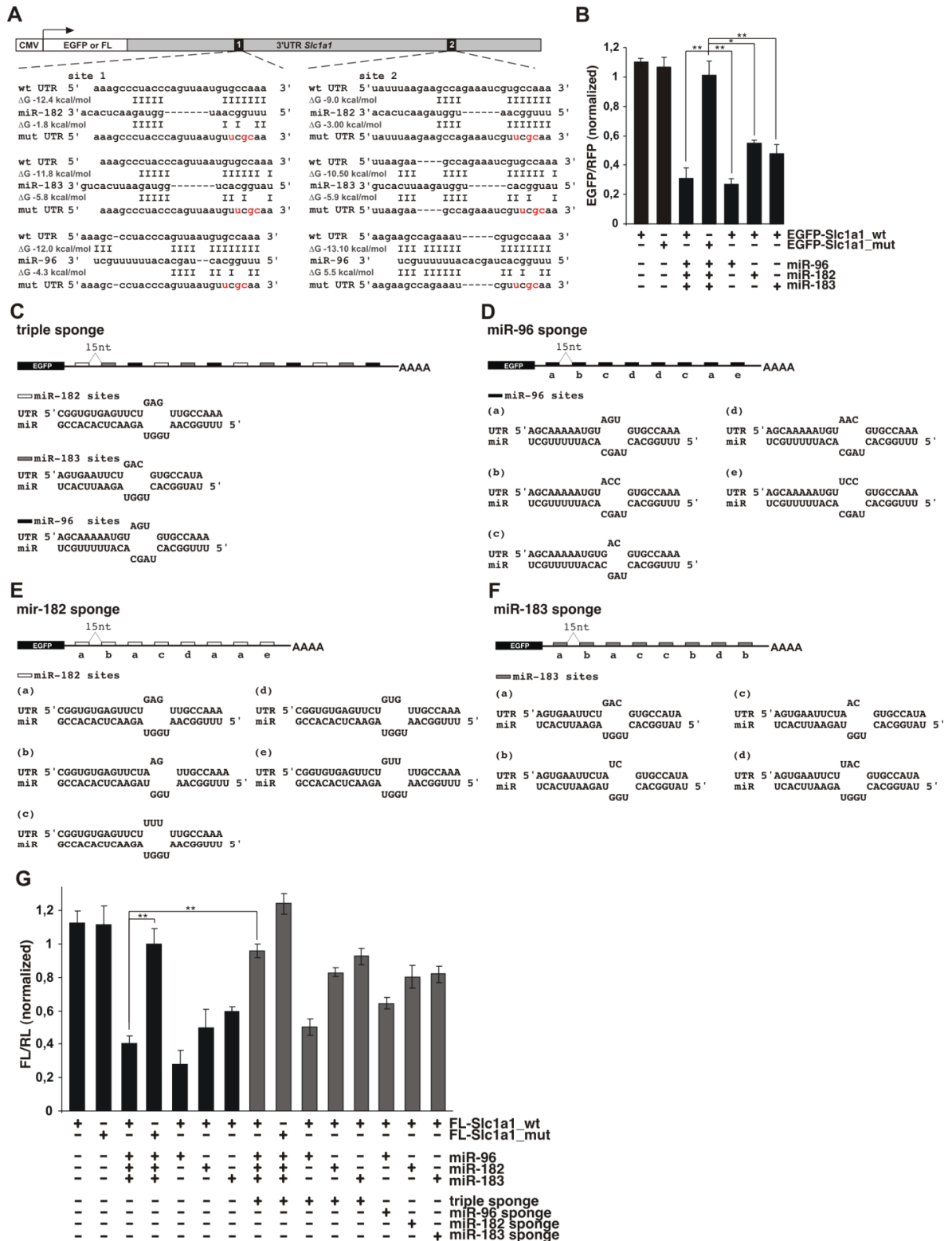


Figure S3, related to Figure 2. The EGFP-Slc1a1_wt reporter is specifically repressed by miR-183/96/182 cluster miRNAs in transfected mouse NIH3T3 cells. **(A)** Schematic representation of EGFP and FL reporter constructs harboring either wt or mut forms of the *Slc1a1* 3'UTR. Sequences of predicted sites (wt and mutant forms, with mutated residues in the seed regions shown in red) recognized by individual miR-183/96/182 cluster miRNAs are shown below. Base-pairing to miR-182, miR-183 and miR-96, and

stability of miRNA/mRNA pairings calculated as ΔG using mfold v. 3.2 are also indicated. **(B)** Activity of EGFP-Slc1a1_wt and EGFP-Slc1a1_mut reporters in NIH3T3 cells cotransfected with control pDsRed plasmid and indicated miRNA mimics. Expression of EGFP and RFP was analyzed by FACS, 48 h post-transfection. Values, normalized for expression of RFP, are means \pm SEM (n=3); *p < 0.05, **p < 0.01. Expression value for EGFP-Slc1a1_mut co-transfected with a mixture of three miRNA mimics was set to one. **(C-G)** Anti-miR-183/96/182 sponges rescue repression of FL-Slc1a1_wt reporter by miR-183/96/182 cluster miRNAs in transfected NIH3T3 cells. Schematic representation of sponge constructs harboring either a mixture of sites for all three miR-183/96/182 cluster miRNAs **(C)** or sites specific for individual miRNAs: miR-96 **(D)**, miR-182 **(E)**, and miR-183 **(F)**. Sequences of different variants of the designed miRNA target sites and their pairing to individual miRNAs are shown below each scheme. **(G)** Activity of FL-Slc1a1_wt and FL-Slc1a1_mut reporters in NIH3T3 cells cotransfected with control pRL reporter and indicated sponges and miRNA mimics. Expression of luciferases was measured 48 h post-transfection. Values, normalized for expression of RL, are means \pm SEM (n=3). Expression value for FL-Slc1a1_mut co-transfected with a mixture of three miRNA mimics and no sponge was set to one. Black bars, transfections containing no sponge plasmids; grey bars, transfections containing sponge plasmids.

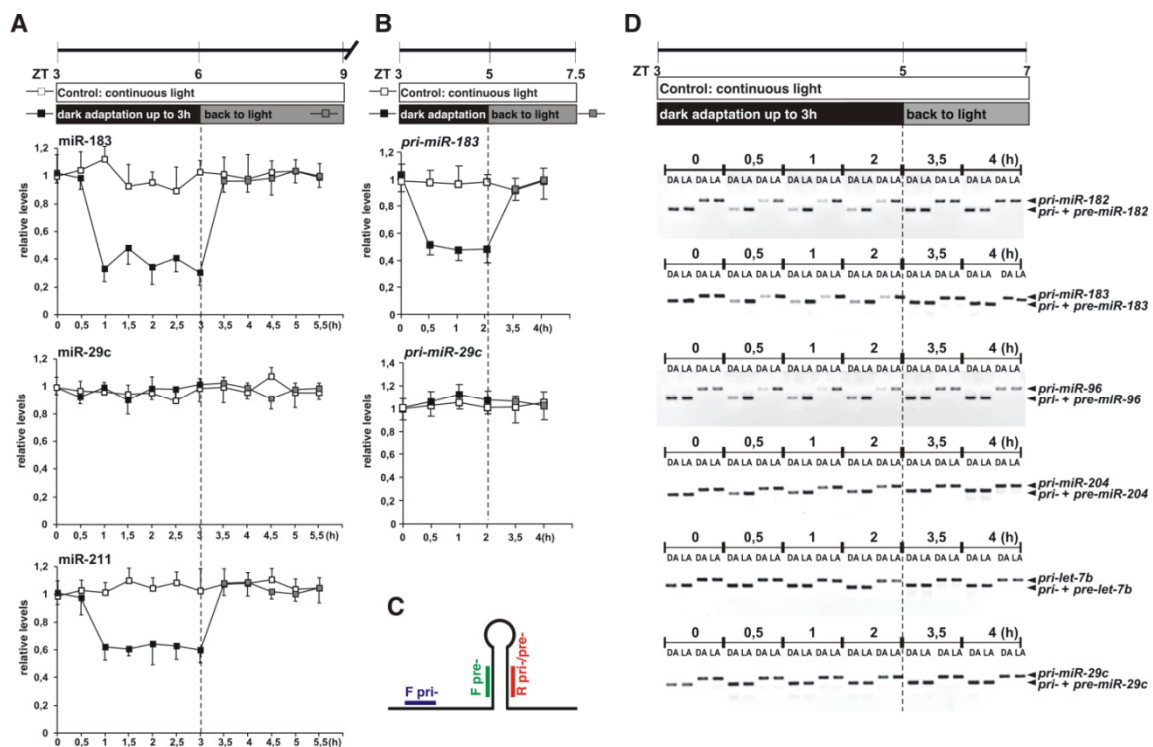


Figure S4, related to Figure 3. Kinetics of changes in mature miRNA and pri/pre-miRNA levels in retina during adaptation to dark and light. Changes in mature **(A)** and pri-miRNA **(B)** levels during adaptation to dark and light. Schemes at the top describe light/dark adaptation regime. Values, normalized to U6 RNA, represent means \pm SEM (n = 2). Values for LA retinas at 0 h (ZT3) were set to one. **(C)** A scheme explaining

amplification of pri- and pre-miRNAs. Hybridization positions of the pre-miRNA forward (F; green) and reverse (R; red) primers are indicated. To amplify specifically pri-miRNAs, a forward primer (F; blue) was used along with the reverse (red) pre-miRNA primer. (D) Changes in pri- and pre-miRNA levels during adaptation to dark and light. Following PCR, a portion of each reaction was run on a 2.5% agarose gel. Positions of amplification products specific for either pri-miRNA or a sum of pri- and pre-miRNA, are indicated.

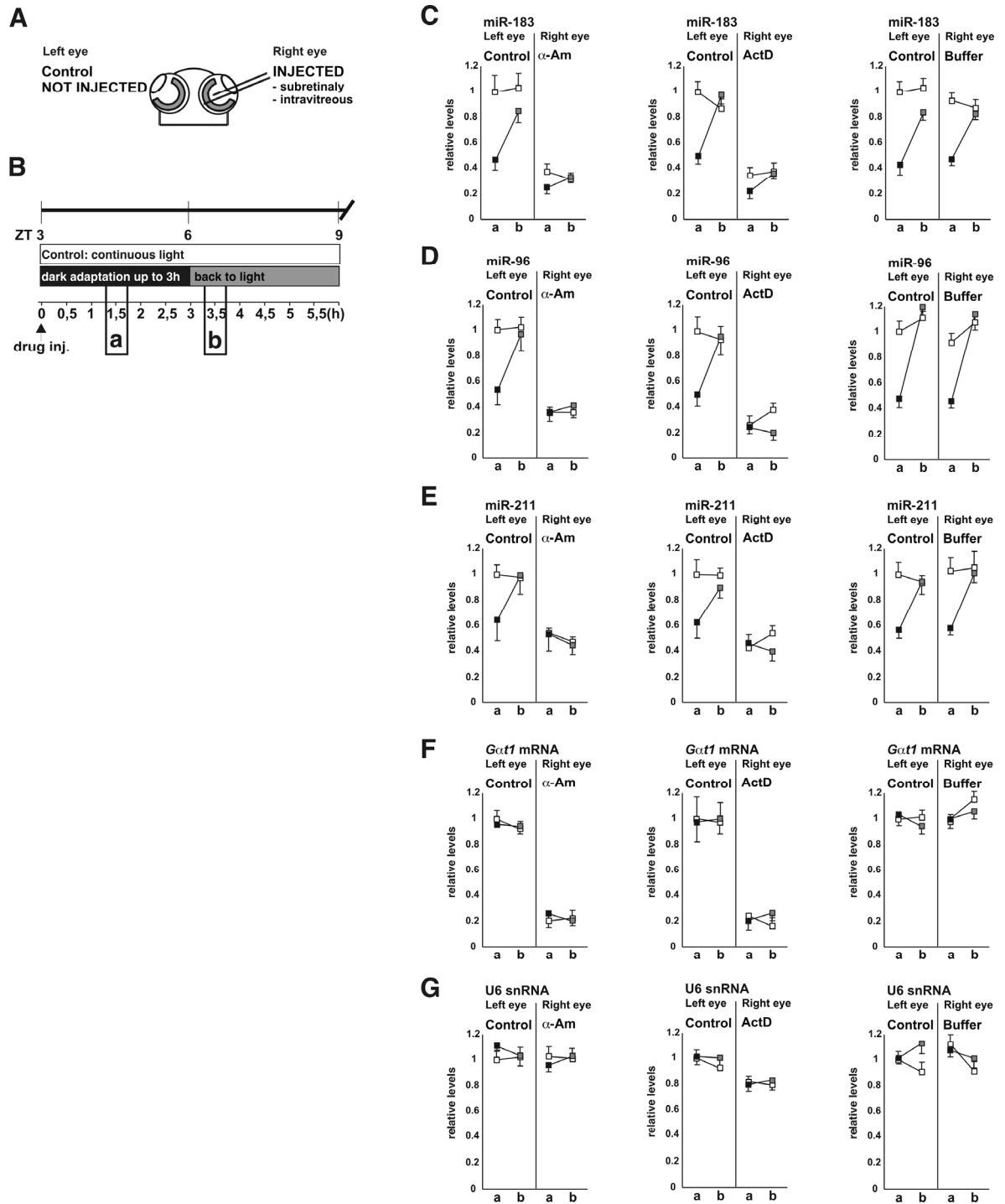


Figure S5, related to Figure 4. Effect of transcription inhibitors on the levels of miRNAs, *Gat1* mRNA, and U6 RNA in DA and LA retinas. **(A)** A scheme indicating an experimental approach. Injections were performed into right eye and non-injected left eye was always used for isolation of control retina. **(B)** A scheme indicating the dark/light adaptation regime and time-points used for collecting retinas. Selected time-points correspond to times when miRNA levels are at their minimum (*a*; dark adaptation for 90 min) and maximum (*b*; light adaptation for 30 min) in DA and LA retinas, respectively (see Figures 3 and S4). **(C-E)** Effect of injection of α -Am (*left panels*), ActD (*middle panels*), or buffer alone (*right panels*) on the level of indicated miRNAs. Control determinations, for non-injected left eye, are always in left sub-panels. Levels of RNAs in retina from mice kept in continuous light, adapted to dark for 90 min, or mice moved from dark to light for 30 min, are shown as white, black, and grey squares, respectively. Values, normalized either to U6 RNA (for α -Am and buffer injections) or 18S rRNA (for ActD injections) are means \pm SEM ($n = 3$). Values for retinas from a control eye of mice kept in continuous light (time-point *a*) were set to one. **(F)** Control experiment demonstrating that injection of α -Am (*left panel*) or ActD (*middle panel*), but not buffer alone (*right panel*), strongly reduces the level of rod transducin (*Gat1*) mRNA, which is known to be expressed in mouse retina independently of the light/dark adaptation and shows fast turnover *in vivo* (106). **(G)** Control experiment demonstrating that injection of α -Am (*left panel*), ActD (*middle panel*), and buffer alone (*right panel*) has no marked effect on the level of U6 RNA. Levels of U6 RNA were normalized to the levels of RNA used for cDNA preparation.

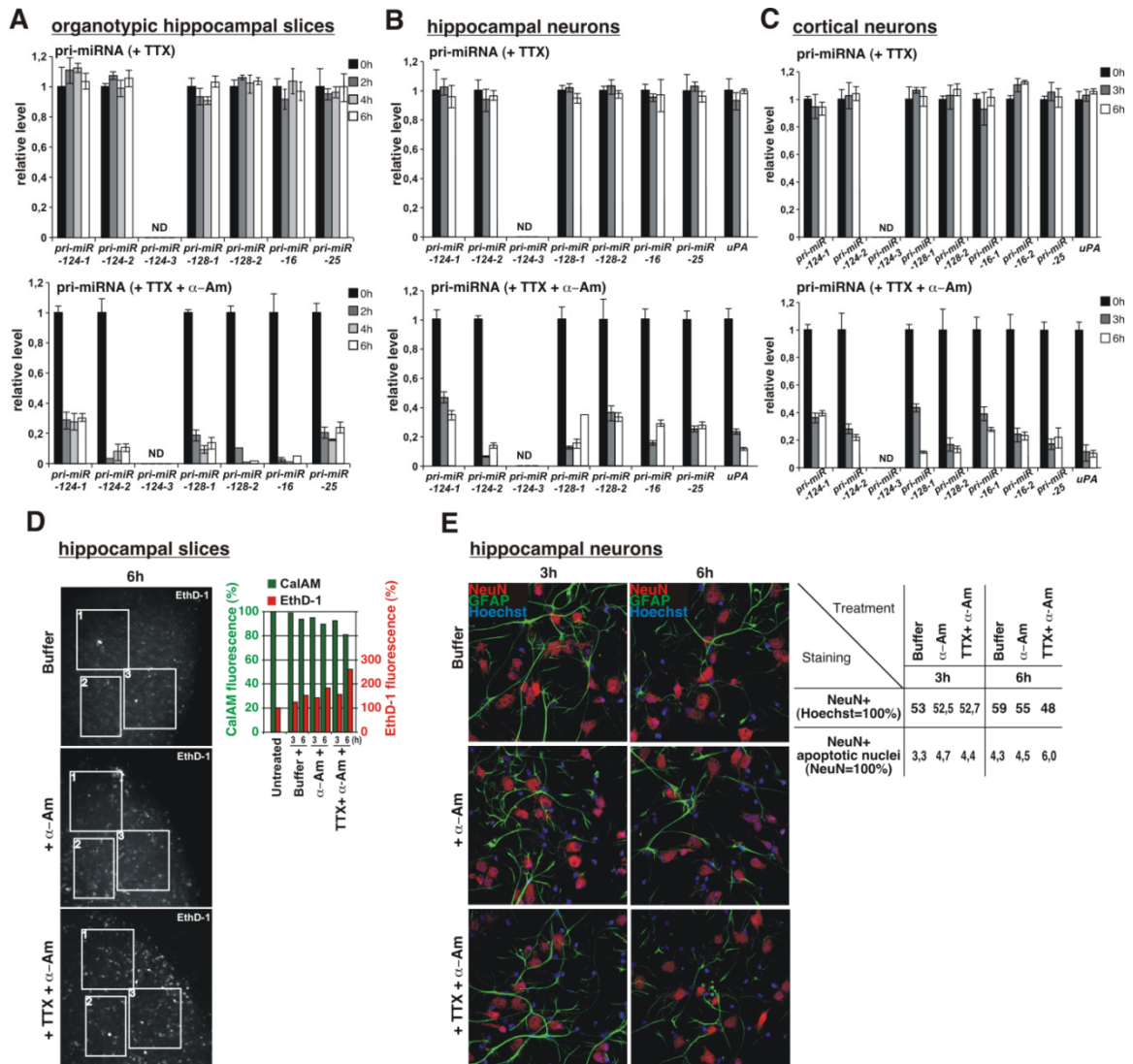


Figure S6, related to Figure 6. Control experiments assessing the effect of TTX on pri-miRNA and *uPA* mRNA turnover, and determining extend of cell death following treatment with either α -Am alone or α -Am + TTX. **(A-C)** Control experiments demonstrating that TTX treatment has no effect on expression levels of pri-miRNAs (*upper panels*) and does not influence the inhibitory effect of α -Am on pri-miRNA levels (*lower panels*) in organotypic hippocampal slices **(A)**, dissociated hippocampal neurons **(B)**, and dissociated neocortical neurons **(C)**. Levels of pri-miRNAs and *uPA* mRNA were determined using RNA from cultures treated with indicated inhibitors for 0, 3, or 6 h. Note that TTX is added to hippocampal slices and cultured neurons 1.5 and 0.5 h prior to the addition of α -Am, respectively. Values, normalized for U6 RNA, are means \pm SEM ($n=3$), with controls at 0h set to one. ND, not detectable. **(D and E)** Effect of α -Am or α -Am + TTX on cellular death in hippocampal slice cultures **(D)** and cultures of dissociated hippocampal neurons **(E)**. In **(D)**, cultures were stained with calcein AM (CalAM; staining living cells; green fluorescent signal) and ethidium homodimer-1 (EthD-1; staining dead cells; red fluorescent signal). Representative pictures of hippocampal slices, treated with inhibitors for 6h and showing EthD-1 staining, are presented. The graph shows average percentages of intensity of green and red

fluorescent signals measured, using 2-photon microscopy, for three regions per slice, with slices originating from two independent cultures. Values from untreated slices are set to 100%. Time of treatment with inhibitors is indicated. In (E), primary hippocampal cultures were stained with antibodies recognizing neuronal (NeuN) or astrocyte (GFAP) markers, and with Hoechst, following treatment with inhibitors. Shown are representative pictures of cultures treated with α -Am, α -Am + TTX, or buffer alone for 3 and 6h. Percentages of neurons (NeuN+) and dead neurons (NeuN+ containing apoptotic nuclei) represent means from 10 pictures obtained from two independent culture experiments. The total number of cells was determined by Hoechst staining.

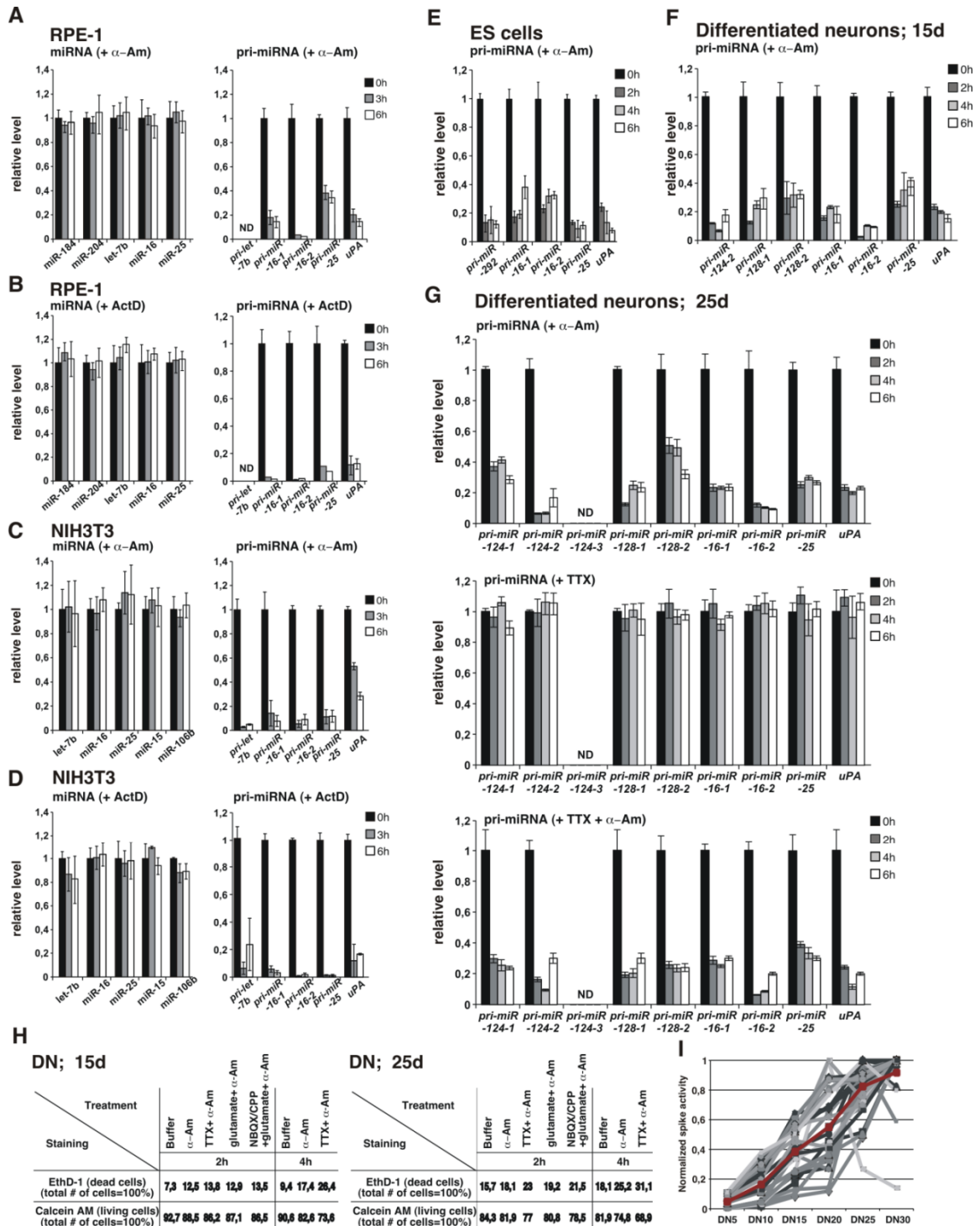


Figure S7, related to Figure 7. Control experiments assessing: (A-G) the effect of inhibitors on miRNA and pri-miRNA levels and turnover in RPE-1, NIH3T3, ES cells and ES-cell-derived neurons; (H) spiking activity of the ES-cell-derived neurons; and (I) the effect of inhibitors on cell death in ES-cell-derived neurons. (A-D) Analysis of mature miRNA (*left panels*) and pri-miRNA (*right panels*) levels in RPE-1 (A and B) or NIH3T3 (C and D) cells treated with either α -Am (A and C) or ActD (B and D) for 0, 3, or 6 h. Effectiveness of transcriptional inhibition was verified by analysis of urokinase (*uPA*) mRNA levels (*right panels*) (107). Values, normalized for U6 RNA (α -Am

treatment) or 18S rRNA (ActD treatment), are means \pm SEM (n=3). ND, not detectable. (E and F) Effect of α -Am on the level of pri-miRNAs in ES cells (E) and neurons maintained in culture for 15 days (F). Expression of pri-miR-16, pri-miR-124 and pri-miR-128 was analyzed for different genomic loci encoding the same mature miRNA. (G) Control experiments demonstrating that TTX treatment has no effect on expression levels of pri-miRNAs (*middle panel*) and does not influence the inhibitory effect of α -Am on pri-miRNA levels (*lower panel*) in ES-cell-derived neurons maintained in culture for 25 days. *Upper panel* (treatment with α -Am alone) represents an experiment similar to that shown in panels A and B. Levels of pri-miRNAs and *uPA* mRNA were determined using RNA from cultures treated with indicated inhibitors for 0, 2, 4, or 6 h. Note that TTX is added to cultured neurons 0.5 h prior to the addition of α -Am. Values, normalized for U6 RNA, are means (\pm SEM; n=3) with controls at 0 h set to one. (H) Effect of α -Am, α -Am + TTX, glutamate + α -Am, and NBQX/ CPP + glutamate + α -Am on cellular death in ES cells-derived neurons maintained in culture for 15 or 25 days, measured by staining with CalAM and EthD-1. Values represent average percentages of living and dead cells, based on 10 pictures obtained from three independent cultures. (I) Spontaneous spiking activity profile, recorded with MEAs, in the ES-cell-derived neurons at 5, 10, 15, 20, 25, and 30 days in culture. Normalized values of the array-wide spiking activity, measured for 30 different active electrodes (in two independent array experiments), are represented as grey lines. Red line represents a mean value. Only recordings from electrodes remaining active at day 30 are included in the graph. Spike range was 0-240 per min.

Supplemental tables

Table S1 and S2. Supplied as a separate Excel files (only as online supporting material)

Table S3. PCR primers used to amplify mouse, rat and human miRNA precursors and mRNAs.

Name	Forward primer (5'-3')	Reverse primer (5'-3')	Species
pri-miR-182	CCCTCCTAAAACCACCCTAA	AGTTGGCAAGTCTAGAACCAC	M
pre-miR-182	TTTGGCAATGGTAGAACTCAC	AGTTGGCAAGTCTAGAACCAC	M
pri-miR-183	TGTAGGACCTCCAGGAGAAGG	TATGGCCCTTCGGTAATTCA	M
pre-miR-183	GGCACTGGTAGAATTCCTGTG	TATGGCCCTTCGGTAATTCA	M
pri-miR-96	GTGCCAGGGTACAAAGACCT	GGCACTACACATGATTGCTCA	M
pre-miR-96	TTTGGCACTAGCACATTTTTG	GGCACTACACATGATTGCTCA	M
pri-miR-204	GCTAAGATGCCGGAGAATCA	GCCTTCCCAGCCTCCTTC	M
pre-miR-204	TTCCTTTTGTATCCTATGC	GCCTTCCCAGCCTCCTTC	M
pri-let7b	CTATGGCTCTAGTGGCCTGTG	GTATAGTTATCTTCGGAGGGGCA	M
pre-let7b	GAGGTAGTAGTTGTGTGGTTTCAG	GTATAGTTATCTTCGGAGGGGCA	M
pri-miR-29c	TCATTCAGTCCTGGTTGCAG	CCGATTTCAAATGGTGCTAGA	M
pre-miR-29c	TGACCGATTTCTCCTGGTGT	CCGATTTCAAATGGTGCTAGA	M
pri-miR-292	TTTACAGGAGCGGACAACCT	AACCGGTGACACTCAAACC	M
pri-miR-16-1	AAAAGGTGCAGGCCATACTG	TTGCCAACCTTACTTCAGCA	M
pri-miR-16-2	TGCTGAGTCCTGTCTTTTGG	ACGCCAATATTTACGTGCTG	M
pri-miR-25	AGGCTCCATTTGTTTGATGG	GCACTGTCAGACCGAGACAA	M
pri-miR-124-1	CCATCCCCTCCCTTTCTTT	ACCGCGTGCCTTAATTGTAT	M

pri-miR-124-2	GGAGTAGGGACTCCAAGCCTA	CTCCGCTCTTGGCATTAC	M
pri-miR-124-3	GGCGAAGAAGCTGGAGCA	ACCGCGTGCCTTAATTGTAT	M
pri-miR-128-1	TGACAGGTTTATAGGCCCTGA	GAAGTCAGGAAGCAGCTGAAA	M
pri-miR-128-2	TCCATGTTTTACTGCCACGA	CGGATTGACAGGGAATTCTG	M
pri-miR-124-1	CCCTCCCATCCTTCCTTCT	TTGTGCTGAGTCGATCCTTC	R
pri-miR-124-2	TACAAGCCTCGAACTGCAAG	GCACAGGATGGGTTCAATTCTA	R
pri-miR-124-3	CCCTCTGCGTGTTACAG	ATTGTTCCGCCGATTGTC	R
pri-miR-128-1	AGCCCTGGCTCTTTGATACA	TGAAGCCAAATGATGCAAAA	R
pri-miR-128-2	CAGCAGGATTGACAGGGAAT	ATGCAGCATACGTGATGGAA	R
pri-miR-16	CATCACACTTGATTATTATGTTTGA	TGGTTTTTATGTTAGAAAAGTGACAA	R
pri-miR-25	AGGGGTGAAACCAAGGATCT	ATGGGGAGCCTAGTGGAGTT	R
uPA	GGGTCAGTCGAAGGAGAGC	GTCTGAACCAAACGGAGCAT	M
β -actin	TGTTACCAACTGGGACGACA	GGAGAGCATAGCCCTCGTAG	M/R
β -tubulin	ACCGTAGCCATGAGGGAAAT	CCCAGTTCTAGATCCACCA	M/R
G α t1	GACGACGAAGTGAACCGAAT	GGTGACAGCGTCAAAGACAA	M
18S rRNA	CGGCTACCACATCCAAGGAA	GCTGGAATTACCGCGGCT	M/R/H
uPA	CGCTCAAGGCTTAACTCCAACAC	AACGGATCTTCAGCAAGGCAATG	H
pri-let7b	CTCCTGCTCTGGTGACTGAG	CCCTGCAGGTCAGTGGGT	H
pri-miR-16-1	AAAGGTGCAGGCCATATTGT	TGAAAAGACTATCAATAAACTGA AAA	H
pri-miR-16-2	GCGAATCATTATTTGCTGCTC	AAGAACAACAAAGGAAAAGGA	H
pri-miR-25	CAAGCTCCATCTGTCAT CT	GACACCCTTGTTCTGGCTTT	H

Supplemental table legends

Table S1, related to Figure 1. 454 sequencing (worksheet I) and Exiqon array (worksheet II) data of miRNAs expressed in DA and LA retinas. The Exiqon data represent results of two independent array experiments (I and II). Single arrays were used in Experiment I, while the data from Experiment II represent average hybridization signals from two independent array analyses performed for each DA and LA RNA samples originating from two independent experiments. Only miRNAs for which hybridization signal was significantly above the background are listed. For other details, see Supplementary Experimental Procedures. Note, that in Experiment I, in which a pool of RNA from ten different mouse organs (not including retinas) was used as a reference RNA, there is a dramatic difference between test and reference samples in the intensity at hybridization signals for miR-183/96/182 cluster and mir-211. This argues for the specificity of hybridization for these particular miRNAs.

Table S2, related to Figure 2. List of predicted miR-183/96/182 targets. (*Worksheet I*) List of genes expressed in mouse retina and predicted to be targets of the miR-183/96/182 cluster miRNAs by each of the three algorithms: PicTar, Targetscan 5.1 and MicroCosm (see also Figure 2A). Retinal expression of genes is based on data from (61, 108, 109) and our own array analysis. (*Worksheet II*) List of predicted targets of the miR-183/96/182 cluster miRNAs, which were found to be up-regulated ≥ 1.5 -fold ($p < 0.05$) in retinal photoreceptors of DA relative to LA retina. Up-regulation and p values for individual mRNAs are indicated.

Table S3. PCR primers used to amplify mouse, rat or human miRNA precursors, mRNAs, and U6 RNA.

My contribution

My contribution to the research article “Characterization of microRNAs induced by light adaptation in mouse retina reveals rapid turnover as a common property of neuronal microRNAs” published in Cell was following: I performed retinal tissue isolation for all experiments, except for the initial 454 sequencing screen (see Fig. 1). I evolved the idea to generate sponge sequences under consideration of thermodynamic parameters and helped to write an algorithm for sponge design and selection (together with Michael Stadler, unpublished). I selected all *in silico* generated sponge sequences used for this study. I generated adeno-associated-virus (AAV) sponge expression vectors for photoreceptor-specific expression for *in vivo* knockdown of particular microRNAs. I transfected mouse retinas with sponge AAVs *in vivo*, performed immunohistochemistry, confocal microscopy of transfected retinas and image processing. I also performed *in vivo* electroporations to deliver fluorescent reporter constructs to retinas of newborn mice that were used for ratiometric measurements to isolate microRNA targets *in vivo* (see Fig.2 and S3). I contributed to the design and accomplishment of the kinetic experiments, as well as in data presentation (see Fig. 3, 4, 5, S4, S5). Furthermore, I did all *in vivo* injection of transcription inhibitors (see Fig. 4). I dissociated retinas for fluorescent activated cell sorting (FACS) experiments (see Fig. 5). I performed extracellular spike recordings from embryonic stem cells derived neurons using a multi-electrode array system and corresponding analysis (see Fig. S7). I helped in writing of the manuscript.

Chapter 3: Side projects

3.1 - Genetically timed, activity-sensor and rainbow transsynaptic viral tools

Nat Methods. 2009 Feb;6(2):127-30. Epub 2009 Jan 4.

Genetically timed, activity-sensor and rainbow transsynaptic viral tools.

Boldogkoi Z, Balint K, Awatramani GB, Balya D, **Busskamp V**, Viney TJ, Lagali PS, Duebel J, Pásti E, Tombácz D, Tóth JS, Takács IF, Scherf BG, Roska B.

Abstract

We developed retrograde, transsynaptic pseudorabies viruses (PRVs) with genetically encoded activity sensors that optically report the activity of connected neurons among spatially intermingled neurons in the brain. Next we engineered PRVs to express two differentially colored fluorescent proteins in a time-shifted manner to define a time period early after infection to investigate neural activity. Finally we used multiple-colored PRVs to differentiate and dissect the complex architecture of brain regions.

PMID: 19122667

My contribution

I generated the DNA construct that was used to generate the transgenic mouse line expressing TN-L15 from the Thy1 promoter (see Methods.)

3.2 - KAP1-mediated epigenetic repression in the forebrain modulates behavioral vulnerability to stress

Neuron. 2008 Dec 10;60(5):818-31.

KAP1-mediated epigenetic repression in the forebrain modulates behavioral vulnerability to stress.

Jakobsson J, Cordero MI, Bisaz R, Groner AC, **Busskamp V**, Bensadoun JC, Cammas F, Losson R, Mansuy IM, Sandi C, Trono D.

Abstract

KAP1 is an essential cofactor of KRAB-zinc finger proteins, a family of vertebrate-specific epigenetic repressors of largely unknown functions encoded in the hundreds by the mouse and human genomes. Here, we report that KAP1 is expressed at high levels and necessary for KRAB-mediated repression in mature neurons of the mouse brain. Mice deleted for KAP1 in the adult forebrain exhibit heightened levels of anxiety-like and exploratory activity and stress-induced alterations in spatial learning and memory. In the hippocampus, a small number of genes are dysregulated, including some imprinted genes. Chromatin analyses of the promoters of two genes markedly upregulated in knockout mice reveal decreased histone 3 K9-trimethylation and increased histone 3 and histone 4 acetylation. We propose a model in which the tethering of KAP1-associated chromatin remodeling factors via KRAB-ZFPs epigenetically controls gene expression in the hippocampus, thereby conditioning responses to behavioral stress.

PMID: 19081377 [PubMed - indexed for MEDLINE]

My contribution

I used *in silico* approaches to identify target molecules (Krueppel-associated box (KRAB) zinc finger proteins (KRAB-ZFPs)) whose expression might be altered in the hippocampus due to the manipulation of epigenetic repression (knock out of corepressor KAP1). I verified *in silico* results by combining robotics with high throughput quantitative real time PCR (see methods).

3.3 – Light-activated channels targeted to ON bipolar cells restore visual function in retinal degeneration.

Nat Neurosci. 2008 Jun;11(6):667-75. Epub 2008 Apr 27.

Light-activated channels targeted to ON bipolar cells restore visual function in retinal degeneration.

Lagali PS, Balya D, Awatramani GB, Münch TA, Kim DS, **Buskamp V**, Cepko CL, Roska B.

Abstract

Genetically encoded optical neuromodulators create an opportunity for circuit-specific intervention in neurological diseases. One of the diseases most amenable to this approach is retinal degeneration, where the loss of photoreceptors leads to complete blindness. To restore photosensitivity, we genetically targeted a light-activated cation channel, channelrhodopsin-2, to second-order neurons, ON bipolar cells, of degenerated retinas *in vivo* in the Pde6b(rd1) (also known as rd1) mouse model. In the absence of 'classical' photoreceptors, we found that ON bipolar cells that were engineered to be photosensitive induced light-evoked spiking activity in ganglion cells. The rescue of light sensitivity was selective to the ON circuits that would naturally respond to increases in brightness. Despite degeneration of the outer retina, our intervention restored transient responses and center-surround organization of ganglion cells. The resulting signals were relayed to the visual cortex and were sufficient for the animals to successfully perform optomotor behavioral tasks.

PMID: 18432197

My contribution

I helped performing *in vivo* electroporations to deliver channelrhodopsin-2 to bipolar cells of *rd1* mice (see methods).

Summarizing Discussion

The reactivation of non-functional cone photoreceptors in mouse models of RP (Chapter 1) demonstrated that the intervention at the photoreceptor level had several advantages compared with inner retinal approaches. All complex cone pathways tested were restored in a sophisticated manner. This was important because it implied the restoration of vision as opposed to just reactivating light sensitivity. One single archaeobacterial light sensor substituted for the entire intrinsic phototransduction cascade. This was of utmost significance for the feasibility of gene therapy concerning practical issues and legal issues if this approach will be translated to patients. The light requirements to stimulate eNpHR were considered safe regarding photochemical or photothermal damage due to the red-shifted action spectra (lower energy of photons) of the light sensor. The therapeutic window for reactivated cones spanned about one third of a mouse lifetime (last point tested). This cannot be compared directly with the human disease but it is quite promising since the human RP progression is much slower. The ability of eNpHR to drive human photoreceptors *in vitro* demonstrates its translational potential. Apart from all biomedical aspects, my finding that morphologically altered cones in RP retinas are still connected to downstream bipolar cells has not been shown yet. At late stages of mouse RP, all cones were considered dead but my data suggested a preservation of ~25% at P260 in mice. This fraction of cones was enough to reactivate the retinas. The persisting cones also changed their protein expression pattern and merged with the inner nuclear layer. The use of s-RD mice indicated that the development of inner retinal pathways is genetically “hard-wired” and no light input is needed. My behavioral data showed differences between the two mouse models in the processing of light signals at higher visual centers suggesting visual-activity-dependent development of the brain circuitries. The reactivation of human photoreceptors in healthy but light-insensitive post-mortem retinas *in vitro* also enables the use of this system to study human retinal circuitries functionally, like color vision or foveal pathways.

The microRNA project (Chapter 2) addressed more basic questions of retinal functions. My contribution helped to understand how small non-coding RNA molecules regulate gene expression in retinal cells in a light level-dependent

manner. The finding that microRNA levels are regulated by their transcription but also by the turnover of mature microRNA in active neurons demonstrate their highly dynamic nature. MicroRNAs might act as master regulators or switches of gene expression. Current detection technologies are just starting to reach the resolution to study reliably the levels of these small molecules. Our findings shed light on the dynamics of the concentrations of a set of microRNAs in active neurons. Our results have to be taken under consideration by performing microRNA-mediated gene knock-downs in neurons for basic but also biomedical questions. The half-life of microRNAs in active neurons might be shorter than in other cell types tested so far.

Chapter 3.1 demonstrated the necessity of molecular biological and imaging tools to study retinal functions. The use of transgenic animals is advantageous concerning reliability and reproduction of experiments but expression levels are often lower and the generation of transgenic animals is very time consuming (~1 year).

The field of epigenetics deals with the non-genetic factors of gene expression such as DNA methylations and histone modification. The hippocampus-specific ablation of an epigenetically repressing modulator (KAP1) had an impact on animal behaviors such as anxiety, learning and memory (Chapter 3.2). Lacking the ability to form heterochromatin and thereby silence certain genes induced an impact on memory. Normally, the repressor complex is directed to specific DNA regions via DNA-binding zinc finger proteins, in a controlled manner. This indicates that active heterochromatin formation is linked to memory by repressing the expression of certain genes.

Chapter 3.3 was the first vision restoration project I contributed to. The combination of targeted gene expression and the knowledge of retinal circuitry led to the restoration of light perception in blind mice. The preservation of retinotopy - the spatial organization of neuronal responses - is essential to relay useful light information towards higher visual centers. In this project, the targeted expression of ChR2 to ON bipolar cells transformed these inner retinal cells to photoreceptors. This approach might be useful at late stages of RP when all functional photoreceptor-to-bipolar cell synapses are degenerated.

Material and Methods

Chapter 1: Material and Methods

Plasmids.

The sources and names of the plasmids that were used as starting materials are listed in Supplementary Table S2. Restriction enzymes were purchased from New England Biolabs. Polymerase chain reaction (PCR)-based cloning was performed using Herculase polymerase (Stratagene) followed by sequencing to verify that the constructs were free of mutations. The In-Fusion 2.0 PCR Cloning Kit (Clontech) was used to insert PCR products into linearized plasmids via homologous recombination. Primers for In-Fusion cloning were designed to comprise 21 bp homology to the PCR product and 15 bp homology to the target vector backbone. In some cloning steps, linearization was performed using two restriction enzymes to remove unwanted DNA segments.

First, to obtain pAAV2-hRHO-eNpHR-EYFP we linearized pAAV2.1-Rho-EGFP using NotI/HindIII, and inserted the PCR-amplified eNpHR-EYFP from Lenti-CaMKIIa-eNpHR-EYFP-WPRE (31). Forward primer: atcacactggcggccctagcggccacatgaggggta. Reverse primer: gattgatccaagcttcattacacctcgttctcgta. Note that Rho in pAAV2.1-Rho-EGFP and hRHO refer to the same promoter (hRHO, 0.9 kb).

Second, to obtain pAAV2-hRO-EGFP we linearized pAAV2.1-Rho-EGFP using NheI/NotI and inserted the PCR-amplified human red opsin promoter (hRO, 2.1 kb) from pRed2.1lacZ (37). Forward primer: tcgcccttaagctagcctacagcagccagggtgaga. Reverse primer: cggccttgctcacatggcggccgctatggaaagcc.

Third, to obtain pAAV2-hRO-eNpHR-EYFP we linearized pAAV2-hRO-EGFP using NotI/HindIII and inserted the PCR-amplified eNpHR-EYFP from Lenti-CaMKIIa-eNpHR-EYFP-WPRE. Forward primer: ctttccatagcggcctgccacatgaggggtacgcc. Reverse primer: attggatccaagctattacacctcgttctcgtagca.

Fourth, to generate the intermediate plasmid pCR-Blunt II-TOPO-mCAR, the mouse cone arrestin promoter fragment (38) (mCAR, 0.5 kb) upstream of the Arr3 gene was PCR-amplified from mouse genomic DNA. Forward primer: ggttcttccatttggcta. Reverse primer: cctccagctctggttgctaag. mCAR was then subcloned into the pCR-Blunt II-TOPO (Invitrogen) vector backbone. To obtain pAAV2-mCAR-EGFP, we linearized pAAV2.1-Rho-EGFP using NheI/EcoRV and inserted the PCR-amplified mCAR from pCR-Blunt II-TOPO-mCAR. Forward primer: tcgcccttaagctagggttcttccatttggctac. Reverse primer: gccagtgtgatggatcctccagctctggttgctaag.

Fifth, to obtain pAAV2-mCAR-eNpHR-EYFP we linearized pAAV2-mCAR-EGFP using NotI/HindIII and inserted the PCR-amplified eNpHR-EYFP from Lenti-CaMKIIa-eNpHR-EYFP-WPRE. Forward primer: atcacactggcggcctgccaccatgaggggtacgcc. Reverse primer: attggatccaagctattacacctcgttctcgtagca.

Sixth, to obtain pLV-mCAR-eNpHR-EYFP we linearized pRRLsincPPT-hPGK using EcoRV/BamHI and inserted the PCR-amplified mCAR-eNpHR-EYFP from pAAV2-mCAR-eNpHR-EYFP. Forward primer: ctcgagaagcttgatggttcttccatttggctac. Reverse primer: ctgtttaaacggatcctattacacctcgttctcgtgta.

Seventh, to obtain pbRHO-NpHR-EYFP (here bRho refers to the bovine rhodopsin promoter, 2.2 kb) the pRho-DsRed (18) was linearized using KpnI/NotI. The NotI site was blunted using T4 polymerase (New England Biolabs). NpHR-EYFP was cut out of pcDNA3.1/NpHR-EYFP (14) using KpnI/XbaI. The XbaI site was blunted using T4 polymerase. The two DNA fragments were ligated (2x Mighty Ligation Mix, Takara Bio) and called pbRHO-NpHR-EYFP. pbRHO-NpHR-EYFP was used for pronuclear injections to obtain transgenic mice in FVB background.

Eighth, to obtain pAAV2-hRHO-NpHR-EYFP we cut out NpHR-EYFP from pcDNA3.1/NpHR-EYFP (14) using NheI/BsrGI. The NheI site was blunted and NpHR-EYFP was ligated to EcoRV/BsrGI linearized pAAV2.1-Rho-EGFP (2x Mighty Ligation Mix, Takara Bio).

Animals.

Wild-type C57BL/6 mice were purchased from RCC Ltd. (Füllinsdorf, Switzerland). C3H/HeNCrl (*Pde6b^{rd1}*) mice were purchased from Charles River Laboratories (L'Arbresle Cedex, France). *Cnga3^{-/-}*; *Rho^{-/-}* double knockout mice were provided by Mathias Seeliger, Peter Humphries, and Martin Biel. The Fvb-Rho-NpHR-EYFP mouse line was generated in the transgenic mouse production facility at the Friedrich Miescher Institute. For this study, it was backcrossed to C57BL/6 mice. All animal experiments and procedures were approved by the Swiss Veterinary Office. The animals were maintained under a 12-hour light-dark cycle. The ranges of mice age used for particular experiments are listed in Supplementary Table S1. The ages of mice transfected with AAVs and used for retinal electrophysiology are shown in Fig. S6.

AAV production.

All recombinant adeno-associated viruses were made by Penn Vector Core and serotyped as listed in Supplementary Table S3. Penn Vector Core performed the genome copy (GC) number titration (see Supplementary Table S3) by using real-time PCR (TaqMan reagents, Applied Biosystems).

Lentivirus production.

Lentivirus was produced as previously described (52). The titer of LV-mCAR-eNpHR-EYFP was 2×10^9 VG/ml (viral genomes per ml).

Subretinal AAV administration.

The animals were anaesthetized using 3% isoflurane. A small incision was made with a sharp 30-gauge needle in the sclera near the lens. Through this hole, 2 μ l AAV were injected slowly (in 20-30 s) into the subretinal space using a blunt 5 μ l Hamilton syringe held in a micromanipulator. Mice older than P21 were used for injections. There was a minimum incubation time of 21 days before performing experiments on AAV-injected animals. For behavioral studies, we injected both eyes with either eNpHR- or EGFP-expressing AAVs.

Immunohistochemistry.

Retinas were isolated and fixed in 4% paraformaldehyde in phosphate-buffered saline (PBS) for maximal 30 min at room temperature (RT), and washed in PBS overnight at 4°C. Retinal whole mounts were incubated in 30% sucrose overnight at RT. The retinas were treated with three freeze-thaw cycles. After the freeze-thaw treatment, all the steps were performed at RT. Retinas were incubated in a blocking solution (10% normal donkey serum (NDS, Chemicon), 1% bovine serum albumin (BSA), and 0.5% Triton X-100 in PBS, pH 7.4) for 1h. Primary and secondary antibody applications were done in 3% NDS, 1% BSA, 0.02% sodium azide, and 0.5% Triton X-100 in PBS. All antibodies, dilutions and sources are listed in Supplementary Table S4. Primary antibodies were applied for 3-7 days. After washing the retina three times for 10 minutes in PBS, the retina was incubated with Alexa Fluor-conjugated secondary antibodies (1:200 dilution) and 10 µg/ml 4', 6-diamidino-2-phenylindole (DAPI, Roche Diagnostics), which stains cell nuclei, for 2h. After another three washes in PBS, the retina was mounted on a glass slide with ProLong Gold antifade reagent (Invitrogen). Retinal vibratome sections: Fixed retinas were embedded in 3% agarose (SeaKem Le Agarose, Lonza) in PBS, and 150µm vertical sections were cut using a Leica VT1000S vibratome. Antibody staining procedure was the same as in whole mounts. Note that we used primary anti green fluorescent protein (GFP) antibodies to label EYFP because of epitope homology. Neurobiotin-filled ganglion cells from patch clamping experiments were stained with Alexa Fluor 555-conjugated streptavidin (Invitrogen) as described before (110). We used choline acetyl transferase antibody to mark two IPL strata (110).

Confocal microscopy.

Confocal images of antibody-stained retinas were taken using a Zeiss LSM 510 Meta Axioplan 2 laser scanning confocal microscope (Carl Zeiss) equipped with argon and helium-neon lasers. Plan-Apochromat 63X/1.4 or 40X/1.4 oil immersion objective lenses were used. Image analysis and quantification were done using Imaris software (Bitplane).

Quantification of AAV transduction.

At least three retinal whole mounts per mouse line and AAV type were immunostained for GFP (to label eNpHR-EYFP- or EGFP-expressing cells) and cone arrestin (to label cones), as well as stained with DAPI (to label cell nuclei in order to count the total number of photoreceptors). In each wild-type retina the entire depth of the ONL was scanned by confocal microscopy at three randomly-chosen areas in AAV-transduced regions. Three horizontal sections of each ONL scan (top layer, central layer, and bottom layer close to OPL) were analyzed. Automatic cell count in Imaris (Bitplane) was used to determine the number of GFP-labeled, cone-arrestin-labeled, and DAPI positive photoreceptors. Due to the fact that eNpHR-EYFP is membrane-bound, the GFP channel in eNpHR-EYFP-transduced retinas was inverted. This inversion enabled automatic cell counting. After this automatic cell count procedure, which marked every counted cell, each confocal section was manually inspected to remove false automatic counts. In RD retinas the procedure was the same, but due to decreased ONL thickness only one horizontal section was analyzed per confocal scan. In total, 81 horizontal sections were analyzed from AAV-transduced wild-type retinas (n=7403 cells (hRHO), n=7974 (hRO), n=7996 (mCAR)), 26 for s-RD (n=1634 (hRHO), n=1865 (hRO), n=1871 (mCAR)), and 18 for f-RD (n=1183 (hRO), n=1105 (mCAR)). The cone-arrestin antibody failed to label cone cell bodies in the RD retinas in a reproducible manner. Therefore, subtype-specific quantifications were performed in wild-type animals. Cones are only present in the top row of the ONL. In total, 27 horizontal sections for cones (n=343 cells (hRHO), n=446 (hRO), n=463 (mCAR)) and 81 sections for rods (n=7060 cells (hRHO), n=7528 (hRO), n=7533 (mCAR)) were analyzed. Total photoreceptor cell number in a horizontal confocal optical section was obtained by counting DAPI-labeled nuclei. We determined total photoreceptor number in uninjected wild-type retinas from 24 sections (n=7169 cells) and in NpHR transgenic mouse line from 9 sections (n=2793 cells). Estimation of persisting cone cell bodies (Fig.

S7) based on the quantification on GFP-labeled cells in P99-108 (n=5 retinas), P184-255 (n=5 retinas) s-RD, P50-77 (n=3), and P182-264 (n=3) f-RD retinas. These numbers were related to the retinal area, divided by the maximal transfection efficiency (Mean + SEM) for each mouse model (s-RD 88.6%, f-RD 50.8%) and normalized to wild-type cone numbers (12,800 cells mm⁻², (111)).

Fluorescence-activated cell sorting (FACS).

Retinas from 4 mice per group (f-RD injected with mCAR-EGFP from P110 or P220 mice, and f-RD injected with mCAR-eNpHR-EYFP from P165 animals) were isolated and dissociated to single cells by papain digestion as previously described (112). EGFP- or eNpHR-EYFP-positive cells were sorted using FACS (MoFlo from DakoCytomation) and used for microarray profiling.

RNA isolation and amplification, and microarray profiling.

All samples were obtained in four biological replicates per genotype for microarray gene expression profiling. Following cell dissociation, cells were immediately sorted by FACS and immersed in 50 µl extraction buffer (Arcturus, USA), left to lyse at RT for 10 minutes and stored at -80°C. Total RNA from samples containing 500 or 300 cells was isolated using the PicoPure RNA isolation kit (Arcturus) with the following modifications. The tubes were incubated at 42°C for 10 minutes and vortexed at low speed. Total RNA was treated with 10 units of DNase I (Qiagen) for 15 minutes to remove any remaining genomic DNA and eluted in 8 µl elution buffer. The RNA quality was assessed using RNA 6000 PicoChips with the Agilent 2100 Bioanalyzer (Agilent). No traces of DNA were detected; degradation of the ribosomal RNA was absent. The rRNA represented 90–95% of total RNA and a ratio of 28S/18S equal to 1.9-2.2 was recorded, indicating that the extractions met the criteria for downstream genetic analysis. Total RNA from each sample was reverse-transcribed using 4 µM T7-(dT)24/T7-(dN)6 primer mix (Affymetrix) and 150 units Superscript II reverse transcriptase (Invitrogen) in a volume of 10 µl. Synthesis of second-strand cDNA was performed by adding 4 mM dNTPs, 6 units DNA Polymerase I, and 0.4 units RNase H in a 20 µl reaction volume. cRNA was produced by *in vitro* transcription (IVT) with a T7 RNA polymerase at 37°C for 14 hours using the MEGAscript T7 kit (Ambion) as per manufacturer's

instructions. For the second cycle, the first-strand cDNA was synthesized using 0.2 µg random primers from 9µl purified cRNA. The second-strand cDNA was produced using 10 µM T7-(dN)₆ primer and 40 units DNA polymerase at 16°C for two hours, after which 10 units of T4 DNA polymerase (Invitrogen) were added and incubation continued for another 10 minutes. The cDNA was *in vitro*-transcribed with a T7 RNA polymerase at 37°C for 16 hours. The single-strand cDNA was synthesized using 10 µg purified cRNA in the presence of 4 µg random primers, 0.2 M DTT, 12 mM dNTP + dUTP, and 750 units Superscript II (Roche Diagnostics) in a total volume of 20 µl. The cRNA was hydrolyzed with 2 units RNase H at 37°C for 40 minutes. The sense cDNA was purified and eluted in 28 µl elution buffer. Amplified products were purified using the GeneChip cDNA Sample Cleanup Module (Affymetrix) applying a 6,000 g centrifugation speed during the first two steps. To improve the recovery from the columns, water or elution buffer were spun into the matrix at 50 g and then left to stand for 4 minutes prior to 16,000 g centrifugation. The quantity and purity of the cRNA and cDNA produced during the first and second rounds were evaluated using the NanoDrop ND-1000 spectrophotometer (Nanodrop Technologies). The cDNA was then fragmented using UDG (uracil DNA glycosylase) and APE 1 (apurinic/aprimidic endonuclease 1), and biotin-labeled with TdT (terminal deoxynucleotidyl transferase) using the GeneChip WT Terminal labeling kit (Affymetrix). Hybridization was performed using 5 µg biotinylated target, which was incubated with the GeneChip Gene 1.0 ST array (Affymetrix) at 45°C for 16 hours. Following hybridization, nonspecifically bound nucleotides were removed by washing, and detection of specifically bound target was performed using the GeneChip Hybridization, Wash and Stain kit, and the GeneChip Fluidics Station 450 (Affymetrix). The arrays were scanned using the GeneChip Scanner 3000 7G (Affymetrix), and CEL files acquired using the GeneChip Command Console Software (Affymetrix). Quality control and gene expression value estimates were obtained after RMA and quantile normalization performed in R (version 2.10). To identify transcripts that are differentially expressed between the controls and the mutant mice, we defined a criterion of a 2-fold or greater difference, plus a P-value of < 0.01.

Human ocular tissue.

Human ocular tissue was obtained from the Cornea Bank of Amsterdam and was handled in accordance with the guidelines of the Declaration of Helsinki. Eyes were collected from five donors (ranging in age from 58 to 65 years) after death through natural causes. After removal of the cornea, eyes were put into storage within 6 to 12 hours in cold phosphate-buffered saline solution (PBS) and shipped to Basel where the experiments took place. Retinas were always put into culture less than 36 hours post-mortem.

Human retinal explant culture and vector administration.

Immediately after the arrival of the eyes, the anterior parts were removed and the vitreous humor with attached neural retina was transferred to a CO₂-independent medium (Invitrogen). The retina was separated from the vitreous humor and from the retinal pigment epithelium, and cut into ~1 cm² pieces. With the photoreceptor face up, these retinal pieces were placed on the polycarbonate membrane of a Transwell 0.4 μm cell culture insert (Corning) with one drop of CO₂-independent medium, and flattened with a polished Pasteur pipette. Next, the CO₂-independent medium was removed and 2 ml neurobasal-A medium with 2mM L-glutamine plus B27 supplement (NBA+; Invitrogen) were added to each well. 10-50 μl AAV (3×10¹² to 5×10¹² GC ml⁻¹, see Supplementary Table S3) or 10 μl lentivirus (2×10⁷ VG ml⁻¹) were added on top of the retinal explants. Virus-infected retinas were incubated for up to 18 days for AAVs, and 24-72 h for lentivirus. The culture medium was renewed by a daily addition of fresh NBA+ medium to each well. Human retinas were already light insensitive at the time of isolation.

Optical coherence tomography (OCT).

OCT and functional tests (see below) were performed at the Center for Clinical Investigation (CIC) of the Centre Hospitalier National d'Ophthalmologie des Quinze-Vingts in Paris. OCT imaging was carried out using spectral domain OCT (Spectralis® OCT, Heidelberg Engineering, Dossenheim, Germany).

Goldmann perimetry.

Photopic visual field measurements were performed with a Goldmann perimeter (Haag-Streit AG, Bern, Switzerland). The kinetic perimetry was performed by moving the tests IV1, V1, and V4 from non-seeing to seeing areas. The visual field areas were then determined after plotting the fields with a desktop planimeter.

Light stimulation of isolated retinas.

Light generated by a 120W epifluorescent mercury lamp-based illuminator (X-Cite 120PC, EXFO Photonics Solutions) was filtered with a band-pass filter (600-660 nm, Chroma Technology) and projected onto the retina. The light path was interrupted with a computer-controlled shutter (SC10, Thorlabs). Light intensity was modulated by neutral density filters over a range of 5 log units (ND 0-ND 40). For patterned light stimuli, the retina was stimulated using a digital light projector (V-332, PLUS Vision) filtered with the same band-pass filter used for the epifluorescent light path. A monochromatic light source (15nm bandwidth, TILL Photonics Polychrome V, Agilent Technologies) was used to provide a color-ramp, light flashes, or periodic light pulses at defined wavelengths. The color-ramp started at 400 nm and continuously increased to 650 nm within 5 s. Light intensities from all three light sources were measured using a fluorescent spectrometer (USB 4000, Ocean Optics) calibrated with a radiometric reference source (LS1-Cal, Ocean Optics). The stimulus was generated via custom-made software written by D.B. (Matlab, Mathworks and Labview, National Instruments).

Two-photon targeted patch clamp recordings.

AAV-transduced retinas from s-RD and f-RD mice were isolated in Ringer's medium (110mM NaCl, 2.5mM KCl, 1mM CaCl₂, 1.6mM MgCl₂, 10mM D-glucose, and 22mM NaHCO₃, bubbled with 5% CO₂/95% O₂). For photoreceptor patch clamp recordings, retinal slices (200 μm) were cut with a razor blade tissue chopper (Stoelting) and placed in the recording chamber of the microscope. The tissue was superfused in Ringer's medium at 36°C for the duration of the experiment. AAV-transduced fluorescent photoreceptors were

targeted with a patch electrode using a custom-made 2-photon microscope. A CCD camera was used to visualize the retina (illuminated with infrared light, 725-775 nm) during two-photon scanning. Whole-cell recordings were made using an Axon Multiclamp 700B amplifier. Patch electrodes were made from borosilicate glass (BF100-50-10, Sutter Instruments) pulled to 8-10 M Ω , and filled with 115mM K Gluconate, 10mM KCl, 1mM MgCl₂, 0.5mM CaCl₂, 1.5mM EGTA, 10mM HEPES, and 4mM ATP-Na₂ (pH 7.2). In f-RD retinas the photoreceptor recordings were only performed from cones, since rods died before our recordings. In s-RD retinas we used two criteria to identify cones before the recordings. First, since cone cell bodies occupy only the most distal row of the outer nuclear layer we recorded from cell bodies in this row. Second, since cone cell bodies are larger than rod cell bodies we only targeted the largest cell bodies. In a few cases we verified that we recorded from cones by filling the recorded cell with Lucifer yellow, which showed the characteristic axon terminals of cones. We cannot rule out completely the possibility that some of the recorded cells in s-RD retinas were rods.

For ganglion cell recordings, the retina was mounted ganglion-cell-side up on a piece of filter paper (MF-membrane, Millipore) with a 2 mm² opening in the middle. Ganglion cell spike recordings were performed with a loose cell-attached patch, using the same electrodes pulled to 6-8 M Ω , and filled with Ringer's medium. Excitatory currents were isolated by voltage clamping ganglion cells at the reversal potential of Cl⁻ (-60 mV) (110). For these recordings, electrodes were filled with 112.5mM CsMeSO₄, 1mM Mg SO₄, 7.8 $\times 10^{-3}$ mM CaCl₂, 0.5mM BAPTA, 10mM HEPES, 4mM ATP-Na₂, 0.5mM GTP-Na₃, 5mM lidocaine N-ethyl bromide (QX314-Br), and 7.5mM neurobiotin chloride (pH 7.2). To record spikes and currents, or to record spikes and obtain the morphology of ganglion cells, we first performed cell-attached recordings. Next, we broke into the recorded cell using another electrode filled with intracellular solution containing neurobiotin in whole-cell mode and either recorded currents of simply filled cells with neurobiotin for subsequent anatomical analysis. For human photoreceptor patch clamp recordings, we used human retinal explants, which were incubated with the lentiviral vectors for 1-2 days. The human retinas were cut into slices (200 μ m) with a razor blade

tissue chopper using the method as described above. Brightly labeled photoreceptors from the parafoveal region were targeted with a patch electrode (8-10 M Ω) filled with 115mM K gluconate, 10mM KCl, 1mM MgCl₂, 0.5mM CaCl₂, 1.5mM EGTA, 10mM HEPES, and 4mM ATP-Na₂ (pH 7.2). Patch-clamp recordings were also made from non-transduced human photoreceptors immediately after the isolation of the retina. The human tissue was superfused in Ringer's medium at 36°C for the duration of the patch-clamp experiment. All chemicals were obtained from Sigma, with the exception of ATP (Labforce) and neurobiotin (Vector Laboratories). Data were analyzed offline using Matlab (Mathworks). For statistics, we averaged over ON and OFF responses. The direction-selectivity index shown in Fig. 2E is computed as described (41).

Multi-electrode array recordings.

To record the spike trains of retinal ganglion cells, the isolated mouse retina was placed on a flat MEA60 200 Pt GND array with 30 μ m diameter microelectrodes spaced 200 μ m apart (Ayanda Biosystems or Multi Channel Systems). The retina was continuously superfused in oxygenated Ringer's solution (110mM NaCl, 2.5mM KCl, 1.0mM CaCl₂, 1.6mM MgCl₂, 22mM NaHCO₃, and 10mM D-glucose (pH 7.4 with 95% O₂/5% CO₂)) at 36°C during experiments. Recordings ranged from 1 to 5 h in duration. The signals were recorded (MEA1060-2-BC, Multi-Channel Systems) and filtered between 500 Hz (low cut-off) and 3,500 Hz (high cut-off). The spikes were extracted with a threshold of at least 4 times the standard deviation of the recorded trace (Matlab, Mathworks).

Visual-evoked potentials.

Mice (ages s-RD: P70-P99, f-RD: P67-118, wild-type: P42-60) were anesthetized by subcutaneous injection of 8% chloral hydrate. Atropine drops (1%) and Oculotect (Novartis) were applied to the right eyes to dilate and protect the pupils. After exposing the primary visual cortex (V1), platinum-iridium recording electrodes (size 0.0035, California Fine Wire Company) were inserted. Responses were first measured at different cortical depths, and the depth with the maximum response was chosen for further recordings. 500 ms light stimulus was delivered to the contralateral eye every 3 seconds, 30 times,

using an optical cable attached to a band pass filtered (D595/40, Chroma Technology) light source (EXFO XI120PC-XL, 120W, Photonic Solutions). The distance of the tip of the optical cable from the eye was 1 cm. The intensity of light was 10^{16} photons $\text{cm}^{-2} \text{s}^{-1}$ at the eye surface. Each neural response was band-pass filtered at 0.1-500 Hz.

Dark-light box.

Mice (ages s-RD: P44-P143, f-RD: P50-120, wild-type: P52-64, female) were kept under a 12-hour light-dark cycle and tested between 9 a.m. and 12 p.m. Movement of mice in the dark-light box was recorded with a wireless infrared camera (SA-6255, Stilus SA) equipped with a longpass-filter (FGL665, Thorlabs) and digitized at 25 frames s^{-1} (AV400MKII, TerraTec Electronic GmbH). The interior dimensions of the dark-light box were 32(width)×40(length)×22(height) cm. We inserted a non-transparent wall with a 7×3cm hole (the hole was at the bottom of the wall in the middle) in the middle of the box, creating two equal-sized compartments (32(width)×20(length)×22(height) cm). One compartment was illuminated from the top with two red LED arrays (OD-610-99-070, Opto Diode), while the other remained dark (<2 lux). Illumination in this “light compartment” could be adjusted between 2 and 2,000 lux. Mice were placed individually in the corner of the light compartment and allowed to freely explore the box. The movement of the animal was recorded for 5 minutes. The mouse’s head was used to define the compartment it occupied. The time spent in each compartment was recorded. f-RD animals (eNpHR- or EGFP-expressing) spent a variable amount of time in the light compartment before the first crossing. This increased the variance of the total time spent in the light or dark compartment. We eliminated this time in our analysis by calculating the time in light compartment as (total time in light compartment - time until the first crossing) / (total recording time - time until the first crossing). This modification introduced a slight preference for the dark compartment. Results were, however, still statistically significant without this correction.

Optomotor response.

The experiment was carried out as described previously (16, 51) with small modifications. Briefly, each mouse (ages s-RD: P113-P153, f-RD: P69-120, wild-type: P52-64, female, kept in a 12-hour light-dark cycle, tested between 9 a.m. and 3 p.m.) was placed on an elevated (20cm high) platform (9cm diameter) which was positioned in the middle of an optokinetic drum (30cm diameter, 40 cm height). The drum was made of transparent plastic and decorated with black vertical stripes of different widths corresponding to different cycles per degree (cpd) spatial frequencies (0.03, 0.07, 0.13, 0.26, 0.52 cpd) and rotated with a predetermined number (1, 2, 3, 4, 7) of revolutions per minute (rpm). The platform did not rotate. The drum was illuminated from outside with 6 red LED arrays (OD-610-99-070, Opto Diode) that generated 2,000 lux at the position of the animal's head. The contrast was 1:23 using the 0.26 cpd drum. During the test, the drum turned clockwise and then anti-clockwise for 2 min in each direction. This procedure was repeated at every spatial frequency at 2 rpm and every rotational speed at 0.13 cpd. Mice were recorded using the same video recorder and capture board as described above in the context of the dark-light box. We analyzed all head movements which lasted more than 400 ms. If the speed of the head (estimated as different angular positions within 400 ms) was within $\pm 15\%$ of the angular speed of the drum for more than 320 ms then the mouse was given a score of +1, if not it received -1. These points were added together to form a total score for the 2+2 min recording period. All RD analysis was done in an automated fashion by a program written in Matlab (Mathworks). Wild-type optomotor scores from female animals was obtained as previous described (51).

Statistical analysis.

If the Lilliefors test did not reject the hypothesis that the sample had a normal distribution at the 5% significance level and $n > 7$, then the statistical significance was determined using a one-tailed heteroscedastic Student's t-test. Otherwise the Wilcoxon rank-sum test was used. We used the Kruskal-Wallis non-parametric 1-way ANOVA test to compare groups. The different levels of

significance are indicated by * for $p < 0.05$, ** for $p < 0.01$, and *** for $p < 0.001$.
The error bars and \pm values represent s.e.m.

Chapter 2: Experimental procedures

Light/dark adaptation of mice and retina isolation

C57BL/6 mice were obtained from RCC (Fullinsdorf, Switzerland). Unless indicated otherwise, 6- to 8-week-old animals were used for the experiments. LA animals were kept in a room at 450 lux. For dark adaptation, animals were kept in a dark chamber with a maximum of 0.4 lux. Retinas from DA mice were isolated under dim red light.

Laser capture microdissection (LCM)

For extraction of RNA from LCM dissected layers, isolated retinas were cryoprotected in 20% sucrose for 15 min and embedded in Shandon M-1 (Thermo Fisher) embedding matrix to 20% sucrose ratio 1:2. Frozen tissues were cut into 18- μ m-thick sections and mounted on RNase-free MMI (Molecular Machines & Industries AG) membrane slides. For RNA isolation, retinal sections from 5 mice were stained with Mayer's haematoxylin for 5 sec, fixed, and dehydrated for 50 sec in 100% ethanol. After the sections were briefly air-dried, ~50,000 cells were captured from each retinal cell layer using MMI CellCut Plus® System microscopy. Total RNA was extracted from captured cell layers using Trizol reagent. For protein analysis by Western blotting, retinas were cryoprotected in 20% sucrose containing 10 μ g/ml DAPI and embedded as described above. Sections were fixed and dehydrated in ice-cold methanol for 50 sec. Once the sections were briefly air-dried, ~100,000 cells were captured from each retinal layer, lysed in 1x lysis buffer containing 50 mM Tris, pH 7.5, 10 mM EDTA, 1% SDS, and 1x protease inhibitor cocktail (Roche). For retinas infected with AAV2-Rho-EGFP/triple sponge or AAV2-Rho-EGFP/control viruses, ~50,000 cells from the EGFP-fluorescence-positive ONL+OS/IS layers were captured and lysed.

In vivo retina electroporation and two-photon ratiometric imaging

Subretinal injection and *in vivo* electroporation of plasmids into newborn (P0 or P1) mouse pups was as described (18). A two-photon microscope (custom in-house design by J.D. and B.R.) equipped with a 60x water immersion lens

(0.90W, LUMPlanFI/IR, Olympus, Japan) was used for ratiometric EGFP/RFP imaging.

Cell and organotypic tissue cultures

Organotypic hippocampal slices were prepared from Wistar rats at postnatal day 5 (84). 25-day-old cultures were used for all experiments. Primary hippocampal neurons were prepared from E18.5 Sprague-Dawley rats and cultured on plates coated with laminin (85). They were maintained in culture for 12 days in Neurobasal Medium (Invitrogen) supplemented with B27 (Invitrogen), 0.5 mM L-glutamine, and antibiotics. Mouse neocortical primary neurons were isolated from E16.5 C57Bl/6 mouse embryos and cultured for 28 days in serum-free medium, and supplements on dishes coated with poly-DL-ornithine.

ES cells, derived from blastocysts (3.5 PC) of mixed 129-C57Bl/6 background mice, were cultured on feeder and subsequently without feeder of MEF cells, using 3i medium. Differentiation was performed essentially as described previously (87) and cells were collected either 15 or 25 days after embryoid bodies dissociation.

Treatment with inhibitors

For testing the effect of inhibitors on RNA metabolism in retina, animals maintained under 12-h light/dark photoperiods were anesthetized and one of the eyes was injected both subretinally and intravitreally with 2 μ l of 200 μ M α -Am or ActD (106) in 1x PBS containing 1% DMSO. The inhibitors were injected 10 min before initiating light/dark adaptation experiments (see Figures 4A, B and S5A, B).

Organotypic hippocampal slices and cell cultures were treated with α -Am or ActD (both at 10 μ g/ml; Sigma) for indicated time. To block voltage-dependent Na⁺-channels, TTX (LATOXAN, France) was added to the medium at final concentration of 1 μ M either 1.5 h (organotypic slices) or 0.5 h (cell cultures) prior to blocking of transcription. To block ionotropic glutamate receptors, NBQX (10 μ M, Sigma) plus CPP (10 μ M, Sigma) were used. Glutamate was added to the medium at final concentration of 10 μ M (87), 15 min prior to blocking of transcription.

Chapter 2: Supplemental experimental procedures

Light/dark adaptation of mice and retina isolation

C57BL/6 mice were obtained from RCC (Fullinsdorf, Switzerland). Unless indicated otherwise, 6 to 8 week old animals were used for the experiments. Mice were bred in a pathogen-free environment with *ad libitum* access to food and drinking water. LA animals were kept in a room with the light phase (450 lux) from 6:00 am (ZT0) to 6:00 pm (ZT12). For dark adaptation, animals were kept in a dark chamber with maximum of 0.4 lux. Two light-dark adaptation regimes were used. In one regime, some animals were transferred to light at ZT0, while other group was maintained in dark till ZT3. Both groups were then sacrificed. In a second regime, all animals were moved to light at ZT0 and one half of the group was then moved to dark at ZT3 for 3 hours. All animals were sacrificed at ZT6. Since changes in the light-regulated miRNA levels did not significantly differ between the two regimes of light-dark adaptation, the data from both regimes were combined together. For kinetic experiments, details of the retinas collection are indicated in individual figures. Unless indicated otherwise, in different experiments, retinas originating from three to ten animals per group were pooled together and used for RNA extraction. Animals were sacrificed by cervical dislocation and retinas were immediately dissected from enucleated eyes in RNase free conditions. Retinas from DA mice were isolated under dim red light. Procedures described above and also other procedures with mice and rats, described further below, were conducted in accordance with the animal care and use guidelines of the Veterinary Department Basel-Stadt.

FACS isolation of retinal cells

To obtain retinal Müller glia cells tagged with Red Fluorescence Protein (RFP), hemizygous *PDGFRa-CRE* mice (113) were crossed with *floxed-RosaRFP* mice (114) to generate mice hemizygous for *PDGFRa/RosaRFP* allele. Retinal rod bipolar cells tagged with Enhanced Green Fluorescence Protein (EGFP) were isolated from FVB-Tg (*Pcp2-EGFP*)2Yuza/J mice (The Jackson Laboratory, Bar Harbor, USA) expressing EGFP under the direction of the mouse Purkinje cell protein 2 promoter (115). Retinal amacrine cells were FACS-sorted using

retinas from Tg(*Jer5*-EGFP)²⁶⁷Gsat mice (MMRRC, Mutant Mouse Regional Resource Center, USA), expressing EGFP under the immediate early response 5 promoter in subpopulation of amacrine cells (116). Adult LA animals were anesthetized and their eyes were injected intraocularly with a solution containing 200 μ M α -Am and 1% DMSO in 1x PBS (right eye; see below) or with a control buffer containing no α -Am (left eye). After 3 h, retinas from 5 mice were isolated and dissociated to single cells by digestion with papain as described (112). RFP- or EGFP-positive cells were enriched using FACS and used for RNA extraction with Trizol reagent.

In situ hybridization

Retinas from LA mice were dissected in PBS containing diethyl pyrocarbonate (DEPC), fixed in 4% paraformaldehyde (PFA) in PBS for 20 min, infiltrated with 30% sucrose, and embedded in Shandon M-1 embedding matrix. 20- μ m-thick sections were cut and picked up on Superfrost™ slides. After brief wash in PBS, retinal sections were treated with 10 μ g/ml Proteinase K (Roche) for 6 min, post-fixed in 4% PFA and acetylated with 0.25% acetic anhydride in 0.1 M triethanolamine. RNA in situ hybridization was performed as described (112, 117) with some modifications. Briefly, slides were prehybridized for 1 h at 50°C in a buffer containing 10 mM Tris pH 7.5, 600 mM NaCl, 1 mM EDTA, 50% formamide, 0.25% SDS, 10% dextran sulfate, 1x Denhardt's solution, 200 μ g/ml yeast tRNA, and 2 mM vanadium ribonucleotide complex. Slides were hybridized in the same buffer for 16 h at 55°C with 100 ng per slide of digoxigenin (DIG)-labeled miRCURY LNA probe (Exiqon) in a chamber humidified with 50% formamide and 5x SSC. We used predesigned miRCURY LNA probes for mmu-miR-182 (Exiqon 39474-00), mmu-miR-96 (39208-00), mmu-miR-183 (39071-00), mmu-miR-211 (39105-00), mmu-let-7b (39001-00). Mutant LNA probes, containing six bases with mismatches (underlined) to mature miRNA, were as follows: mut-miR-182 (GTGTCAACTACCTAAGCCATA), mut-miR-183 (CAGTGTTAAACTACCTCAGCCTAA), mut-miR-96 (AGCAATTTTAGTGCT TCAGCCAA), mut-miR-204 (CAGGCAATCGATGACTTTTCGGAA), mut-let7b (AACCGGACAACCTAAAGCCTCA). Slides were washed ones in 50% formamide/1x SSC, with 2x SSC, and with 0.2x SSC, each time for 30 min at

50°C. Sections were then shortly reequilibrated in 0.1 M maleic acid buffer (MABT; pH 7.5) containing 0.1% Tween 20, blocked for 1 h in 10% donkey serum (Chemicon, Millipore) in MABT, and incubated overnight at 4°C with anti-DIG alkaline phosphatase (AP)-conjugated Fab fragment (1:2000). Sections were rinsed in MABT and AP buffer (100 mM Tris, pH 9.5, 50 mM MgCl₂, 100 mM NaCl, 0.1% Tween 20) and signals were developed with nitroblue tetrazolium and 5-bromo-4-chloro-3-indolyl phosphate, supplemented with 2 mM levamisol hydrochloride (Fluka), in the dark for 2 h. Finally, retinal sections were dehydrated and mounted using UltraKit (Meditate Medizintechnik AG), examined, and photographed using an Axiophot microscope (Carl Zeiss MicroImaging) connected to a DFC480 camera (Leica).

Cell and organotypic tissue cultures

Organotypic hippocampal slices were prepared from Wistar rats at post-natal day 5 as described (84). Twenty-five days old cultures of hippocampal slices were used for all experiments. Primary hippocampal neurons were prepared from E18.5 Sprague-Dawley rats and cultured on plates coated with laminin as described (85). They were maintained in culture for 12 days in Neurobasal medium (Invitrogen) supplemented with B27 (Invitrogen), 0.5 mM L-glutamine, and antibiotics. Mouse neocortical primary neurons were isolated from E16.5 C57Bl/6 mouse embryos and cultured in serum-free medium and supplements on dishes coated with poly-DL-ornithine (0.5 mg/mL) as described (118-120). Twenty-eight days old cultures of neocortical neurons were used for all experiments.

ES cells, derived from blastocysts (3.5 PC) of mixed 129-C57BL/6 background mice, were cultured on feeder and subsequently without feeder of MEF cells, using 3i medium (121). Differentiation was performed essentially as described previously (122) and unless indicated otherwise, cells were collected either 15 or 25 days after embryoid bodies dissociation.

Mouse NIH3T3 cells were grown in Dulbecco's modified Minimum Essential Medium (DMEM; Invitrogen, Basel, Switzerland) supplemented with 2 mM L-glutamine and 10% heat-inactivated fetal calf serum (FCS) at 37°C in a humidified atmosphere containing 5% CO₂. The h-TERT-immortalized human

retinal pigmented epithelium (RPE-1) cell line (Clontech Laboratories, Inc., Palo Alto, CA) was maintained in DMEM:F-12 nutrient mixture (Gibco) supplemented with 2 mM L-glutamine, 10% FCS and 0.348% sodium bicarbonate at 37°C in a humidified atmosphere containing 5% CO₂.

454 sequencing

Total RNA from retinas of ten LA or DA seven-week-old mice was extracted with Trizol reagent (Invitrogen, Carlsbad, CA) according to the manufacturer's instructions. cDNA libraries for 454 sequencing were prepared by Vertis Biotechnologie AG (Freising, Germany). Briefly, 50 µg of RNA was combined with 25 fmol of 5'-end-³²P-labeled 15-nt and 30-nt RNA size markers, electrophoresed on a 15% polyacrylamide denaturing gel, and gel fragments containing 15 to 30-nt-long RNA were excised. RNA was eluted in 300 µL 0.3 M NaCl, the eluate passed through a 0.2 µm Nanosep 100 microcolumn and was ethanol-precipitated with 20 µg of glycogen as a carrier. RNA was 3'-polyadenylated, reverse-transcribed using oligo(dT) as a primer, and 454 adapter oligonucleotides were ligated to the cDNA 5'-end. Sequencing was performed by 454 Life Sciences Inc., Branford, CT. Sequences of RNA inserts were extracted from 454 reads (average length 91.2 nt) by removing exact matches to the 5' adapter 24-mer sequences (CTNNNGACCTTGGCTGTCACTCA, containing a 4 nt barcode) from the beginning of the read, and any matches to a sequence of four or more adenines that were at least 17 nt downstream of the removed 5' adapter. This procedure identified inserts in 99.5% of the reads, yielding sequences of an average length of 22.3 nt. These were then aligned to reference sequences for assignment to biological classes, in the following order: pre-miRNA (miRBase 10.1), rRNA (from GenBank R164), tRNA (from <http://lowelab.ucsc.edu/GtRNAdb>), snRNA and snoRNA (GenBank R164), piRNA (from (123)), repBase (release 13.02), mRNA (GenBank R164). Alignments were performed using oligomap (124), only considering perfect matches to reference sequences. Manual inspection of imperfect alignments indicated a high frequency of adenines in read sequences (close to their 3-termini) that were aligned to single nucleotide gaps in reference sequences. These "insertions" were likely caused by the strong adenine signal originating from the sequencing of the polyA tail in neighboring wells on the

sequencing plate. We therefore allowed for up to two non-templated adenines in read sequences to be removed if no perfect match of a read to any reference sequence was found. This increased the percentage of mapped reads from 47% to 95%. Of 36,056 and 39,331 sequences that were obtained from DA and LA libraries, 15,729 (44%) and 17,003 (43%) mapped to known miRNA sequences, respectively. miRNAs were quantified by counting reads aligned to pre-miRNA hairpins, assigning them to mature or mature-star forms depending on the alignment coordinates within the hairpin and mature miRNA sequence annotation from miRBase.

microRNA array profiling

MicroRNA array profiling was performed by Exiqon, using miRCURY LNA array versions 10.0 (experiment I) or 11.0 (experiment II) (Exiqon, Vedbaek, Denmark). Total RNA from retinas of LA or DA seven-week-old mice was extracted with Trizol reagent. The quality of the total RNA was verified by an Agilent 2100 Bioanalyzer profile. 1 µg (experiment I) or 400 ng (experiment II) of total test RNA and reference RNA was labeled with Hy3 and Hy5 fluorescent compound, respectively, using the miRCURY LNA Array power labeling kit (Exiqon), as described by the manufacturer. The reference RNA sample corresponded to either a pool of RNA from 10 different mouse organs (experiment I) or a pool of all test retinal RNA samples used in the experiment (experiment II). The Hy3-labeled test RNA and the Hy5-labeled reference RNA were mixed pairwise and hybridized to the miRCURY LNA arrays. The hybridization was done according to the miRCURY LNA array manual using a Tecan HS4800 hybridization station (Tecan, Austria). After hybridization, the microarray slides were scanned and stored in an ozone-free environment (ozone level below 2.0 ppb) to prevent potential bleaching of the fluorescent dyes. The miRCURY LNA array microarray slides were scanned using the Agilent G2565BA Microarray Scanner System (Agilent Technologies, Inc., USA), and the image analysis was carried out using the ImaGene 7.0 (experiment I) or 8.0 (experiment II) software (BioDiscovery, Inc., USA). The quantified signals were background corrected using the “Normexp with offset value 10” (125) followed by normalization using the global Lowess (locally weighted scatterplot smoothing) regression algorithm. In experiment I, pools of

retinas originating from LA or DA animals were analyzed on single arrays. In experiment II, two pools of retinas, for each LA and DA groups of animals (collected on different days) were analyzed; the data represent averages from these two biological replicates.

Quantification of mature miRNAs by RT-qPCR

Total RNA from mouse retina, dissected retina layers, or cell or tissue slice cultures was isolated with Trizol. For analysis of miRNA levels in mouse or rat material, we used the Applied Biosystem Taqman® microRNA Assay System (Applied Biosystems, Foster City, CA). RT reactions, in a final volume of 7.5 µl, contained: 1x RT buffer, 5 ng RNA, 50 nM miRNA-specific RT primer, 0.25 mM each dNTP, 0.25 U/µl RNase inhibitor, and 3.33 U/µl MultiScribe RT, and were incubated for 30 min at 16°C, 30 min at 42°C, 5 min at 85°C and then held at 4°C. For each RNA preparation, RT-qPCR reactions (including RT steps and no template control), were performed in triplicate. RT-qPCR was performed using an Applied Biosystems Prism 7000 Sequence Detection System. The 10 µl PCR reactions contained 0.67 µl RT product, 1x Taqman Universal PCR master mix, and 1 µl of primers and a probe mix of the Taqman® MicroRNA Assay. The reactions were incubated in a 96-well optical plate at 95°C for 5 min, followed by 40 cycles of 95°C for 15 s and 60°C for 60 s. The threshold cycle (Ct) values were determined using default threshold settings. The Ct is defined as the fractional cycle number at which the fluorescence passes the fixed threshold.

The Ct values determined for each sample were normalized to the average Ct obtained for U6 RNA, calculated from triplicate reactions. Estimation of miRNA copy numbers was performed as described previously (126). Briefly, standard curves were generated using HPLC- and polyacrylamide-gel-electrophoresis (PAGE)-purified oligoribonucleotides (Microsynth, Switzerland) corresponding to miR-182, miR-183, miR-96, miR-204, miR-211, let-7b, miR-29c, and miR-124a miRNAs. The Ct values obtained from different reactions were converted to absolute copy number of specific miRNAs per 10 pg of total RNA from retina tissue using appropriate standardization curves.

RT-qPCR quantification of miRNA precursors and mRNAs

Total RNA, treated with RNase-free DNase I, was reverse transcribed to using

random hexamers and Superscript III thermostable RT (Invitrogen). A 1 µg aliquot of RNA mixed with random primers was denatured at 65°C for 5 min and cooled to room temperature for 10 min to allow the hexamers to anneal. The remaining reagents (5 x Buffer, dNTPs, DTT, RNase inhibitor, Superscript III RT) were added as specified in Superscript III RT protocol and reactions were incubated for 60 min at 42°C. RT was inactivated by 5 min incubation at 85°C. Control reactions lacked Superscript III RT. All pri-miRNA- and pre-miRNA-specific primers were designed using criteria described previously (127). RT-qPCR was performed using standard protocol of Applied Biosystems Prism 7000 Sequence Detection System. Briefly, 1 µl of a 1/10 dilution of cDNA was added to 10 µl of the 2x SYBR green PCR master mix (Applied Biosystems) containing 0.5 µM primers. The reactions were amplified for 15 s at 95°C and 1 min at 60°C for 40 cycles. Each reaction was performed in triplicate and the data normalized to either U6 snRNA or 18S rRNA. Sequences of primers are provided in Table S3.

RNase Protection Assays

RNase Protection Assays (RPA) were performed using the mirVana miRNA probe construction and detection kits (Ambion), according to the manufacturer's instructions. Templates used for preparation of RPA probes complementary to miRNAs were: miR-182, TTTGGCAATGGTAGAACTCACCTGTCTC; miR-183, TATGGCACTGGTAGAATTCACCCTGTCTC; miR-96, TTTGGCACTAGCACATTTTTGCCTGTCTC; miR-204, TTCCCTTTGTCATCCTATGCCTCCTGTCTC; let-7b, TGAGGTAGTAGGTTGTGTGGTTCCTGTCTC. Briefly, RPA reactions contained 5 fmol (100,000 cpm) of internally-labeled (with [α -³²P]UTP) and PAGE-purified RPA probe and 3 µg of total retina RNA. Hybridization was carried out overnight at 42°C and RNase A/T1 digestion was at 37°C for 30 min. The protected fragments were analyzed by 12% PAGE under denaturing conditions and quantified with PhosphorImager (Typhoon, Molecular Dynamics).

Affymetrix microarray analysis

Gene expression in retina cell layers originating from either LA or DA animals

was assessed using Affymetrix GeneChip® Mouse Gene 1.0 ST Arrays representing over 28,800 genes, with 27 probes spread along each gene. Analysis was performed at Functional Genomics Facility of the Friedrich Miescher Institute for Biomedical Research. RNA (100 ng) from the LCM-dissected ~20,000 cells was processed according to Total RNA Labeling Protocol as per manufacturer's instructions. Array analysis (two arrays per experiment) was performed with RNA originating from two independent experiments. Fragmented cRNA was hybridized to GeneChip 1.0 ST arrays according to the manufacturer's instructions. Quality control and background normalization was performed using Refiner 4.1 from Genedata AG (Basel, Switzerland). Expression value estimates were obtained using the GC-RMA implementation in Refiner 4.1. Quantile-normalization and median scaling of the genes called present (detection p value <0.05) was performed in Genedata's Analyst 4.1 package. Data analysis was performed using Expressionist Analyst 4.1 from Genedata AG. Genes were required to pass a t -test (1-way ANOVA) with a $p < 0.05$. For photoreceptor cell layer, genes having a fold change of 1.5 or greater (relative to median) (Figure S2A and Table S4) between two conditions (DA versus LA retinas) were identified. Microarray data were deposited in the GEO database (GSE20396).

Reporter assays

Luciferase reporters. Renilla luciferase vector (pRL) was as described (128). To generate firefly luciferase vector (pFL) containing a CMV promoter, the CMV promoter region was excised from pRL as a *NheI*-*Bam*HI fragment and inserted into corresponding sites in the pGL4.10[*luc2*] (Promega). RL and FL cDNAs contain codons optimized for better expression in mammalian cells. A full-length 3'UTR of mouse *Slc1a1* mRNA (positions 1649-3708, NM_009199) was generated by RT-PCR using retinal cDNA as a template. The amplified fragment was cloned into *Xba*I site present downstream of the FL ORF in pFL. A mutant containing 3 bases non-complementary to the miRNA seed region in each miRNA binding site was created using a Quick-Change II XL Site-Directed Mutagenesis Kit (Stratagene), according to the manufacturer's protocol. miRNA mimics of miR-96, miR-182, miR-183 and a non-targeting control mimic were obtained from Dharmacon.

Mouse NIH3T3 cells were seeded onto 6-well plates one day before transfections. Cells (~60% confluent) were transfected with pFL-Slc1a1_wt or _mut (100 ng per well), pRL vector (100 ng per well), and miRNA mimics (5 nM). All transfections were carried out in triplicate with Nanofectin siRNA Kit, according to the manufacturer's instructions (PAA, Austria). Cell lysates were prepared with Passive Lysis Buffer (Promega) 48 h after transfection and luciferase activities were measured using the Dual Luciferase Reporter Assay (Promega).

EGFP reporters. The wt or mutant 3'UTR regions of *Slc1a1* mRNA were cloned in *XbaI* site downstream of the EGFP ORF in pd1EGFP-N1 reporter (Promega). The RFP coding region was excised from pDsRed2-N1 (Promega) as *EcoRI-NotI* fragment and inserted into corresponding sites in the pd1EGFP-N1 to replace EGFP and yielding control pDsRed plasmid. NIH3T3 cells were transfected with pEGFP-Slc1a1_wt or _mut reporters, pDsRed and miRNA mimics as described above. Cells were analyzed on a FACSCalibur Flow Cytometer (Becton Dickinson Immunocytometry Systems), using Cell Quest Pro acquisition software. Green and red fluorescence was measured using a 530 BP 30 nm and 630 BP 22 nm band pass filters, respectively. Gates were set to exclude necrotic cells and cellular debris, and the fluorescence intensity of events within the gated regions was quantified. Data were collected from 20,000 events for each sample.

Construction of sponge plasmids and viruses

Sponge sequences specific for mouse miR-182, miR-183 and miR-96 were designed to have eight miRNA binding sites for each individual miRNA, interrupted by 15-nt spacers. The triple sponge for all three miR-183/96/182 cluster miRNAs contained four binding sites for each miRNA. Binding sites for miRNAs were perfectly complementary to seed region, with a bulge at positions 9-12 to prevent cleavage of the sponge RNA (Figure S3C-F). Sequences of spacers and bulged nucleotides were optimized to have random nucleotide composition and to keep sponge regions unstructured (M.S. and V.B., unpublished data). Sponge regions, originally assembled in pJ241 plasmids (DNA 2.0, CA, USA), were cloned into *XbaI* site downstream of the EGFP ORF

in pd1EGFP-N1. Correctness of all reporter and sponge plasmids was verified by sequencing. NIH3T3 cells were cotransfected with sponge plasmids, pFL-Slc1a1_wt or _mut reporters, control pRL reporter, and miRNA mimics, as described above. A ratio of sponge plasmid to target reporter was 8:1. Luciferase assays were performed 48 h post-transfection.

To generate AAV constructs, the triple sponge sequence was excised from pJ241 vector using flanking *HindIII* sites and cloned into the EGFP 3'UTR region of AAV2-Rho-EGFP (36). AAV2-Rho-EGFP containing no sponge region served as a control (AAV2-Rho-EGFP/control). Recombinant AAVs (serotype 7) were produced by Penn Vector Core (Gene Therapy Program, PA). Penn Vector Core analyzed the genome copy (GC) number by real time PCR (TaqMan reagents, Applied Biosystems) as: 1.49E+13 GC/mL (AAV2-Rho-EGFP/triple) and 3.81E+12 GC/ml (AAV2-Rho-EGFP/control).

AAV administration and immunohistochemistry

For AAV administration, the eyes of anesthetized animals were punctured in the sclera close to the lens by a sharp 30 gauge needle. 2 μ L of AAV particle suspension were injected subretinally by a Hamilton syringe. After 3 weeks, some of the isolated retinas were fixed for 30 min in 4% PFA in PBS, followed by a washing step in PBS at 4°C. A Leica VT1000S vibratome was used to cut cross sections (150 μ m) of retinas embedded in 3% agarose in PBS. The sections were treated with 10% normal donkey serum (NDS), 1% BSA, 0.5% Triton X-100 in PBS for 1h at room temperature. Treatment with polyclonal rabbit anti-GFP Ab (Molecular Probes Inc.; 1:200) in 3% NDS, 1% BSA, 0.5% Triton X-100 in PBS was for days at room temperature. Treatment with secondary donkey anti-rabbit Alexa Fluor-488 Ab (Molecular Probes Inc.; 1:200) and DAPI, was for 2 h. Sections were washed, mounted with ProLong Gold antifade reagent (Molecular Probes Inc.) on glass slides, and photographed using a Zeiss LSM 510 Meta Axioplan 2 laser scanning confocal microscope (Carl Zeiss Inc.). Remaining retinas were used for the LCM dissection of photoreceptor layers (see above).

In vivo retinal electroporation and two-photon ratiometric imaging

Subretinal injection and *in vivo* electroporation of plasmids into newborn (P0 or

P1) mice was performed as described previously (18). Briefly, the pups were anesthetized and a small incision was made in the eyelid and sclera near the lens with a 30-gauge needle. DNA solutions (~5 µg/µl of each plasmid) in PBS containing 0.1% fast green dye were injected into the subretinal space through the incision by using a Hamilton syringe with a 32-gauge blunt-ended needle. For electroporation, tweezer-type electrodes (model 520, 7 mm diameter; BTX, San Diego, CA) were used and five square pulses of 50-ms duration with 950-ms intervals were applied by using a pulse generator. Plasmids pEGFP-Slc1a1_wt or _mut were coelectroporated with pDsRed into right eyes only.

A two-photon microscope (custom in-house design by J.D. and B.R.) equipped with a 60x water immersion lens (0.90W, LUMPlanFI/IR, Olympus, Japan) was used for ratiometric EGFP/RFP imaging. The excitation source was a mode-locked Ti:Sapphire laser (Mai Thai HP, Spectra Physics, CA) tuned to 930 nm. Two-channel recording allowed simultaneous measurement of EGFP/RFP-signals (EGFP filter: 515 BP 30; RFP filter: 605 BP 75). Images from fluorescent photoreceptor somata were acquired in whole mount retina. The data were analyzed with MATLAB (MathWorks, Inc.).

Western blotting

Retinas were lysed on ice in a buffer containing 50 mM Tris pH 7.5, 10 mM DTT, 10 mM EDTA, 1% SDS, and 1x complete protease inhibitor cocktail (Roche). Protein lysates (20 µg/lane) were separated by SDS-PAGE followed by electrotransfer to PVDF membrane (Millipore). Membranes were incubated for 2 h at room temperature with primary antibodies: anti-SLC1A1(a) (Invitrogen; 1:200), anti-SLC1A1(b) (Chemicon; 1:300), anti-SLC1A1(c) (Alpha Diagnostic Int.; 1:1,000), anti-Dicer (129) (1:500), anti-Drosha (Abcam, 1:200), anti-PAIP2 (recognizing both isoforms A and B; (130), 1:500), anti-ATP1B3 ((131), 1:500) or anti-β-tubulin mAb (Sigma; 1:10,000), and then with peroxidase-conjugated secondary antibodies. For ATP1B3 detection protein lysates were treated with *N*-glycosidase F (Roche) as described (131). Immunoreactive bands were visualized using Amersham ECL Western blotting detection reagents (GE Healthcare). For quantitative Westerns, IRDye® 680 or IRDye® 800CW secondary antibodies were used and membranes were

analyzed with the Odyssey Infrared Imaging System (LI-COR Biosciences). For Western analysis of proteins isolated from LCM microdissected cell layers, ~5 µg/lane of the protein lysate was separated by SDS-PAGE and Super Signal WestFemto Trial kit (ThermoScientific) was used for detection. Protein ladder PageRuler™ Plus (Fermentas) was used as a protein size marker. Anti-PAIP2 and anti-ATP1B3 antibodies were kindly supplied by N. Sonenberg (McGill University) and K. Sweadner (Harvard Medical School, Boston), respectively.

Immunofluorescence

ES cell-derived terminal neurons or hippocampal neurons were fixed in 4% paraformaldehyde/4% sucrose for 15 min and permeabilized with buffer containing 20 mM sodium phosphate pH 7.4, 450 mM NaCl, 0.3% Triton and 0.1% Gelatine. For Western analysis, anti-NeuN (Chemicon, 1:1000) and anti-GFAP (DAKO, 1:1000) primary mAbs were used together with secondary Alexa488/594 anti-mouse/rabbit antibodies.

Multi-electrode array (MEA) recordings

ES cell-derived terminal neurons were differentiated as described above and plated on 0.1% polyethyleneimine (PEI)/laminin coated MEAs (Multi Channel Systems MCS GmbH, Reutlingen, Germany). PEI coating was prepared according the manufacturer instructions (Multi Channel Systems). Spontaneous network activity was recorded using MEA dishes with a square array of 59 substrate-embedded titanium nitride microelectrodes (30 µm diameter, 200 µm inter-electrode distance), and an internal embedded reference electrode (200/30iR-Ti-gr). The MEA dishes were sealed with a semi-permeable membrane (ALA MEA-MEM, ALA Scientific Instruments Inc., Westbury, NY) to prevent contamination. The signals were repeatedly recorded using MEA amplifier (MEA-1060-2-BC, Multi Channel Systems) and filtered between 500 Hz (low cut-off) and 3500 Hz (high cut-off). At given time points, spikes were recorded for four minutes. Spikes were extracted with a threshold of at least 4 times the standard deviation of the recorded trace (Matlab, Mathworks).

Cell viability assays

For cell viability assays, a LIVE/DEAD Viability/Cytotoxicity Kit for mammalian

cells was used as per manufacturer's instructions (Molecular Probes, Invitrogen). For hippocampal slice cultures, calcein AM (CalAM; 0.5 μ M) and ethidium homodimer-1 (EthD-1; 1 μ M) were added to the medium following treatment with α -Am, TTX + α -Am, or buffer alone and incubation continued at 37°C for 20 min. CalAM stains living cells and emits green light at 515 nm, whereas EthD-1 stains dead cells and emits red light at 635 nm. Slices were imaged using a custom-built two-photon microscope controlled by ScanMag (132). Integrated green and red fluorescence signals were collected from three independent regions of each slice. Photomultiplier dark noise was measured before shutter opening and subtracted from the dataset. For ES-cell-derived neurons, cell viability test was performed using the same LIVE/DEAD Kit described above. Cells stained with CalAM and EthD-1 were imaged using Axiovert 200 fluorescence microscope. Numbers of live and dead cells were counted in 10 pictures taken from two independent cultures.

For assessment of apoptotic cell death in hippocampal primary neurons, chromatin state in nuclei was analyzed by staining cells with Hoechst 33342 dye (Invitrogen), following treatment with α -Am, TTX + α -Am, or buffer alone. Cells containing uniformly stained nuclei were scored as healthy viable cells, while cells containing condensed or fragmented nuclei were scored as apoptotic cells.

Chapter 3.1 - Methods

Transgenic mice

TN-L15, a gift of O. Griesbeck, was excised from TN-L15/pcDNA3.1 with BamHI (5') and EcoRI (3'). The 1860-bp fragment was subcloned into pBluescriptII KS(+) (Stratagene) using BamHI (5') and EcoRI (3') restriction sites and further subcloned into pULmEB (pcDNA3.1(+)) backbone from Invitrogen) using KpnI (5') and NotI (3') sites. An EcoRI fragment was isolated and was blunt-ended using T4 polymerase and inserted into the XhoI cut and blunt-ended pThy1-mEGFP vector² yielding pTTN. This plasmid was linearized with NotI and PvuI. The linear fragment was used for pronuclear injections to generate transgenic mice.

Chapter 3.2 - Methods

RNA Studies

Whole hippocampi were dissected and snap-frozen on dry ice. Tissue was homogenized by sonication. Total RNA was isolated using Trizol (Invitrogen) according to supplier's recommendations. For real-time PCR analysis RNA was treated twice with DNase (DNAfreeTurbo, Ambion). 0.5 mg of RNA was used for the reverse transcription performed with random primers (Invitrogen) and SuperscriptII (Invitrogen) according to supplier's recommendations. SYBR green quantitative real-time PCR was performed with Power SYBR Green PCR Master Mix (Applied Biosystems) using standard procedures. Data was quantified using the $\Delta\Delta C_t$ -method and were normalized to Gapdh and b-actin expression. All data shown is normalized to Gapdh. Actin-normalized data were very similar to Gapdh data. Primers were designed using PrimerExpress software (Applied Biosystems). The efficiency of all primer pairs were confirmed by performing reactions with serially diluted samples. The specificity of all primer pairs were confirmed by analyzing the dissociation curve. Primer sequences are found in Table S5. For analysis of the real-time PCR data one-way ANOVA followed by Tukey's post hoc test was used. The criterion for

significance for all analyses was $p < 0.05$. All data are expressed as mean \pm SEM.

Chapter 3.3 –Methods

Plasmid DNA Construction and *In vivo* Electroporation.

DNA constructs were generated using standard molecular biology protocols. A 200-base pair DNA sequence corresponding to nucleotide positions –8583 to –8384 relative to the ATG start codon of the mouse metabotropic glutamate receptor subtype 6 (GRM6) gene1 (nucleotide positions 16160939 to 16161138 of *Mus musculus* chromosome 11 genomic contig with Genbank accession no. NT_096135) was defined as a GRM6 enhancer element (D.S.K. and C.L.C., manuscript in preparation). This element was amplified from the genomic sequence upstream of the GRM6 coding region using the primers 5'–gactagtGATCTCCAGATGGCTAAAC–3' and 5'–ccgctcgagCAACCAGTCTTGTGGAGCC–3' to give the 200-base pair enhancer sequence, 5'–GATGATCTCCAGATGATGGCTAAACTTTTATTAATAATCATCATGAATGAA GTAGATATTATTACTACCAAATTATTGCTTTTCAGCATCCATTATTTAGT AGATAATAATAATCATCATGATGTTTTTTGCCTTTAATAATCTGTTATTAATG ATGTAGTAGTGAATTATTAAGAAATAATAACATCATTTCCTACTAAATAAT CATCATTACTACATCATCCCCCAAATCATCGTTAATAATCTGCTACTAAAGT ACTACATCATCTCTGGCTCAAACAAGACTGGTTG–3', flanked by *SpeI* and *XhoI* restriction enzyme recognition sequences. The isolated GRM6 enhancer element was fused to a SV40 eukaryotic promoter sequence from the pGL3-Promoter vector (Promega Corp.). The GRM6 enhancer-SV40 promoter fusion product was inserted into a modified2 pCAGGS vector (133) lacking the CAG promoter. The cDNA encoding a ChR2-EYFP fusion protein was excised from the pLECYT lentiviral vector (kind gift from K. Deisseroth) (134) and cloned downstream of the GRM6 enhancer-SV40 minimal promoter elements to produce the pGRM6-CY expression plasmid. Subretinal injection and *in vivo* electroporation of the pGRM6-CY plasmid into newborn (P0 or P1) mouse pups was performed as previously described (18). Plasmid DNA was transfected into right eyes only.

References

1. R. H. Masland, *Nat Neurosci* **4**, 877 (Sep, 2001).
2. B. Roska, A. Molnar, F. S. Werblin, *J Neurophysiol*, (Mar 1, 2006).
3. B. Roska, F. Werblin, *Nature* **410**, 583 (Mar 29, 2001).
4. D. Larhammar, K. Nordstrom, T. A. Larsson, *Philos Trans R Soc Lond B Biol Sci* **364**, 2867 (Oct 12, 2009).
5. F. A. Dunn, M. J. Lankheet, F. Rieke, *Nature* **449**, 603 (Oct 4, 2007).
6. F. A. Dunn, F. Rieke, *Neuron* **57**, 894 (Mar 27, 2008).
7. J. B. Demb, *J Physiol* **586**, 4377 (Sep 15, 2008).
8. H. Grosshans, W. Filipowicz, *Nature* **451**, 414 (Jan 24, 2008).
9. J. K. Phelan, D. Bok, *Mol Vis* **6**, 116 (Jul 8, 2000).
10. K. Shintani, D. L. Shechtman, A. S. Gurwood, *Optometry* **80**, 384 (Jul, 2009).
11. B. Lin, R. H. Masland, E. Strettoi, *Exp Eye Res* **88**, 589 (Mar, 2009).
12. E. Bamberg, J. Tittor, D. Oesterheld, *Proc Natl Acad Sci U S A* **90**, 639 (Jan 15, 1993).
13. G. Nagel *et al.*, *Biochem Soc Trans* **33**, 863 (Aug, 2005).
14. F. Zhang *et al.*, *Nature* **446**, 633 (Apr 5, 2007).
15. A. Bi *et al.*, *Neuron* **50**, 23 (Apr 6, 2006).
16. P. S. Lagali *et al.*, *Nat Neurosci* **11**, 667 (Jun, 2008).
17. Y. Zhang, E. Ivanova, A. Bi, Z. H. Pan, *J Neurosci* **29**, 9186 (Jul 22, 2009).
18. T. Matsuda, C. L. Cepko, *Proc Natl Acad Sci U S A* **101**, 16 (Jan 6, 2004).
19. T. Matsuda, C. L. Cepko, *Proc Natl Acad Sci U S A* **104**, 1027 (Jan 16, 2007).
20. S. Daya, K. I. Berns, *Clin Microbiol Rev* **21**, 583 (Oct, 2008).
21. T. R. Flotte, B. J. Carter, *Gene Ther* **2**, 357 (Aug, 1995).
22. Z. Boldogkoi *et al.*, *Nat Methods* **6**, 127 (Feb, 2009).
23. J. Jakobsson *et al.*, *Neuron* **60**, 818 (Dec 10, 2008).
24. T. Cronin, T. Leveillard, J. A. Sahel, *Curr Gene Ther* **7**, 121 (Apr, 2007).
25. R. E. Marc, B. W. Jones, C. B. Watt, E. Strettoi, *Prog Retin Eye Res* **22**, 607 (Sep, 2003).
26. Z. Y. Li, I. J. Kljavin, A. H. Milam, *J Neurosci* **15**, 5429 (Aug, 1995).
27. A. H. Milam, Z. Y. Li, R. N. Fariss, *Prog Retin Eye Res* **17**, 175 (Apr, 1998).
28. E. Banin *et al.*, *Neuron* **23**, 549 (Jul, 1999).
29. B. Schobert, J. K. Lanyi, *J Biol Chem* **257**, 10306 (Sep 10, 1982).
30. A. Seki *et al.*, *Biophys J* **92**, 2559 (Apr 1, 2007).
31. V. Gradinaru, K. R. Thompson, K. Deisseroth, *Brain Cell Biol* **36**, 129 (Aug, 2008).
32. G. P. Gao *et al.*, *Proc Natl Acad Sci U S A* **99**, 11854 (Sep 3, 2002).
33. C. Leberherz, A. Maguire, W. Tang, J. Bennett, J. M. Wilson, *J Gene Med* **10**, 375 (Apr, 2008).
34. E. Claes *et al.*, *Invest Ophthalmol Vis Sci* **45**, 2039 (Jun, 2004).
35. D. B. Farber, J. G. Flannery, C. Bowes-Rickman, *Prog Retin Eye Res* **13**, 31 (1994).
36. M. Allocca *et al.*, *J Virol* **81**, 11372 (Oct, 2007).
37. Y. Wang *et al.*, *Neuron* **9**, 429 (Sep, 1992).

38. X. Zhu *et al.*, *FEBS Lett* **524**, 116 (Jul 31, 2002).
39. C. Punzo, K. Kornacker, C. L. Cepko, *Nat Neurosci* **12**, 44 (Jan, 2009).
40. S. S. Nikonov, R. Kholodenko, J. Lem, E. N. Pugh, Jr., *J Gen Physiol* **127**, 359 (Apr, 2006).
41. W. R. Taylor, D. I. Vaney, *J Neurosci* **22**, 7712 (Sep 1, 2002).
42. P. Degenaar *et al.*, *J Neural Eng* **6**, 035007 (Jun, 2009).
43. S. W. Kuffler, *J Neurophysiol* **16**, 37 (Jan, 1953).
44. T. Gollisch, M. Meister, *Neuron* **65**, 150 (Jan 28).
45. E. V. Famiglietti, Jr., H. Kolb, *Science* **194**, 193 (Oct 8, 1976).
46. H. B. Barlow, *J Physiol* **119**, 69 (Jan, 1953).
47. J. B. Demb, *Neuron* **55**, 179 (Jul 19, 2007).
48. K. Yoshida *et al.*, *Neuron* **30**, 771 (Jun, 2001).
49. H. B. Barlow, R. M. Hill, *Science* **139**, 412 (Feb 1, 1963).
50. M. Bourin, M. Hascoet, *Eur J Pharmacol* **463**, 55 (Feb 28, 2003).
51. J. Abdeljalil *et al.*, *Vision Res* **45**, 1439 (May, 2005).
52. R. Zufferey, D. Nagy, R. J. Mandel, L. Naldini, D. Trono, *Nat Biotechnol* **15**, 871 (Sep, 1997).
53. B. Chen, C. L. Cepko, *Science* **323**, 256 (Jan 9, 2009).
54. T. Leveillard, J. A. Sahel, *Sci Transl Med* **2**, 26ps16 (Apr 7).
55. Y. Yang *et al.*, *Mol Ther* **17**, 787 (May, 2009).
56. B. Povazay *et al.*, *Opt Express* **17**, 4134 (Mar 2, 2009).
57. S. G. Jacobson *et al.*, *Invest Ophthalmol Vis Sci* **51**, 1079 (Feb).
58. N. Grossman *et al.*, *J Neural Eng* **7**, 16004 (Feb).
59. B. Y. Chow *et al.*, *Nature* **463**, 98 (Jan 7).
60. U. B. Kaupp, R. Seifert, *Physiol Rev* **82**, 769 (Jul, 2002).
61. J. C. Corbo, C. A. Myers, K. A. Lawrence, A. P. Jadhav, C. L. Cepko, *Proc Natl Acad Sci U S A* **104**, 12069 (Jul 17, 2007).
62. H. Wässle, *Nat Rev Neurosci* **5**, 747 (Oct, 2004).
63. Y. Fu, K. W. Yau, *Pflugers Arch* **454**, 805 (Aug, 2007).
64. E. N. Pugh, Jr., S. Nikonov, T. D. Lamb, *Curr Opin Neurobiol* **9**, 410 (Aug, 1999).
65. W. Filipowicz, S. N. Bhattacharyya, N. Sonenberg, *Nat Rev Genet* **9**, 102 (Feb, 2008).
66. D. P. Bartel, *Cell* **136**, 215 (Jan 23, 2009).
67. N. Bushati, S. M. Cohen, *Annu Rev Cell Dev Biol* **23**, 175 (2007).
68. A. Arora, G. J. McKay, D. A. Simpson, *Invest Ophthalmol Vis Sci* **48**, 3962 (Sep, 2007).
69. M. Karali, I. Peluso, V. Marigo, S. Banfi, *Invest Ophthalmol Vis Sci* **48**, 509 (Feb, 2007).
70. C. J. Loscher *et al.*, *Genome Biol* **8**, R248 (2007).
71. S. Xu, P. D. Witmer, S. Lumayag, B. Kovacs, D. Valle, *J Biol Chem* **282**, 25053 (Aug 24, 2007).
72. K. S. Kosik, *Nat Rev Neurosci* **7**, 911 (Dec, 2006).
73. G. Schrott, *Nat Rev Neurosci* **10**, 842 (Dec, 2009).
74. X. C. Ding, J. Weiler, H. Grosshans, *Trends Biotechnol* **27**, 27 (Jan, 2009).
75. S. N. Bhattacharyya, R. Habermacher, U. Martine, E. I. Closs, W. Filipowicz, *Cell* **125**, 1111 (Jun 16, 2006).
76. D. Gatfield *et al.*, *Genes Dev* **23**, 1313 (Jun 1, 2009).

77. H. W. Hwang, E. A. Wentzel, J. T. Mendell, *Science* **315**, 97 (Jan 5, 2007).
78. D. G. Ryan, M. Oliveira-Fernandes, R. M. Lavker, *Mol Vis* **12**, 1175 (2006).
79. C. W. Morgans *et al.*, *Proc Natl Acad Sci U S A* **106**, 19174 (Nov 10, 2009).
80. Y. Shen *et al.*, *J Neurosci* **29**, 6088 (May 13, 2009).
81. A. Nieoullon *et al.*, *J Neurochem* **98**, 1007 (Aug, 2006).
82. A. V. Tzingounis, J. I. Wadiche, *Nat Rev Neurosci* **8**, 935 (Dec, 2007).
83. M. S. Ebert, J. R. Neilson, P. A. Sharp, *Nat Methods* **4**, 721 (Sep, 2007).
84. L. Stoppini, P. A. Buchs, D. Muller, *J Neurosci Methods* **37**, 173 (Apr, 1991).
85. G. M. Schratt, E. A. Nigh, W. G. Chen, L. Hu, M. E. Greenberg, *J Neurosci* **24**, 7366 (Aug 18, 2004).
86. P. Landgraf *et al.*, *Cell* **129**, 1401 (Jun 29, 2007).
87. M. Bibel *et al.*, *Nat Neurosci* **7**, 1003 (Sep, 2004).
88. D. R. Copenhagen, C. E. Jahr, *Nature* **341**, 536 (Oct 12, 1989).
89. L. Gaal *et al.*, *J Neurophysiol* **79**, 190 (Jan, 1998).
90. J. Hasegawa, T. Obara, K. Tanaka, M. Tachibana, *Neuron* **50**, 63 (Apr 6, 2006).
91. P. Kugler, A. Beyer, *Histochem Cell Biol* **120**, 199 (Sep, 2003).
92. H. Y. Cheng *et al.*, *Neuron* **54**, 813 (Jun 7, 2007).
93. G. A. Wayman *et al.*, *Proc Natl Acad Sci U S A* **105**, 9093 (Jul 1, 2008).
94. S. Impey *et al.*, *Mol Cell Neurosci* **43**, 146 (Jan).
95. P. Rajasethupathy *et al.*, *Neuron* **63**, 803 (Sep 24, 2009).
96. P. Sethi, W. J. Lukiw, *Neurosci Lett* **459**, 100 (Aug 7, 2009).
97. S. W. Flavell, M. E. Greenberg, *Annu Rev Neurosci* **31**, 563 (2008).
98. S. Chatterjee, H. Grosshans, *Nature* **461**, 546 (Sep 24, 2009).
99. V. Ramachandran, X. Chen, *Science* **321**, 1490 (Sep 12, 2008).
100. T. Katoh *et al.*, *Genes Dev* **23**, 433 (Feb 15, 2009).
101. C. J. Barnstable, U. C. Drager, *Neuroscience* **11**, 847 (Apr, 1984).
102. D. S. Kim *et al.*, *J Comp Neurol* **507**, 1795 (Apr 10, 2008).
103. S. Rowan, C. L. Cepko, *Dev Biol* **271**, 388 (Jul 15, 2004).
104. C. L. Schlamp, E. C. Johnson, Y. Li, J. C. Morrison, R. W. Nickells, *Mol Vis* **7**, 192 (Aug 15, 2001).
105. J. I. Korenbrot, R. D. Fernald, *Nature* **337**, 454 (Feb 2, 1989).
106. R. Weiler, K. Schultz, M. Pottek, S. Tieding, U. Janssen-Bienhold, *Proc Natl Acad Sci U S A* **95**, 7139 (Jun 9, 1998).
107. S. Shetty, *Mol Cell Biochem* **271**, 13 (Mar, 2005).
108. S. Blackshaw *et al.*, *PLoS Biol* **2**, E247 (Sep, 2004).
109. H. L. Schulz, T. Goetz, J. Kaschkoetoe, B. H. Weber, *BMC Genomics* **5**, 50 (Jul 29, 2004).
110. T. A. Munch *et al.*, *Nat Neurosci*, (Sep 6, 2009).
111. C. J. Jeon, E. Strettoi, R. H. Masland, *J Neurosci* **18**, 8936 (Nov 1, 1998).
112. J. M. Trimarchi *et al.*, *J Comp Neurol* **502**, 1047 (Jun 20, 2007).
113. K. Roesch *et al.*, *J Comp Neurol* **509**, 225 (Jul 10, 2008).
114. H. Luche, O. Weber, T. Nageswara Rao, C. Blum, H. J. Fehling, *Eur J Immunol* **37**, 43 (Jan, 2007).
115. M. Tomomura, D. S. Rice, J. I. Morgan, M. Yuzaki, *Eur J Neurosci* **14**, 57 (Jul, 2001).

116. S. Siegert *et al.*, *Nat Neurosci* **12**, 1197 (Sep, 2009).
117. D. Damiani *et al.*, *J Neurosci* **28**, 4878 (May 7, 2008).
118. D. Lindholm, P. Carroll, G. Tzimagiogis, H. Thoenen, *Eur J Neurosci* **8**, 1452 (Jul, 1996).
119. A. Weiss *et al.*, *J Neurochem* **104**, 846 (Feb, 2008).
120. F. Zafra, B. Hengerer, J. Leibrock, H. Thoenen, D. Lindholm, *EMBO J* **9**, 3545 (Nov, 1990).
121. Q. L. Ying *et al.*, *Nature* **453**, 519 (May 22, 2008).
122. M. Bibel, J. Richter, E. Lacroix, Y. A. Barde, *Nat Protoc* **2**, 1034 (2007).
123. A. Aravin *et al.*, *Nature* **442**, 203 (Jul 13, 2006).
124. P. Berninger, D. Gaidatzis, E. van Nimwegen, M. Zavolan, *Methods* **44**, 13 (Jan, 2008).
125. M. E. Ritchie *et al.*, *Bioinformatics* **23**, 2700 (Oct 15, 2007).
126. M. Sarasin-Filipowicz, J. Krol, I. Markiewicz, M. H. Heim, W. Filipowicz, *Nat Med* **15**, 31 (Jan, 2009).
127. T. D. Schmittgen, J. Jiang, Q. Liu, L. Yang, *Nucleic Acids Res* **32**, e43 (2004).
128. R. S. Pillai *et al.*, *Science* **309**, 1573 (Sep 2, 2005).
129. E. Billy, V. Brondani, H. Zhang, U. Muller, W. Filipowicz, *Proc Natl Acad Sci U S A* **98**, 14428 (Dec 4, 2001).
130. J. J. Berlanga, A. Baass, N. Sonenberg, *RNA* **12**, 1556 (Aug, 2006).
131. E. Arystarkhova, K. J. Sweadner, *J Biol Chem* **272**, 22405 (Sep 5, 1997).
132. N. Holbro, A. Grunditz, T. G. Oertner, *Proc Natl Acad Sci U S A* **106**, 15055 (Sep 1, 2009).
133. H. Niwa, K. Yamamura, J. Miyazaki, *Gene* **108**, 193 (Dec 15, 1991).
134. E. S. Boyden, F. Zhang, E. Bamberg, G. Nagel, K. Deisseroth, *Nat Neurosci* **8**, 1263 (Sep, 2005).

Curriculum Vitae of Volker Buskamp

Personal Details

Name: Volker Buskamp
Date of Birth: 25th December 1980
Nationality: German
Address: Chesterplatz 6
D-79539 Lörrach
Tel: +49-176-21171450
Email: volker.buskamp@fmi.ch

Education

Since 10/2007 **Friedrich Miescher Institute for Biomedical Research (FMI) in Basel and “*Frontiers in Genetics*” Geneva, Switzerland**
PhD thesis in Botond Roska’s group

08/2007 **University of Geneva, Switzerland**
Post graduate diploma in biology (DEA), average grade: 5.7 (max. grade 6.0)

Since 10/2006 **“*Frontiers in Genetics*” Graduate School, National Center of Competence in Research (NCCR), Geneva, Switzerland**

09/2006 **Technical University of Braunschweig, Germany**
Diploma in biotechnologies, average grade: “Sehr gut” (1.1)

10/2005 – 09/2006 Friedrich Miescher Institute for Biomedical Research (FMI) in Basel, Switzerland

External diploma thesis in Neurobiology, Botond Roska's group entitled: "*Lighting up neurons in the mammalian retina to understand their morphology, connectivity and function*"

Grade: 1.0

10/2003 – 10/2005 Technical University of Braunschweig, Germany

Advanced study period in biotechnologies, *Viva voce* diploma examination in Genetics, Technical Chemistry, Process Engineering, Technical Biochemistry and Microbiology, average grade: 1.2

10/2001 – 09/2003 Technical University of Braunschweig, Germany

Intermediate diploma in biotechnologies, average grade: 1.6

08/1991 – 06/2000 Euregio-Gymnasium in Bocholt, Germany

Degree: German Abitur, average grade: 1.5

Work experience

05/2007 – 09/2007 Friedrich Miescher Institute for Biomedical Research (FMI) in Basel, Switzerland

Rotation within the scope of the NCCR graduate school in Botond Roska's lab, project title: "*Restoring photoreceptor function in blind mice*"

01/2007 – 04/2007 Friedrich Miescher Institute for Biomedical Research (FMI) in Basel, Switzerland

Rotation within the scope of the NCCR graduate school in Prof. Susan Gasser's lab, project title: "*Telomere position effect in yeast*"

10/2006 – 12/2006 **Ecole Polytechnique Fédérale de Lausanne (EPFL), School of Life Sciences, Laboratory of Virology and Genetics (LVG), Lausanne, Switzerland**

Rotation within the scope of the NCCR graduate school in Prof. Didier Trono's lab, project title: "*KAP1 knock out effects*"

02/2005 – 04/2005 **Institute of Developmental Genetics in Braunschweig, Germany**

Student research project in Prof. Ralf Schnabel's lab, thesis: "*Establishment of an ADH depending selection system for C. elegans*"

07/2003 – 06/2004 **Institute of Developmental Genetics in Braunschweig, Germany**

Student assistant, tasks: DNA extraction, PCR, DNA sequencing, 4D microscopy

Publications

Busskamp V, Duebel J, Balya D, Fradot M, Viney TJ, Siegert S, Groner AC, Cabuy E, Forster V, Seeliger M, Biel M, Humphries P, Paques M, Mohand-Said S, Trono D, Deisseroth K, Sahel JA, Picaud S, Roska B. "Genetic Reactivation of Cone Photoreceptors Restores Visual Responses in Retinitis pigmentosa", *Science* 23 July 2010: Vol. 329. no. 5990, pp. 413 - 417

Krol J, **Busskamp V**, Markiewicz I, Stadler MB, Ribi S, Richter J, Duebel J, Bicker S, Fehling HJ, Schübeler D, Oertner TG, Schrott G, Bibel M, Roska B, Filipowicz W. "Characterizing light-regulated retinal microRNAs reveals rapid turnover as a common property of neuronal microRNAs", *Cell*. 2010 May 14;141(4):618-31.

Boldogkoi Z, Balint K, Awatramani GB, Balya D, **Busskamp V**, Viney TJ, Lagali PS, Duebel J, Pásti E, Tombácz D, Tóth JS, Takács IF, Scherf BG, Roska B. "Genetically timed, activity-sensor and rainbow transsynaptic viral tools", *Nat Methods*. 2009 Feb;6(2):127-30.

Jakobsson J, Coredero MI, Bisaz R, Groner AC, **Busskamp V**, Bensadoun JC, Cammas F, Losson R, Mansuy IM, Sandi C, Trono D, “KAP1-mediated Epigenetic Repression in the Forebrain Modulates Behavioral Vulnerability to Stress”, Neuron 2008 Dec 10;60(5):818-31

Lagali PS, Balya D, Awatramani GB, Münch TA, Kim DS, **Busskamp V**, Cepko CL, Roska B. “Light-activated channels targeted to ON bipolar cells restore visual function in retinal degeneration”, Nat Neurosci. 2008 Jun;11(6):667-75.

Fellowships

- 06/2006** Accepted for the “Frontiers in Genetics” graduate school
- 01/2006** Accepted for the Friedrich Miescher Institute for Biomedical Research (**FMI**) international PhD program

Skills Profile

- IT** Competent in Microsoft Windows, Linux and Unix system software
- Extensive knowledge in Microsoft Office
- Image processing (Adobe Photoshop, Adobe Illustrator, Bitplane Imaris™)

- Languages**
- English:** fluent in writing and speaking
- German:** native speaker
- French:** basic level
- Latin:** “groses Latinum”

Interests & Activities

Enjoy travelling and meeting people from different cultures

Sports: running, swimming, cycling and football

Fond of reading literature books

Music and cinema

Additional Information

Military obligations fulfilled (07/00 – 04/01)

References

Available on request